Trabajo Fin de Máster
Máster en Ingeniería Aeronáutica

E-sail attitude control with tether voltage modulation in non-symmetric operation

Autor: Antonio del Valle Hernández

Tutores: Guillermo Pacheco Ramos, Rafael Vázquez Valenzuela

Dpto. de Ing. Aeroespacial y Mecánica de Fluidos
Escuela Técnica Superior de Ingeniería
Universidad de Sevilla

Sevilla, 2023

Trabajo Fin de Máster
Máster en Ingeniería Aeronáutica

E-sail attitude control with tether voltage modulation in non-symmetric operation

Autor:
Antonio del Valle Hernández

Tutores:
Guillermo Pacheco Ramos, Rafael Vázquez Valenzuela
Profesor Sustituto Interino, Profesor Titular

Dpto. de Ing. Aeroespacial y Mecánica de Fluidos
Escuela Técnica Superior de Ingeniería
Universidad de Sevilla

Sevilla, 2023

Trabajo Fin de Máster: E-sail attitude control with tether voltage modulation in non-symmetric operation

Autor: Antonio del Valle Hernández
Tutores: Guillermo Pacheco Ramos, Rafael Vázquez Valenzuela

El tribunal nombrado para juzgar el trabajo arriba indicado, compuesto por los siguientes profesores:

Presidente:

Vocal/es:

Secretario:

acuerdan otorgarle la calificación de:

El Secretario del Tribunal

Fecha:

Agradecimientos

Estos seis años de carrera universitaria han sido sin duda una etapa enriquecedora y memorable de mi vida, con sus altibajos combinando alegría y éxito con momentos más sufridos, pero siempre superado con el apoyo y el cariño de todas las personas que han estado ahí durante este tiempo. Por eso, me gustaría agradecer a todas esas personas (compañeros y compañeras de clase, el excelente profesorado y mi entorno más cercano) por aportarme cada una un granito de arena en la persona que soy hoy.

En concreto, agradecer a mis tutores Guillermo y Rafael que me hayan dado la oportunidad de trabajar y aprender un poco más sobre nuevas tecnologías de propulsión espacial y sobre el control de actitud, compartiéndome su pasión por el espacio, que tan importante es para un Ingeniero Aeronáutico. Gracias por vuestro apoyo y consejo durante estos meses.

Finalmente, mi agradecimiento más sentido se debe a mi familia y amigos de confianza, por "aguantarme" estos meses compaginando trabajo y estudios, y siempre darme esos momentos de desconexión y felicidad que uno necesita para motivarse en proyectos con tanta dedicación. Gracias especialmente a mi esposa, Isa, con la que he tenido la inmensa suerte de crecer como persona y compartir todos los logros y experiencias, con su inestimable apoyo incondicional.

Antonio del Valle Hernández
Sevilla, 2023

Resumen

Título

Control de actitud de E-sails mediante la modulación del voltaje de los cables en operación asimétrica.

Resumen del trabajo

La Vela Solar Eléctrica (*E-sail*) es una novedosa tecnología propulsiva sin propelente aplicable a vehículos espaciales, que genera el empuje necesario a partir de la interacción eléctrica entre cables (*tethers*) muy largos cargados eléctricamente y los iones del viento solar. Así pues, el presente trabajo aborda el problema de control de actitud de las *E-sails*, con el objectivo principal de ampliar el rango de validez de trabajos recientes ([1], [2]), que logran realizar maniobras de cabeceo manteniendo el eje de giro en una alineación próxima con el Sol, y considerando una deformación simétrica de los *tethers*. Para tal fin, en este proyecto se propone un modelo de deformación no simétrico, que permite a los *tethers* deformarse de forma independiente según la orientación relativa al Sol y el voltaje aplicado, tal y como sucedería en realidad. Esta propuesta es entonces analizada bajo control LQR para comprobar su rango de validez y estudiar la respuesta al control de la vela solar eléctrica, y, después, bajo control LQG para incluir la influencia de las perturbaciones y el ruido procedente de los sensores en el análisis.

Palabras clave

Vela Solar Eléctrica, E-sail, Control de Actitud, Regulador Cuadrático Lineal, Filtro de Kalman, Regulador Cuadrático Lineal Gaussiano.

Conclusiones

Durante el proyecto se ha desarrollado e implementado el modelo de deformación asimétrica de los cables de la *E-sail*, analizando en primer lugar cómo el aumento del voltaje aplicado y la reducción del ángulo del cabeceo suponen una mayor deformación de dichos cables. Tras ello, la simulación de la vela solar bajo control LQR ha permitido analizar la validez de los modelos propuestos, resultando una respuesta de actitud precisa y estable para ángulos de cabeceo de hasta 28 grados, ampliando el rango obtenido en trabajos anteriores asumiendo saturación. Finalmente, se ha sometido a la *E-sail* con controlador LQG a ruido procedente de perturbaciones e instrumentos de medida, logrando mantener un comportamiento aceptable en el rango operativo de maniobra.

Abstract

The Electric Solar Sail (E-sail) is an innovative propellantless propulsion technology for spacecraft, which generates thrust from interaction of long electrically-charged tethers with solar wind ions. This thesis addresses the attitude control problem for E-sails, with the main objective of widening the validity range of recent work ([1], [2]), that are able to perform pitch change maneuvers near a Sun-facing configuration, assuming a symmetrical deformation of all tethers. For this purpose, a non-symmetrical deformed shape model is proposed to allow the tethers deform independently according to relative orientation from Sun and applied voltage, as it would happen in reality. This proposal is then analyzed under LQR control to check the validity range and study the behaviour of the E-sail's control response, and, later, under LQG control to include the effects of disturbances and sensors' noise.

Contents

Notation

A, B	Linearization matrices
$\mathscr{A}$	Auxiliar reference frame
$\mathscr{B}$	Main body reference frame
b_l	Non-dimensional shape coefficient
C_I^B	Director cosine matrix of reference frame $\mathscr{B}$ with respect to $\mathscr{I}$
$\mathbf{d}_k$	Deformed shape position vector for tether k [m]
$(\mathscr{E}, \mathscr{F}, \mathscr{G})$	E-sail's total torque components [Nm]
f_k	Deformed shape function for tether k [m]
$\mathbf{f}$	Non-dimensional movement equations vector
$(F_{x_k}, F_{y_k}, F_{z_k})$	Exerted forces on the tether k root [N]
$h(t)$	Heaviside step function at t
$(\hat{\mathbf{i}}_A, \hat{\mathbf{j}}_A, \hat{\mathbf{k}}_A)$	Unit vectors of auxiliar reference frame
$(\hat{\mathbf{i}}_B, \hat{\mathbf{j}}_B, \hat{\mathbf{k}}_B)$	Unit vectors of body reference frame
$(\hat{\mathbf{i}}_k, \hat{\mathbf{j}}_k, \hat{\mathbf{k}}_k)$	Unit vectors of tether k local reference frame
$(\hat{\mathbf{i}}_I, \hat{\mathbf{j}}_I, \hat{\mathbf{k}}_I)$	Unit vectors of inertial reference frame
Id_n	Identity matrix of order n
I_t	Transversal inertia [kg m^2]
I_z	Axial inertia [kg m^2]
$\mathbf{I}$	Inertia matrix in main body reference frame [kg m^2]
J	LQR/LQG cost function
k	Tether index
K	LQR feedback control gain matrix
K_f	Kalman gain matrix
L	Tether longitude
LQE	Linear Quadratic Estimator
LQG	Linear Quadratic Gaussian regulator
LQR	Linear Quadratic Regulator
m_p	Proton mass [kg]
n	Solar wind ion density [m^{-3}]
$\hat{\mathbf{n}}$	Unit normal vector to E-sail's nominal plane
N	Number of tethers
$N_n(0, V)$	Normal Gaussian distribution with zero mean and covariance V
p_{dyn}	Dynamic pressure exerted by solar wind [Pa]

Q, Q_{end}, R	LQR weighting matrices
r	E-sail's distance from Sun [AU]
$\hat{\mathbf{r}}$	Sun-spacecraft direction unit vector
s_k	Tether's natural curve coordinate [m]
$\hat{\mathbf{s}}_k$	Tether's tangential unit vector
t	Time [s]
t_m	Slew maneuver duration [s]
t^*	Non-dimensional time
T	Transition time from tracking to regulation phase [s]
u	Solar wind velocity [m/s]
Δv	Velocity impulse [m/s]
V	Noise intensity matrix for disturbance accelerations [rad/s^2]
V_k	Tether k voltage [V]
ΔV_k	Control voltage applied to tether k [V]
V_w	Solar wind voltage [V]
W	Noise intensity matrix for gyroscopes' noise [rad/s]
(x_k, y_k, z_k)	Tether's deformed shape coordinates [m]
x_{r_k}	Tether root x_k coordinate [m]
x_{t_k}	Tether tip x_k coordinate [m]
$\mathbf{X}$	Non-dimensional state vector
$\delta\mathbf{X}$	Incremental non-dimensional state vector
α_n	Pitch angle [rad]
δ_n	Clock angle [rad]
ε_0	Vacuum electric permitivity [F/m]
Γ_k	Non-dimensional control coefficient applied to tether k
(ϕ, θ, ψ)	Euler angles [rad]
ρ	Tethers' linear mass density [kg/m]
σ	Nominal voltage coefficient [kg/(m s)]
σ_k	Control voltage coefficient for tether k [kg/(m s)]
ζ_k	Azimuth angle between tether k and first tether [rad]
ω	E-sail's nominal angular velocity [rad/s]
$(\omega_x, \omega_y, \omega_z)$	Non-dimensional angular velocity components
$(\Omega_x, \Omega_y, \Omega_z)$	Angular velocity components of $\boldsymbol{\Omega}^B_{B/I}$ [rad/s]
$\boldsymbol{\Omega}^B_{B/I}$	Angular velocity of frame $\mathscr{B}$ with respect to $\mathscr{I}$ expressed in frame $\mathscr{B}$
$\square'$	Derivative with respect to x_k
$\dot{\square}$	Derivative with respect to time
$\tilde{\square}$	Desired state
$\square_{ref}$	Reference state

1 Introduction

This chapter introduces all fundamental concepts related to E-sails (Section 1.2), beginning with a brief context of propellantless propulsion systems and, in particular, solar sails (Section 1.1). Afterwards, Section 1.3 describes the state of art of E-sails' architecture and applications, while Section 1.3.3 is focused on advances in E-sails' attitude control, which is the core of the project. Finally, the objective and structure of this work is exposed in Sections 1.4 and 1.5.

1.1 Introduction to solar sails

Last decades, some new propellantless propulsion technologies have been object of study in order to overcome the limitations of traditional propellant-based systems. As on-board stored propellant increases total spacecraft mass, this increases overall mission costs. In addition, mission lifetime is limited since an adequate orbital maintenance would require corrective maneuvers that are directly linked to propellant availability [1].

Related to this project, two propellantless propulsion technologies are highlighted, namely: photonic solar sails and magnetic sails. Focusing on solar sails, the generated thrust is produced, in this case, through momentum exchange with incoming solar photons (i.e. solar radiation pressure), which are reflected by a thin membrane. A variety of solar sails' architectures have been proposed, all sharing the same already mentioned fundamental operating principles [3]. They can be categorized according to two main aspects: the shape of solar sail membranes and the need of supporting structure.

Thus, on the one hand, rigid solar sails are those that require rigid structural support spars connected to the membrane edges to maintain them deployed with the desired shape. As an example, Figure 1.1 shows three different variants of rigid solar sails depending on the membranes shape and number of spars required. The advantage of this type of sails is that the stuctural supports reduce membrane flexibility, that are usually considered as disturbances, and are also prone to apply a wide spectrum of attitude control strategies.

On the other hand, non-rigid solar sails (also known as spin sails) keep the membranes deployed by means of tension generated by centrifugal forces resulting from the spacecraft spin itself. Two types of spin sails are mainly mentioned in this category (Figure 1.2): disk-type solar sails consists of a large sheet of sail membrane deployed around and from a central hub, whereas an heliogyro solar sail presents long thin strips attached to the hub resembling the rotor blades of a helicopter. As compared to rigid solar sails, spin sails show a more favourable mass to membrane area ratio, therefore being able to generate larger accelerations; however, membranes deployment and attitude control require a more comprehensive study due to flexibility effects.

To conclude, solar sailcraft technology has succesfully demonstrated its potential by means of recent solar sail-based missions, such as IKAROS (2010) or LightSail-2 (2019).

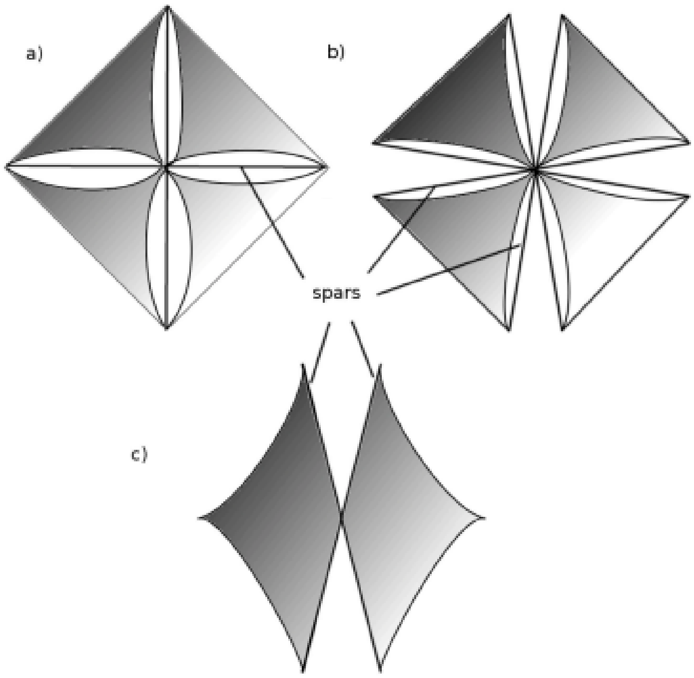

Figure 1.1 Rigid solar sail variants: clipper (a), quad (b) and butterfly (c) [3].

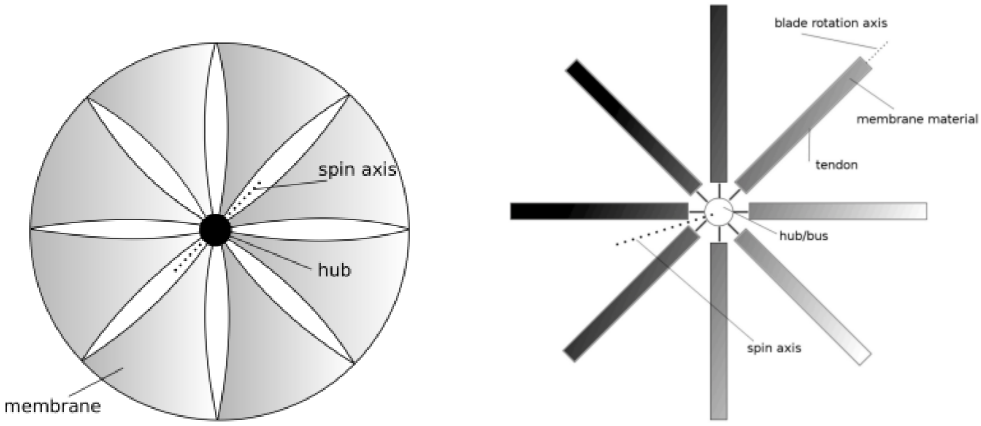

Figure 1.2 Non-rigid solar sail variants: disk sail (left) and heliogyro (right) [3].

1.2 The E-sail concept

In this context, the Electric Solar Wind Sail (E-sail) concept was first conceived in 2004 by the Finnish space physicist, astrobiologist and inventor Pekka Janhunen [4]. An E-sail is a spacecraft composed by a large grid of tethers maintained at a high positive electrical charge, causing a surrounding electrostatic field which extracts momentum from the incoming solar wind ions (i.e. solar dynamic pressure) and, therefore, leading to generation of continuous thrust. This working principle is similar to other technologies proposed at that time, in which Janhunen based his original idea, namely photonic solar sails (specially non-rigid or spin solar sails) and magnetic sail concepts.

Then, which are the strengths of E-sails as compared with their propellantless competitors? On the one hand, it is known that, at a distance of 1 AU (i.e. the distance from Sun to Earth), solar dynamic pressure (about 2 nPa) is approximately 5,000 times weaker than solar radiation pressure (about 9 μPa) [5]. However, if an E-sail is constructed with a mesh of wires with a separation distance comparable to the Debye length of solar wind plasma (i.e. the distance at which plasma screens the E-sail electrostatic field) and charged with a high positive electric voltage, protons will see an impenetrable surface with greater effective area. As a result, E-sails may have greater surface areas with lower weights possible, counteracting the previous difference in thrust generation, and finally leading to comparable accelerations with respect to photonic solar sails.

On the other hand, there is one of the most promising characteristics of E-sails, that makes them interesting and feasible for interplanetary missions far from Sun. While the thrust generated by photonic solar sails decays with the inverse of the distance to Sun squared ($1/r^2$), E-sails produce a thrust proportional to $1/r$ instead.

1.3 State of the art

Once the E-sail concept has been introduced, the aim of this section is to summarize the current state of this innovative propulsive technology. For this purpose, the main components will be described, together with a brief analysis of the orders of magnitude of key performance indicators, such as consumption and propulsive forces. Besides, this section shows the potential applications under research and, finally, the different approaches to attitude control techniques for E-sails.

1.3.1 E-sail architecture

As stated in Section 1.2, the working principle of E-sails for thrust generation is based on electrostatic interaction between positive charged tethers and the ions of solar wind plasma, being the force acting on each tether proportional to the tether voltage. In order to perform this main feature, several tether arrangements have been proposed along time, starting from the original Janhunen's proposal of a wire mesh as shown in Fig. 1.3.

Additionally, most spacecraft missions require the capability of attitude change in order to adjust the direction of the thrust vector. On an E-sail, it is possible to take advantage of potential modulation for each tether, in a synchronous way with the spacecraft rotation, to create the necessary torque to achieve the desired orientation. However, it is crucial to take into account that the generated transverse thrust may induce different angular velocity change for each tether, also being affected by Coriolis forces and solar wind velocity fluctuations. This phenomena increases the risk of tether collision and led to a reformullation of the original tether arrangement.

At the present, the typical electric solar sail configuration is made up of a number of radial main tethers, whose tip hosts a remote unit, connected by auxiliary tethers forming an external circle centered on the spacecraft spin axis. This architecture, depicted on Fig. 1.4, has been found to be useful to overcome the problem of stability of the complex cable system and risk of collision between tethers [6].

Beginning with main tethers, they are quite long cables (typically around 2 km) subject to high positive electrostatic potential, which is maintained through an onboard electron gun, which is

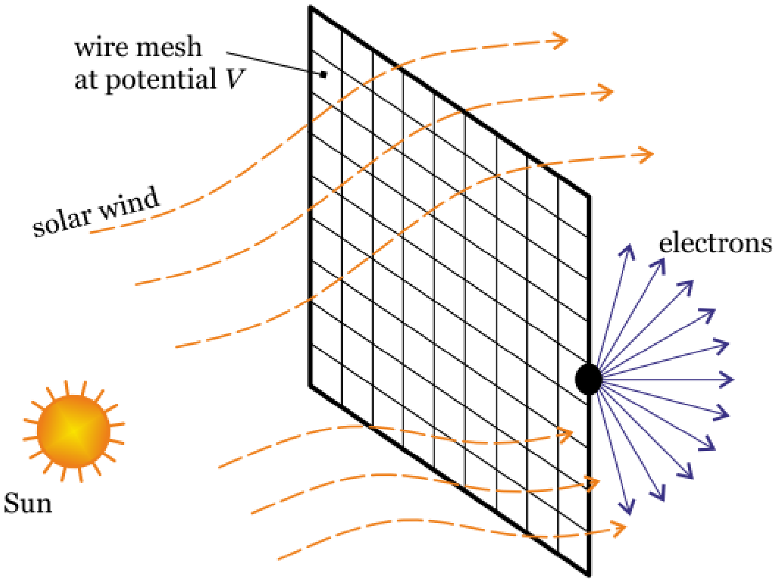

Figure 1.3 Original wire mesh arrangement for E-sail [1].

capable of repelling the negative charge attracted by interaction with solar wind plasma ions. Each tether is composed by four cables of conductive material such as aluminum, where one of them is straight and is surrounded by the three remaining cables with loops, and presents a relatively low linear mass density (typically $\rho = 1.155 \cdot 10^{-5}$ kg/m) [2].

As stated before, a remote unit (RU), together with the main tether reel assembly, is located at the tip of each main tether. These remote units may include small thrusters that produce the required initial impulse for tether deployment and, also, to control the rotation of the tethers during operation. In addition, controllers and sensors should be attached around the spacecraft, in order to locate each RU with its respective main tether, between other functionalities.

Finally, the remote units are connected by a cable with a longitude nearly equal to that of a circumference of radius equal to the main tether longitude. This auxiliary tether does not need to be electrically charged and its objective is to avoid collisions between adjacent main tethers. For simplification purposes, we will not consider its presence for the spacecraft dynamics.

1.3.2 Potential applications

Related with some characteristics already mentioned about electric solar sails, it can be stated that this new propulsive method shows the following main advantages: it avoids the limitation of missions due to outage of propellant and its capability of providing thrust is extended throughout (almost) all the Solar System. However, there are also some issues related to the tethers' deployment and resistance, voltage source and electromagnetic compatibility, between others, which are into study and implementation.

Consequently, the possible applications that E-sails may have (analized in [7]) are:

Asteroids and terrestrial planets missions

First of all, we can highlight the use of electric solar sails in missions to Venus. This planet, the closest to Earth, offers relatively easy access in terms of required impulse Δv. Studies have shown that E-sails can provide the necessary impulse to place a spacecraft in a Venusian orbit in a time

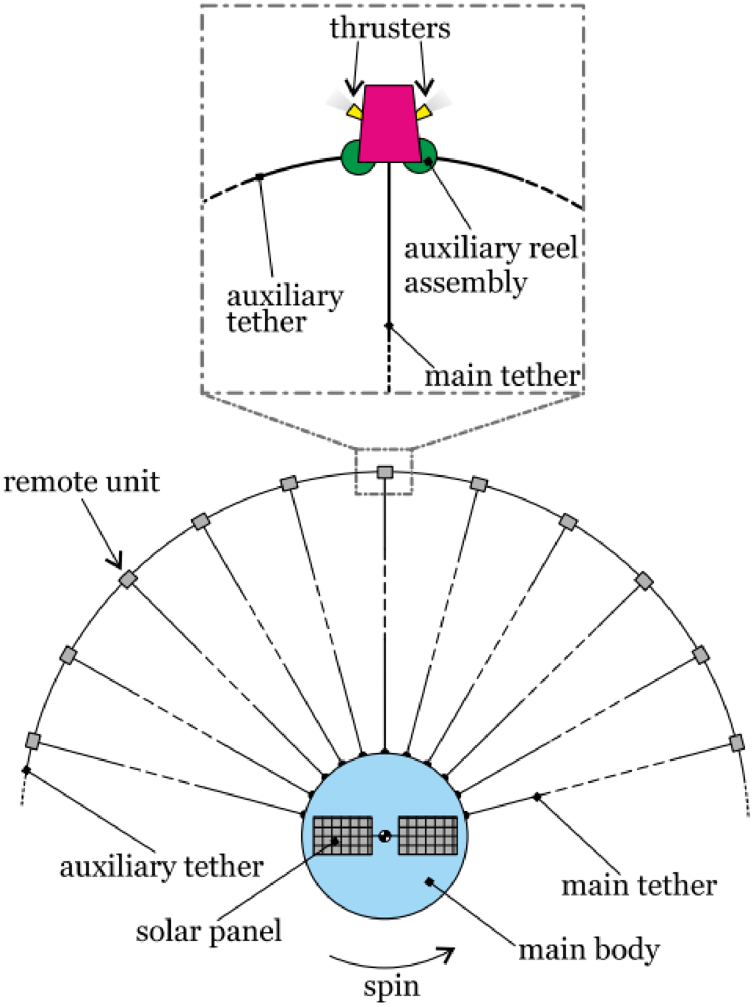

Figure 1.4 Typical E-sail configuration with remote units and auxiliary tethers [1].

similar to that required for a Hohmann transfer. This offers the advantage of not requiring fuel and reducing the overall weight of the mission.

Secondly, the use of electric solar sails on Mars missions also offers significant benefits. For example, in a transfer to low Mars orbit, the use of an electric solar sail can save 1.1 km/s momentum and eliminate the need for aerobraking. Additionally, on return-to-Earth missions from Phobos, a moon of Mars, the use of an electric solar sail can save up to 3.8 km/s in Δv and allow for smoother reentry. Compared to electric propulsion, E-sails offer similar or even greater thrust without the need for propellant, just requiring a reasonable amount of electrical power.

Focusing on the planets near Earth, the impact of the use of E-sails in missions to Mercury can also be analyzed. Since Mercury is very close to the Sun, the probes that approach this planet are strongly affected by the solar gravitational field. However, using an electric solar sail as the propulsion system can reduce transfer time by up to six times compared to missions using chemical and ion propulsion, such as the BepiColombo mission. In this type of missions close to the Sun, the tolerance of the materials of the conductive cables (tethers) to high temperatures must be taken into account, which may require additional cooling systems.

Non-Keplerian orbits

The use of electric solar sails in space missions offers interesting possibilities in the study of non-Keplerian orbits, such as Halo orbits around Lagrange points. These sails provide greater thrust than other methods of propulsion and could replace the need to constantly burn fuel to maintain unstable orbits. In addition, they allow the study of phenomena such as auroras and the effects of the solar wind on planets like Jupiter as they are located above the L1 point, avoiding the need to use multiple vehicles and withstand high levels of radiation.

However, the presence of conductive cables disturbs the measurement of solar plasma, which requires the development of new measurement systems to overcome this challenge. In summary, electric solar sails present exciting opportunities and technological challenges in space exploration, enabling greater efficiency and observation capabilities in non-Keplerian orbits and the study of space phenomena.

Near Sun missions

Missions near the Sun are usually expensive in terms of impulse Δv, which can be as much as 15 km/s (depending on the type of target orbit). However, in an E-sail, the thrust increases as the distance from the Sun decreases. This means that in a mission with a shorter distance from the Sun, the electric sail can provide more thrust compared to a distance of 1 AU. However, this also increases the power consumption of the electron gun and the degradation of the solar panels due to high temperatures. Therefore, incorporating E-sails into these types of missions can pose technological challenges.

One-way boosting to outer solar system

Due to the nature of the hardware used, the operational range of E-sails in relation to their proximity to the Sun is 0.9-4 AU. However, it is feasible to extend this limit to 0.9-8 AU with minimal alterations in the component specifications, as long as the electric sail does not have to carry an excessively heavy load (between 1-1.5 tons) and is Keep the Sun as a power source. In addition, in the event that the load requires an additional energy source, such as nuclear, this can also be used to improve the performance of the electric candle. An additional advantage of this propulsion system is the possibility of increasing the number of launch opportunities, which would allow certain missions to be carried out more frequently.

Impactors and data clippers

The "data clippers" are defined as space vehicles whose objective is to approach the Earth, carrying in their memory a large volume of high-resolution scientific data. These scientific data can be downloaded by terrestrial antennas when these vehicles are in the vicinity of the Earth. The E-sails can intervene in this type of missions as a propulsion mechanism, minimizing the cost of the missions by making the trip without consuming propellant.

1.3.3 Attitude control

This project will be focused on the E-sail attitude control, whose main (and essencial for maneuvering) function is to orientate the thrust vector during the space mission. In this subsection, different strategies for regulation and control of the electric solar sail attitude and its spin rate are briefly exposed.

Firstly, Janhunen proposed in 2013 a simple dynamical model of the tether [8], described as a spherical pendulum rotating under the constant action of the solar wind. Based on this model, he suggested to apply an auxiliary propulsion to the tips of the main tethers, as for example small photonic blades, which may be capable of counteracting the Coriolis effect. This idea was shown to provide enough spin control capability, with the benefit of keeping the spacecraft fully propellantless, which is one of the key points of E-sails.

Also in 2013, Toivanen and Janhunen [9] studied another strategy for E-sail attitude control, which consists in individual modulation of the voltage of each tether in order to generate the desired net torque on the whole E-sail. In subsequent work [10], the authors conceived a model capable of estimating the thrust and torque vectors through an approximate expression of the tether deformed shape. These ideas allowed to succesfully compute the necessary voltage modulation for attitude maintenance under stationary solar conditions, which was shown to be even lower when considering a flexible tether instead of a rigid one, as well as to estimate the fraction of electron gun power to be reserved for attitude control.

More recent works continue studying the tether voltage modulation strategy and develop the initial proposal to more realistic scenarios. Firstly, Bassetto et al. [11]-[12] deepened on the analysis of tether deformation due to combined effects of solar wind dynamic pressure and centrifugal force, which was found to generate a disturbing torque. This torque tends to realign the thrust vector with the Sun-spacecraft line, seriously affecting the maneuvring capabilities of the E-sail, and it is only zero when the spacecraft is in a Sun-facing condition (i.e., with its spin axis fully parallel to Sun-spacecraft line).

Finally, we summarize the most recent progress. On the one hand, Li et al. [13] studied an E-sail model based on the nodal position finite element method in order to analyze the coupling effects between elastic dynamics of the tethers and the electric field. The author demonstrated that maneuverability is improved with a greater number of tethers, but decreases in face of an increase of the tether length, the sail spin rate and the mass of remote units. Besides, Du et al. investigated the dynamics of high-order modes of flexible elastic wires [14] and the modeling of rigid-flexible coupling effects on attitude dynamics and control [15]. On the other hand, Huang et al. [16] were devoted to study the attitude dynamics and control of a barbell E-sail, another E-sail configuration consisting in two tip satellites connected through long conductive tethers, insulated at the central point in such a way that their electrical voltages can be controlled independently.

1.4 Objective and scope of the project

The aim of this project is to study the control of an E-sail's attitude change maneuver, under the hypothesis and assumptions made in Chapter 2. In more detail, this project is based on the simplified and analytical model for symmetrical and Sun-facing configuration proposed by Bassetto et al. [11]-[12] and its LQR control application in [2]. Thus, the main objective is to widen the scope of these works to non-symmetrical configuration model (i.e., tethers present a different deformed shape between them depending on the voltage modulation and the attitude) and, then, check its validy for a greater interval of desired final pich angles.

In this way, the work is orientated in order to obtain two main achievements. On the one hand, to propose and study a more complete analytical model for tether's deformed shape for non-symmetrical configuration, and compare it with the original proposed in [11] in different conditions of voltage modulation and attitude. On the other hand, to design a control law for a pitch change maneuver, based on LQR method, applying this new suggested model, and perform a comparative study of the obtained results with respect to the simplified model used in [2], in order to check the validity range of the new proposed model. Additionally, a LQG controller is also considered to study the effects of noise and disturbances in the E-sail's control.

1.5 Structure

To conclude this introduction, the subsequent structure of this document is presented, summarizing the content of each chapter.

Firstly, Chapter 2 is dedicated to perform a thorough exposition of the theoretical concepts related to the E-sail and attitude dynamaics, divided in two different sections. On the one hand, the E-sail's basic model is defined, explaining all the hypothesis, the proposal of tether deformed shape model in non-symmetrical configuration and, finally, the torque dynamics according to these assumptions. On the other hand, the second section summarizes the attitude fundamentals; this is, attitude representation through Euler angles, kinematics and dynamics, particularizing the equations to E-sail's model previously defined. Finally, a third section condenses the state and control variables, together with the applicable movement equations for attitude, in non-dimensional way.

Subsequently, Chapter 3 is related to control law design to achieve a certain final attitude by performing a pitch change maneuver. For this purpose, two control problems are posed: a Linear Quadratic Regulator (LQR), which is aimed to follow a certain reference trajectory and, furthermore, Linear Quadratic Gaussian control (LQG), which fits a Kalman filter to the previous LQR controller in order to handle noise related to measurements and system disturbances. Besides, as these two control problems require the system dynamics to be linear with respect to the state and control variables, then a section is dedicated to this linearization around a certain defined reference.

After that, several results are obtained and presented in Chapter 4 to validate the models previously defined. Thus, a first section aims to illustrate the non-symmetrical tether deformed shape model and analyze how the related shape coefficient depends on the attitude and the control power applied to each tether. Next, the E-sail with LQR controller is simulated under several maneuver with different final pitch angles, in order to check the limits of validity and study the control response behaviour. Comparably, a certain noise is added to test the LQG controller in similar terms.

Lastly, the main conclusions deduced from the work performed during this project are summarized in Chapter 5.

2 Theoretical background

All theoretical background regarding general assumptions and dynamics of an E-sail, as well as attitude concepts, is described in this chapter. On the one hand, Section 2.1 exposes, in the following order, the general hypothesis, parameters and reference frames used to define the basic model for the electric solar sail, the tethers' deformed shape model and, finally, the dynamic model. On the other, attitude representation, kinematics and dynamics are described in Section 2.2, finally sumarizing the movement equations and non-dimensional variables in Section 2.3.

2.1 E-sail's basic model

2.1.1 Reference frames and hypothesis

As general hypothesis during this project, the E-sail-based spacecraft is considered to have a certain number of tethers, $N \geq 2$, which are modelled as two-dimensional cables contained in plane $(\hat{\mathbf{i}}_k, \hat{\mathbf{n}})$. All these tethers, in their undeformed state (i.e., as straight wires), define the sail nominal plane, from which the vector $\hat{\mathbf{n}}$ is perpendicular.

In this context, k denotes the index corresponding to each tether (integer from 1 to N), and a local reference frame for each tether k is defined, being: $\hat{\mathbf{i}}_k$ pointing towards the tip of tether k, $\hat{\mathbf{k}}$ parallel to $\hat{\mathbf{n}}$, and $\hat{\mathbf{j}}_k$ completing a right-hand reference frame centered at the spacecraft's center of mass, S.

In addition, the spacecraft is assumed to behave as a rigid body, initially rotating around normal unit vector to sail nominal plane, $\hat{\mathbf{n}}$, with a constant angular velocity $\omega = 0.0758$ rad/s. Associated with this rigid body model, some geometric properties of the E-sail are enumerated below:

- Tether longitude: $L = 2\,000$ m.
- Tether linear density: $\rho = 1.155 \cdot 10^{-5}$ kg/m.
- Inertia matrix in principal body axes, assuming axial symmetry around $\hat{\mathbf{k}}_B$ (it will be seen hereunder that is coincident with $\hat{\mathbf{n}}$): $I_t = 1\,000$ kg m^2 and $I_z = 3\,000$ kg m^2, with

$$I = \begin{bmatrix} I_t & 0 & 0 \\ 0 & I_t & 0 \\ 0 & 0 & I_z \end{bmatrix}.$$

Regarding the electric properties from the tethers and the solar wind that actually provide the propulsive forces in an E-sail, the following is assumed. On the one hand, all tethers will be subject to a certain nominal potential $V = 16.5$ kV needed for desired propulsive thrust. At the same time, a modulation ΔV_k can be applied to each tether for attitude control purposes, as will be analyzed during this project, leading to a different voltage for each tether: $V_k = V_w + \Delta V_k$.

On the other hand, solar wind at a distance of 1 AU from Sun is characterized by a typical electric potential of $V_w = 1$ kV and a velocity $u = 400$ km/s. Taking into account that dynamic pressure exerted by solar wind at that distance is $p_{dyn} = 2$ nPa and, together with the previous properties, the positive ion mass density (particle density n times proton mass m_p) is directly estimated from:

$$p_{dyn} = nm_p u^2 \Longrightarrow nm_p = \frac{p_{dyn}}{u^2}. \tag{2.1}$$

Besides, the attitude representation requires the use of the following reference frames:

- **Principal body reference frame ($\mathscr{B}$).** It is directly linked to the spacecraft, jointly moving with it, centered at its center of mass S, according to Figure 2.1. The unit vectors that define this reference frame are: $\hat{\mathbf{i}}_B$ aligned with first tether ($k = 1$) in its undeformed shape, $\hat{\mathbf{j}}_B$ normal to the previous unit vector and contained in the sail nominal plane, and $\hat{\mathbf{k}}_B$ normal to this plane and coincident with $\hat{\mathbf{n}}$.

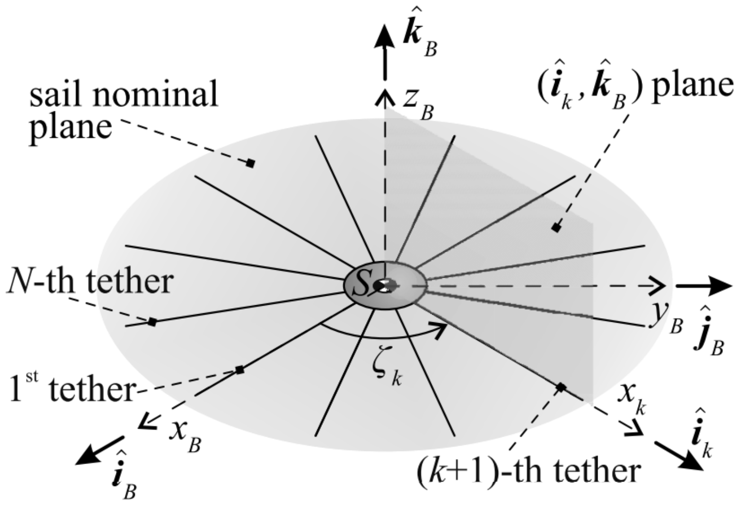

Figure 2.1 Body reference frame and main geometry of E-sail's tethers [12].

- **Inertial reference frame ($\mathscr{I}$).** It is actually a inertial reference frame with origin at the E-sail's center of mass, whose base of unitary vectors $(\hat{\mathbf{i}}_I, \hat{\mathbf{j}}_I, \hat{\mathbf{k}}_I)$ is coincident with those of body reference frame $\mathscr{B}$ at initial state (when the spacecraft is assumed to have a sail nominal plane perpendicular to solar wind).
- **Auxiliary reference frame ($\mathscr{A}$).** This non-inertial reference system is used to express the pitch angle (α_n) evolution during the attitude change maneuver, between I and B. For this aim, unit vector $\hat{\mathbf{j}}_A$ is always coincident with $\hat{\mathbf{j}}_I$; and the other vectors $\hat{\mathbf{i}}_A$ and $\hat{\mathbf{k}}_A$ result from a rotation of reference frame I around $\hat{\mathbf{j}}_I$ with an angle α_n.

Finally, it is important to define three angles directly involved in E-sail's dynamics model and repeteadly used throughout this document. On the one hand, azimuth angles ζ_k quantifies the angle between tether k and the first tether $k = 1$ (or equivalently x_B), measured counterclockwise inside the sail nominal plane:

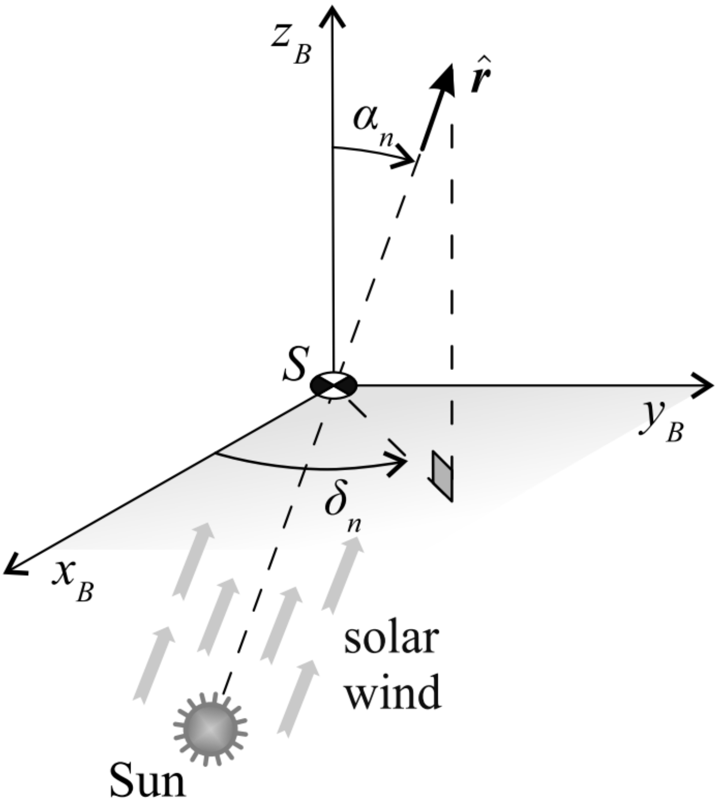

Figure 2.2 Definition of pitch and clock angles [12].

$$\zeta \triangleq \left(\frac{2\pi}{N}\right)(k-1). \tag{2.2}$$

These azimuth angles allow to stablish a relationship between local unit vectors for each tether and body axes, and viceversa:

$$\begin{aligned} \hat{\mathbf{i}}_B &= \cos\zeta_k \hat{\mathbf{i}}_k - \sin\zeta_k \hat{\mathbf{j}}_k, \\ \hat{\mathbf{j}}_B &= \sin\zeta_k \hat{\mathbf{i}}_k + \cos\zeta_k \hat{\mathbf{j}}_k, \\ \hat{\mathbf{k}}_B &= \hat{\mathbf{k}}_k. \end{aligned} \tag{2.3}$$

On the other hand, the E-sail orientation is defined by two angles with respect to local solar wind velocity direction $\hat{\mathbf{r}}$, according to Figure 2.2. First, sail pitch angle $\alpha_n \in [0,\pi/2]$ rad is the angle between Sun direction $\hat{\mathbf{r}}$ and the spacecraft axis z_B:

$$\alpha_n \triangleq \arccos(\hat{\mathbf{r}} \cdot \hat{\mathbf{k}}_B). \tag{2.4}$$

Secondly, clock angle $\delta_n \in [0,2\pi)$ rad is the angle between x_B axis and the projection of Sun direction $\hat{\mathbf{r}}$ on the sail nominal plane, and is computed from:

$$\delta_n \triangleq \begin{cases} \arccos\left(\dfrac{\hat{\mathbf{r}} \cdot \hat{\mathbf{i}}_B}{||\hat{\mathbf{r}} \times \hat{\mathbf{k}}_B||}\right) & \text{if} \quad \hat{\mathbf{r}} \cdot \hat{\mathbf{j}}_B \geq 0, \\ 2\pi - \arccos\left(\dfrac{\hat{\mathbf{r}} \cdot \hat{\mathbf{i}}_B}{||\hat{\mathbf{r}} \times \hat{\mathbf{k}}_B||}\right) & \text{if} \quad \hat{\mathbf{r}} \cdot \hat{\mathbf{j}}_B < 0. \end{cases} \tag{2.5}$$

Hence, the unit vector describing the local solar wind direction can be expressed, in body axes, depending on these two orientation angles:

$$\hat{\mathbf{r}} = \sin\alpha_n \cos\delta_n \hat{\mathbf{i}}_B + \sin\alpha_n \sin\delta_n \hat{\mathbf{j}}_B + \cos\alpha_n \hat{\mathbf{k}}_B. \tag{2.6}$$

2.1.2 Tether deformed shape model

One of the main points of this project is to assume that tethers are able to deform due to interaction by means of different forces. In this context, many works are aimed to analyze the tethers' deformation, either numerically or analytically.

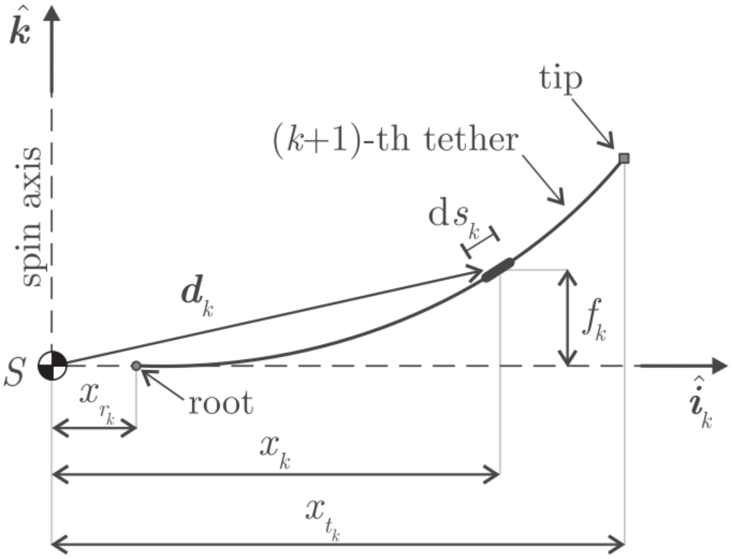

Figure 2.3 Geometry of a planar tether deformed shape [11].

From now on, the general geometry described in Figure 2.3 is to be considered for a tether k deforming in its plane (x_k,z_k), neglecting any transversal displacement y_k. In order to clarify in a simple way the new magnitudes involved, they are enumerated below:

- Tether's root x_k coordinate (x_{r_k}). A tether is typically attached to the spacecraft really close to its center of mass, and the distance to S, as compared to the great tether's length (in the order of kilometers), allows to neglect it, hence: $x_{r_k} \simeq 0$.
- Tether's tip x_k coordinate (x_{t_k}). Specially in a Sun-facing configuration, tethers' deformation in z_k is quite small (in the order of meters) as compared to tethers' length (in the order of kilometers), so it will be considered that $x_{t_k} \simeq L$. However, to expose the deformed tether shape model in this section, it is kept.
- Deformed shape function $f_k(x_k)$. It describes the displacement of a tether's point located at x_k in direction z_k.
- Position vector $\mathbf{d}_k$. This vector has its origin at spacecraft's center of mass S and ends on each point of the deformed shape's curve:

$$\mathbf{d}_k = x_k \hat{\mathbf{i}}_k + f_k \hat{\mathbf{k}}_k. \tag{2.7}$$

- Tether's natural curve coordinate (s_k). It is the distance from the root $s_k = 0$ to each point of the tether's deformed curve. Each differential segment of the curve is analyzed as a differential $\mathrm{d}s_k$, related with f_k throughout the following expression:

$$\mathrm{d}s_k = \sqrt{1+(f_k')^2}\mathrm{d}x_k. \tag{2.8}$$

- Tether's tangential unit vector ($\hat{\mathbf{s}}_k$). It can be computed from the differential of the position vector $\mathrm{d}\mathbf{d}_k$ divided by the differential curve distance $\mathrm{d}s_k$:

$$\hat{\mathbf{s}}_k = \frac{\mathrm{d}\mathbf{d}_k}{\mathrm{d}s_k} = \frac{\mathrm{d}x_k\hat{\mathbf{i}}_k + \mathrm{d}f_k\hat{\mathbf{k}}_k}{\sqrt{1+(f_k')^2}\mathrm{d}x_k} = \frac{\hat{\mathbf{i}}_k + f_k'\hat{\mathbf{k}}_k}{\sqrt{1+(f_k')^2}}. \tag{2.9}$$

For our puroposes, we will focus on one particular model, proposed in [11], whose application is valid for an axisymmetric E-sail with a Sun-facing configuration (i.e., with a reduced pitch angle α_n). However, with the aim of widening the application to non-symmetric operation, it will be considered that each tether has its own deformed shape function, differing from the original model, where all tethers would show the same deformation.

This model consists in a simple logarithmic function for $f_k(x_k)$, modulated by a non-dimensional shape coefficient b_{l_k} for each tether describing the tether slope at the root $x_k = 0$:

$$f_k(x_k) = b_{l_k} L \ln\left(1+\frac{x_k}{x_{t_k}}\right), \tag{2.10}$$

$$f_k'(x_k) = \frac{b_{l_k}}{1+\frac{x_k}{x_{t_k}}}, \tag{2.11}$$

$$f_k'(x_k = 0) = b_{l_k}. \tag{2.12}$$

In order to complete the model based on Equations (2.10)-(2.12), it is necessary to compute both the shape coefficients (b_{l_k}) and tip coordinates (x_{t_k}) for each tether. To do so, a system of equations is solved numerically, containing two groups of equations:

- For x_{t_k} calculation, we use the definition of total lenght in curve coordinates; however, this will only be used to check the hypothesis $x_{t_k} \simeq L$ and, after this system of equations, that consideration is to be applied to subsequent expressions:

$$L = \int_{s_k(0)}^{s_k(x_{t_k})} \mathrm{d}s_k(x_k) = \int_0^{x_{t_k}} \sqrt{1+(f_k')^2}\mathrm{d}x_k = \int_0^{x_{t_k}} \sqrt{1+\left(\frac{b_{l_k}}{1+\frac{x_k}{x_{t_k}}}\right)^2}\mathrm{d}x_k. \tag{2.13}$$

- In the case of shape coefficients, the procedure and considerations followed in [11] are applied, but not enforcing Sun-facing conditions. Therefore, assuming that the tether does not have bending stiffness, only internal tension acts tangential to its neutral axis. Consequently, the tangent vector on any point P of the tether has the same direction of the integral of the differencial force from P to the tether tip. Translated to tether slope in $x = 0$ (which is equivalent to the shape coefficient) and, neglecting the transversal forces, b_{l_k} are computed from:

$$b_{l_k} = f_k'(x_k = 0) = \frac{F_{z_k}}{F_{x_k}}, \tag{2.14}$$

where the forces are:

$$\begin{aligned} F_{x_k} &= \int_{F_{x_k}(0)}^{F_{x_k}(x_{t_k})} \mathrm{d}F_{x_k}(x_k), \\ F_{z_k} &= \int_{F_{z_k}(0)}^{F_{z_k}(x_{t_k})} \mathrm{d}F_{z_k}(x_k). \end{aligned} \tag{2.15}$$

To finalize, it is fundamental to define a proper model for the forces acting on a tether. Between all forces (gravity, structural bonding to spacecraft, elastic and damping forces, that are not assumed in this project, as done in [11]), two interactions are mainly considered to affect the tether shape and its dynamics:

- Inertial forces due to Coriolis' effect associated to spin around z_k axis:

  $$\mathrm{d}\mathbf{F}_{\omega_k} = \rho \,\mathrm{d}s_k x_k \omega^2 \hat{\mathbf{i}}_k, \tag{2.16}$$

- Coulomb forces due to electrostatic interaction of charged tethers with solar wind ions (dynamic pressure provoked by solar wind), according to Janhunen and Toivanen's recent works of (at a approximate distance of 1 AU from Sun) [17]:

  $$\mathrm{d}\mathbf{F}_{s_k} = \sigma_k \mathbf{u}_{\perp k} \mathrm{d}s_k, \tag{2.17}$$

  where σ_k is a coefficient computed from difference of potential between the tether (V_k) and solar wind (V_w), and $\mathbf{u}_{\perp k}$ is the component of solar wind velocity perpendicular to the tether's local tangent unit vector, assuming a purely radial solar wind $\mathbf{u} = u\hat{\mathbf{r}}$:

  $$\sigma_k = 0.18 \max(0, V_k - V_w) \sqrt{\varepsilon_0 m_p n}, \tag{2.18}$$

  $$\mathbf{u}_{\perp k} = u(\hat{\mathbf{s}}_k \times \hat{\mathbf{r}}) \times \hat{\mathbf{s}}_k. \tag{2.19}$$

Therefore, the total force exerted on a tether's infinitesimal arc-length $\mathrm{d}s_k$ would be the sum of these two interactions:

$$\mathrm{d}\mathbf{F}_k = \mathrm{d}\mathbf{F}_{\omega_k} + \mathrm{d}\mathbf{F}_{s_k}, \tag{2.20}$$

Expressing the infinitesimal force vector expressed in Equation (2.20) into its three components in local tether coordinates, one obtains the following:

$$\begin{aligned} \mathrm{d}F_{x_k}(x_k) = \Big\{ &\rho \omega^2 x_k + \sigma_k u \big[\sin\alpha_n \cos\delta_n \sin\zeta_k + \sin\alpha_n \sin\delta_n \sin\zeta_k \\ &- \frac{\cos(\delta_n - \zeta_k)\sin\alpha_n + f_k' \cos\alpha_n}{1 + (f_k')^2} \big] \Big\} \sqrt{1 + (f_k')^2} \mathrm{d}x_k, \end{aligned} \tag{2.21}$$

$$\mathrm{d}F_{y_k}(x_k) = \sigma_k u \left[-\sin\alpha_n \cos\delta_n \sin\zeta_k + \sin\alpha_n \sin\delta_n \cos\zeta_k \right] \sqrt{1 + (f_k')^2} \mathrm{d}x_k, \tag{2.22}$$

$$\mathrm{d}F_{z_k}(x_k) = \sigma_k u \left[\cos\alpha_n - \frac{\cos(\delta_n - \zeta_k)\sin\alpha_n f_k' + (f_k')^2 \cos\alpha_n}{1 + (f_k')^2} \right] \sqrt{1 + (f_k')^2} \mathrm{d}x_k. \tag{2.23}$$

Then, it is possible to integrate these magnitudes between the tether root ($x_k = 0$) and tip ($x_k \simeq L$) to compute the components of the total force acting on a tether k:

$$\begin{aligned}F_{x_k} = \rho\omega^2L^2g_1(b_{l_k}) + \sigma_k uL\left\{\sin\alpha_n\cos\delta_n\cos\zeta_k g_2(b_{l_k}) + \sin\alpha_n\sin\delta_n\sin\zeta_k g_2(b_{l_k})\right.\\ \left.-\cos(\delta_n-\zeta_k)\sin\alpha_n g_3(b_{l_k}) - \cos\alpha_n g_4(b_{l_k})\right\},\end{aligned} \tag{2.24}$$

$$F_{y_k} = \sigma_k uL(-\sin\alpha_n\cos\delta_n\sin\zeta_k + \sin\alpha_n\sin\delta_n\cos\zeta_k)g_2(b_{l_k}), \tag{2.25}$$

$$F_{z_k} = \sigma_k uL\left\{\cos\alpha_n g_2(b_{l_k}) - \cos(\delta_n-\zeta_k)\sin\alpha_n g_4(b_{l_k}) - g_5(b_{l_k})\right\}, \tag{2.26}$$

where five auxiliar functions containing the integrals and only depending on shape coefficient b_{l_k} have been defined in order to facilitate comprehension and future calculations (e.g., derivatives with respect to shape coefficient), and considering variable change $x = x_k/L$:

$$\begin{aligned}g_1(b_{l_k}) = \int_0^1 x\sqrt{1+\left(\frac{b_{l_k}}{1+x}\right)^2}\mathrm{d}x = \Bigg(\frac{1}{2}(1+x)\sqrt{(1+x)^2+b_{l_k}^2}\\ +\frac{b_{l_k}^2}{2}\ln\left|\frac{1+x+\sqrt{(1+x)^2+b_{l_k}^2}}{b_{l_k}}\right| + \frac{b_{l_k}}{2}\ln\left|\frac{\sqrt{(1+x)^2+b_{l_k}^2}}{b_{l_k}}+1\right|\\ -\frac{b_{l_k}}{2}\left|\frac{\sqrt{(1+x)^2+b_{l_k}^2}}{b_{l_k}}-1\right| - \sqrt{(1+x)^2+b_{l_k}^2}\Bigg]_{x=0}^{x=1},\end{aligned} \tag{2.27}$$

$$\begin{aligned}g_2(b_{l_k}) = \int_0^1 \sqrt{1+\left(\frac{b_{l_k}}{1+x}\right)^2}\mathrm{d}x = \Bigg(-\frac{b_{l_k}}{2}\ln\left|\frac{\sqrt{(1+x)^2+b_{l_k}^2}}{b_{l_k}}+1\right|\\ +\frac{b_{l_k}}{2}\left|\frac{\sqrt{(1+x)^2+b_{l_k}^2}}{b_{l_k}}-1\right| + \sqrt{(1+x)^2+b_{l_k}^2}\Bigg]_{x=0}^{x=1},\end{aligned} \tag{2.28}$$

$$g_3(b_{l_k}) = \int_0^1 \frac{\mathrm{d}x}{\sqrt{1+\left(\frac{b_{l_k}}{1+x}\right)^2}} = \left(\sqrt{(1+x)^2+b_{l_k}^2}\right]_{x=0}^{x=1}, \tag{2.29}$$

$$g_4(b_{l_k}) = \int_0^1 \frac{\frac{b_{l_k}}{1+x}}{\sqrt{1+\left(\frac{b_{l_k}}{1+x}\right)^2}}\mathrm{d}x = \left(b_{l_k}\ln\left|\frac{1}{b_{l_k}}(x+1+\sqrt{(1+x)^2+b_{l_k}^2}\right|\Bigg|\right]_{x=0}^{x=1}, \tag{2.30}$$

$$g_5(b_{l_k}) = \int_0^1 \frac{\left(\frac{b_{l_k}}{1+x}\right)^2}{\sqrt{1+\left(\frac{b_{l_k}}{1+x}\right)^2}}\mathrm{d}x = \left(b_{l_k}\ln\left|\tan\left(\frac{1}{2}\arctan\left(\frac{1+x}{b_{l_k}}\right)\right)\right|\Bigg|\right]_{x=0}^{x=1}. \tag{2.31}$$

At this point, all the elements needed to solve Equations (2.13) and (2.14) and, thus, to compute both shape coefficients and tethers' tip x_k coordinate, have been exposed.

Finally, it is important to remark that, in an initial Sun-facing configuration, all tethers would have the same deformed shape, thus being:

$$\begin{aligned} \sigma &= 0.18\max(0,V-V_w)\sqrt{\varepsilon_0 m_p n},\\ b_l &= \frac{2\sigma u}{\rho\omega^2 L}. \end{aligned} \tag{2.32}$$

2.1.3 E-sail torque

Before describing the E-sail's attitude dynamic model, it is fundamental to introduce the torque components acting on each tether, which are directly influenced by the previous shape model. According to the assumptions made before, the infinitesimal force acting on a infinitesimal segment of tether k mainly comes from two interactions: Coriolis effect and solar wind dynamic pressure. Hence, the resulting infinitesimal torque at the spacecraft's center of mass (S) is computed from the cross product between the position vector $\mathbf{d}_k$ and that force:

$$\mathrm{d}\mathbf{T}_k = \mathbf{d}_k \times \mathrm{d}\mathbf{F}_k = \mathrm{d}\mathscr{E}_k\,\hat{\mathbf{i}}_B + \mathrm{d}\mathscr{F}_k\,\hat{\mathbf{j}}_B + \mathrm{d}\mathscr{G}_k\,\hat{\mathbf{k}}_B, \tag{2.33}$$

where $[\mathrm{d}\mathscr{E}_k, \mathrm{d}\mathscr{F}_k, \mathrm{d}\mathscr{G}_k]$ are the infinitesimal torque components in principal body reference frame (B):

$$\begin{aligned} \mathrm{d}\mathscr{E}_k = \Bigg\{ & x_k \sin\zeta_k \left[\sigma_k u\cos\alpha_n - \frac{f_k'\sigma_k u(\sin\alpha_n\cos(\delta_n-\zeta_k)+f_k'\cos\alpha_n)}{1+(f_k')^2}\right] \\ & -f_k\sin\zeta_k\left[\rho x_k\omega^2 - \frac{\sigma_k u(\sin\alpha_n\cos(\delta_n-\zeta_k)+f_k'\cos\alpha_n)}{1+(f_k')^2}\right] - f_k\sigma_k u\sin\alpha_n\sin\delta_n\Bigg\}\sqrt{1+(f_k')^2}\,\mathrm{d}x_k, \end{aligned} \tag{2.34}$$

$$\begin{aligned} \mathrm{d}\mathscr{F}_k = \Bigg\{ & -x_k \cos\zeta_k \left[\sigma_k u\cos\alpha_n - \frac{f_k'\sigma_k u(\sin\alpha_n\cos(\delta_n-\zeta_k)+f_k'\cos\alpha_n)}{1+(f_k')^2}\right] \\ & +f_k\cos\zeta_k\left[\rho x_k\omega^2 - \frac{\sigma_k u(\sin\alpha_n\cos(\delta_n-\zeta_k)+f_k'\cos\alpha_n)}{1+(f_k')^2}\right] + f_k\sigma_k u\sin\alpha_n\cos\delta_n\Bigg\}\sqrt{1+(f_k')^2}\,\mathrm{d}x_k, \end{aligned} \tag{2.35}$$

$$\mathrm{d}\mathscr{G}_k = \sigma_k u x_k \sin\alpha_n\sin(\delta_n-\zeta_k)\sqrt{1+(f_k')^2}\,\mathrm{d}x_k. \tag{2.36}$$

In order to obtain the total E-sail's torque in its center of mass, it is necessary to integrate $[\mathrm{d}\mathscr{E}_k, \mathrm{d}\mathscr{F}_k, \mathrm{d}\mathscr{G}_k]$ along local coordinate x_k to compute the total torque due to tether k and, finally, one has to sum the contributions of all N tethers:

$$\mathbf{T}_k = \int_{T_k(0)}^{T_k(L)} \mathrm{d}\mathbf{T}_k(x_k), \tag{2.37}$$

$$\mathbf{T} = \sum_{k=1}^{N}\mathbf{T}_k. \tag{2.38}$$

This torque model is valid for general E-sail attitude configurations (within the hypothesis described in Section 2.1.1 and Section 2.1.2); however, the integration and derivation of Equations (2.34), (2.35) and (2.36) require the use of numerical methods. Since these computations are necessary afterwards for control law design; for this purpose only, we will consider also the simplified analytical expressions for torque components in [12]:

$$\mathscr{E}_k = uL^2\sigma_k \left\{ b_{l_k} \sin\alpha_n \left[\cos(\delta_n - \zeta_k)\sin\zeta_k(\ln 8 - 2) - \sin\delta_n(\ln 4 - 1)\right] + \frac{\cos\alpha_n \sin\zeta_k}{2} \right\}, \tag{2.39}$$

$$\mathscr{F}_k = uL^2\sigma_k \left\{ b_{l_k} \sin\alpha_n \left[\cos\delta_n(\ln 4 - 1) - \cos(\delta_n - \zeta_k)\cos\zeta_k(\ln 8 - 2)\right] - \frac{\cos\alpha_n \cos\zeta_k}{2} \right\}, \tag{2.40}$$

$$\mathscr{G}_k = uL^2\sigma_k \left\{ \frac{\sin(\delta_n - \zeta_k)\sin\alpha_n}{2} \right\}. \tag{2.41}$$

These expressions were initially proposed for Sun-facing conditions and symmetrical operation (all tethers have the same deformed shape and, thus, equal shape coefficient). Nevertheless, we have already introduced b_{l_k} instead to have an approach to non-symmetrical operation.

2.2 Theory of attitude dynamics

This section summarizes all the concepts related to attitude representation, kinematics and dynamics [18], particularly focusing on the E-sail's attitude using Euler angles, according to the model exposed in Section 2.1.

2.2.1 Attitude representation

A spacecraft's (or any other vehicle or object) attitude is defined as its relative orientation with respect to a certain reference frame. In this particular case, the E-sail attitude is the orientation of the principal body reference frame with respect to the inertial reference frame, considering the spacecraft as a rigid body.

Attitude can be represented using many mathematical constructions defined by a given number of parameters, such as: Euler angles, Director Cosine Matrix (DCM), Euler's angle and axis, quaternions, Rodrigues parameters, etc. Each representation has different particularities and there exist transformation relationships between them; hence, one may choose an attitude representation whose characteristics better fits in the problem to be solved.

In this context, it is important to remark that an attitude representation method may show two particularities. On the one hand, a representation is said to present ambiguities when at least two different combinations of parameters actually represent the same attitude. On the other hand, minimal representations (i.e., representations that use only 3 parameters) always have singularities. Both the ambiguities and singularities can be avoided by reducing the total possible set of parameters to the so-called "shadow set".

Regarding E-sail attitude representation, in this project we will use Euler angles $\{\phi,\theta,\psi\}$ with the following rotational sequence $3(\psi) \to 1(\phi) \to 2(\theta)$, as done in [12]:

$$\mathscr{I} \xrightarrow[z_I]{\psi} S_1 \xrightarrow[x_{S_1}]{\phi} S_2 \xrightarrow[y_{S_2}]{\theta} \mathscr{B}, \tag{2.42}$$

where, to obtain the attitude, we rotate the inertial axes $\mathscr{I}$ around its z_I axis with an angle ψ, reaching a first auxiliar reference frame, S_1. The same is done with this reference frame, rotating around its axis x_{S_1} with an angle ϕ and, finally rotating the resulting S_2 around its y_{S_2} axis with an angle θ to reach body axes, $\mathscr{B}$.

The director cosine matrices associated to each of these three basic rotations are:

$$C_I^{S_1} = \begin{bmatrix} \cos\psi & \sin\psi & 0 \\ -\sin\psi & \cos\psi & 0 \\ 0 & 0 & 1 \end{bmatrix}, \quad C_{S_1}^{S_2} = \begin{bmatrix} 1 & 0 & 0 \\ 0 & \cos\phi & \sin\phi \\ 0 & -\sin\phi & \cos\phi \end{bmatrix}, \quad C_{S_2}^{B} = \begin{bmatrix} \cos\theta & 0 & -\sin\theta \\ 0 & 1 & 0 \\ \sin\theta & 0 & \cos\theta \end{bmatrix}. \tag{2.43}$$

Therefore, using the composition property of DCMs, we can obtain the DCM associated to our proposed set of Euler angles, through the following matrix product:

$$C_I^B = C_{S_2}^B C_{S_1}^{S_2} C_I^{S_1}, \tag{2.44}$$

$$C_I^B = \begin{bmatrix} \cos\theta\cos\psi - \sin\theta\sin\psi\sin\theta & \cos\theta\sin\psi + \sin\theta\sin\phi\cos\psi & -\sin\theta\cos\phi \\ -\cos\phi\sin\psi & \cos\psi\cos\phi & \sin\phi \\ \sin\theta\cos\psi + \sin\phi\cos\theta\sin\psi & \sin\theta\sin\psi - \sin\phi\cos\theta\cos\psi & \cos\theta\cos\phi \end{bmatrix}. \tag{2.45}$$

In addition, it is possible to relate these Euler angles to the previously defined E-sail's orientation angles α_n and δ_n. So, taking into account that:

$$\mathscr{I} \xrightarrow[y_I]{\alpha_n} \mathscr{A} \xrightarrow[z_A]{\delta_n} \mathscr{B}, \tag{2.46}$$

the following relationships are deduced:

$$\begin{aligned} \cos\alpha_n &= \cos\phi\cos\theta, \\ \sin\alpha_n\sin\delta_n &= \sin\phi, \\ \sin\alpha_n\cos\delta_n &= -\cos\phi\sin\theta. \end{aligned} \tag{2.47}$$

2.2.2 Attitude kinematics and dynamics

Once we have defined and exposed all basic hypothesis, reference frames, the different selected models for E-sail deformed shape and dynamics and, recently, the attitude representation; we have set all conditions needed to set the differential equations that govern the spacecraft's rotational motion. As it will be seen, this movement is described by a system of three attitude kinematic equations and three dynamic equations, six in total, that allow to compute the six corresponding state variables (Euler angles and rotation velocity components).

Attitude kinematic equations

Firstly, the attitude kinematics is represented using Euler angles, with the previously defined sequence. To do so, it is known that the body reference frame's angular velocity (the same as the spacecraft's) with respect to the inertial reference frame, and expressed in body axes, is equal to the sum of the angular velocities of the three basic rotations defining the Euler angles' sequence:

$$\boldsymbol{\Omega}_{B/I}^B = \boldsymbol{\Omega}_{B/S_2}^B + \boldsymbol{\Omega}_{S_2/S_1}^B + \boldsymbol{\Omega}_{S_1/I}^B. \tag{2.48}$$

All these velocities, expressed in their respective reference frames, are defined as:

$$\boldsymbol{\Omega}_{B/I}^B = \begin{Bmatrix} \Omega_x \\ \Omega_y \\ \Omega_z \end{Bmatrix}, \quad \boldsymbol{\Omega}_{B/S_2}^B = \begin{Bmatrix} 0 \\ \dot{\theta} \\ 0 \end{Bmatrix}, \quad \boldsymbol{\Omega}_{S_2/S_1}^{S_2} = \begin{Bmatrix} \dot{\phi} \\ 0 \\ 0 \end{Bmatrix}, \quad \boldsymbol{\Omega}_{S_1/I}^{S_1} = \begin{Bmatrix} 0 \\ 0 \\ \dot{\psi} \end{Bmatrix}. \tag{2.49}$$

However, we need all of them to be expressed in the same reference frame, actually, in body axes. This is easily done using the corresponding DCM transformations, as follows:

$$\mathbf{\Omega}^{B}_{B/I} = \mathbf{\Omega}^{B}_{B/S_2} + C^{B}_{S_2}\mathbf{\Omega}^{S_2}_{S_2/S_1} + C^{B}_{S_2}C^{S_2}_{S_1}\mathbf{\Omega}^{S_1}_{S_1/I}. \tag{2.50}$$

Finally, developing Equation (2.50) and inverting matrices, we reach to the following matrix expression that define the attitude kinematic equations for the selected Euler angles:

$$\begin{Bmatrix} \dot{\phi} \\ \dot{\theta} \\ \dot{\psi} \end{Bmatrix} = \begin{bmatrix} \cos\theta & 0 & \sin\theta \\ \tan\phi\sin\theta & 1 & -\tan\phi\cos\theta \\ -\sin\theta\sec\phi & 0 & \cos\theta\sec\phi \end{bmatrix} \begin{Bmatrix} \Omega_x \\ \Omega_y \\ \Omega_z \end{Bmatrix}. \tag{2.51}$$

Attitude dynamic equations

The attitude dynamic in a rigid solid is described from Euler equations, that relate the time-evolution of the angular velocity and the action of the external torque applied to the solid:

$$\mathbf{I}\dot{\mathbf{\Omega}} + \mathbf{\Omega} \times (\mathbf{I}\mathbf{\Omega}) = \mathbf{T}. \tag{2.52}$$

The general expression in Equation (2.52) is particularized and simplified to the hypothesis formulated in Section 2.1 for E-sail case (axial symmetry for inertia matrix and previously described torque components), obtaining the differential equations for attitude dynamics:

$$\begin{aligned} \dot{\Omega}_x &= \frac{I_t - I_z}{I_t}\Omega_y\Omega_z + \frac{\mathscr{E}}{I_t}, \\ \dot{\Omega}_y &= \frac{I_z - I_t}{I_t}\Omega_x\Omega_z + \frac{\mathscr{F}}{I_t}, \\ \dot{\Omega}_z &= \frac{\mathscr{G}}{I_z}. \end{aligned} \tag{2.53}$$

2.3 Non-dimensional variables and movement equations

This final section aims to summarize the movement equations that are going to be used from now on to study E-sail's attitude change maneuvers, but also to introduce the non-dimensional variables to be used:

$$\mathbf{X} = \begin{Bmatrix} \phi \\ \theta \\ \psi \\ \omega_x \\ \omega_y \\ \omega_z \end{Bmatrix} = \begin{Bmatrix} \phi \\ \theta \\ \psi \\ \Omega_x/\omega \\ \Omega_y/\omega \\ \Omega_z/\omega \end{Bmatrix}, \qquad \mathbf{\Gamma} = \begin{Bmatrix} \Gamma_1 \\ \Gamma_2 \\ \dots \\ \Gamma_k \\ \dots \\ \Gamma_N \end{Bmatrix} = \frac{1}{\sigma}\begin{Bmatrix} \sigma_1 \\ \sigma_2 \\ \dots \\ \sigma_k \\ \dots \\ \sigma_N \end{Bmatrix}, \qquad t^* = \omega t, \tag{2.54}$$

where $\mathbf{X}$ is the vector of state variables, $\mathbf{\Gamma}$ is the vector of control variables (which depend on the voltage modulation) and t^* is the non-dimensional time. The reason to use these non-dimensional variables is to reduce possible numerical errors due to the spread of very high values.

$$
\begin{aligned}
f_1 &\equiv \frac{\mathrm{d}\phi}{\mathrm{d}t^*} = \omega_x \cos\theta + \omega_z \sin\theta, \\
f_2 &\equiv \frac{\mathrm{d}\theta}{\mathrm{d}t^*} = \omega_y - (\omega_z \cos\theta - \omega_x \sin\theta), \\
f_3 &\equiv \frac{\mathrm{d}\psi}{\mathrm{d}t^*} = (\omega_z \cos\theta - \omega_x \sin\theta) \sec\phi, \\
f_4 &\equiv \frac{\mathrm{d}\omega_x}{\mathrm{d}t^*} = \frac{I_t - I_z}{I_t}\omega_y \omega_z + \frac{\mathscr{E}}{I_t \omega^2}, \\
f_5 &\equiv \frac{\mathrm{d}\omega_y}{\mathrm{d}t^*} = \frac{I_z - I_t}{I_t}\omega_x \omega_z + \frac{\mathscr{F}}{I_t \omega^2}, \\
f_6 &\equiv \frac{\mathrm{d}\omega_z}{\mathrm{d}t^*} = \frac{\mathscr{G}}{I_t \omega^2}.
\end{aligned}
\tag{2.55}
$$

As a result, the movement equations, joined up and expressed in terms of non-dimensional variables, are shown in Equation (2.55). Here we can directly identify all state variables, but it is important to remark that the torque components appearing depend both on state and control variables.

3 Control law design

The aim of this chapter is to present the attitude control problem that wants to be solved and propose an appropriate control law. Then, Section 3.1 describes, for an E-sail, the attitude change maneuver that will be studied and, afterwards, Sections 3.2-3.4 expose all the necessary expressions and developments to design a controller suitable for the desired maneuver, which will be based in LQR method. Finally, a LQG-based controller is designed according to Section 3.5, in order to manage noise in measurements and disturbances.

3.1 Problem statement

Given an electric solar sail described by assumptions and dynamic model presented in Chapter 2, we will consider that it is initially in a Sun-facing configuration (i.e., pitch angle $\alpha_{n_0} = 0$) shown in Figure 3.1, and rotating around its symmetry axis z_B with an angular velocity ω. This yields to the following initial conditions, expressed by the non-dimensional state variable vector:

$$\mathbf{X_0} = \mathbf{X}(t^* = 0) = \left\{ \begin{array}{c} \phi_0 \\ \theta_0 \\ \psi_0 \\ \omega_{x_0} \\ \omega_{y_0} \\ \omega_{z_0} \end{array} \right\} = \left\{ \begin{array}{c} 0 \\ 0 \\ 0 \\ 0 \\ 0 \\ 1 \end{array} \right\}. \tag{3.1}$$

Indeed, this initial attitude corresponds to body axes coincident with inertial reference frame, defined in Section 2.1.1. Another initial condition to be fixed is the E-sail's distance with respect to the Sun, as Coulomb forces due to solar wind acting on the tethers actually decay with $1/r$. Therefore, in order to use expression 2.17, that distance is set to 1 AU for our analysis.

Starting from this initial orientation, we want the E-sail to perform a pitch change maneuver from $\alpha_{n_0} = 0$ to a certain desired value of pitch angle α_{n_f}, that will lead to a final attitude represented in Figure 2.2. This maneuver can be performed throughout different strategies; for example, Bassetto et al., in [12], propose an active control law; whereas Pérez et al., in [2], use LQR control instead.

The design methodology used in this project is fundamentally based on these two references. Thus, according to [2], the maneuver is divided into two well-differentiated phases where LQR method is applied: firstly, a tracking phase until maneuver time t_m^* where the E-sail is controlled to follow a certain desired evolution of the pitch angle along time ($\tilde{\alpha}_n(t^*)$) and, afterwards, a regulation phase from t_m^* to the end of operation or simulation t_f^* aimed to stabilize the spacecraft around the final desired attitude.

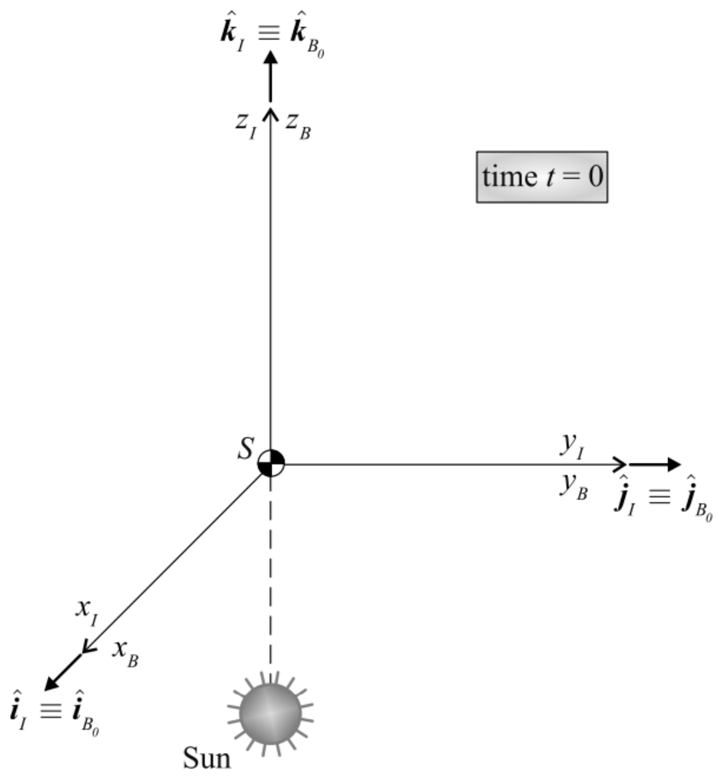

Figure 3.1 Initial attitude situation [12].

From reference [12] we take the reference evolution of pitch angle for tracking phase, which assumes an E-sail rotation around y_B axis with value α_n (which is expressed by auxiliary reference frame A defined in Section 2.1.1). This desired evolution (and its derivatives with respect to time) is expressed in Equations (3.2-3.4) and corresponds to a slew maneuver that allows to rotate the spacecraft from Sun-facing configuration to α_{n_f} in a time t_m^*.

$$\tilde{\alpha}_n(t^*) = \frac{6\alpha_{n_f}}{2(t_m^*)^2}\left[(t^*)^2 - \frac{2}{3}\frac{(t^*)^3}{t_m^*}\right](h(t^*) - h(t^* - t_m^*)) + \alpha_{nf} h(t^* - t_m^*), \tag{3.2}$$

$$\dot{\tilde{\alpha}}_n = \frac{\mathrm{d}\tilde{\alpha}_n}{\mathrm{d}t^*}(t^*) = \frac{6\alpha_{n_f}}{(t_m^*)^2}\left[t^* - \frac{(t^*)^2}{t_m^*}\right](h(t^*) - h(t^* - t_m^*)), \tag{3.3}$$

$$\ddot{\tilde{\alpha}}_n = \frac{\mathrm{d}^2\tilde{\alpha}_n}{\mathrm{d}t^{*2}}(t^*) = \frac{6\alpha_{n_f}}{(t_m^*)^2}\left[1 - \frac{2t^*}{t_m^*}\right](h(t^*) - h(t^* - t_m^*)), \tag{3.4}$$

where $h(t^*)$ is the Heaviside step function, used to maintain the pitch constant at final value after the slew maneuver ends at t_m^*.

However, as stated in 1.4, our dynamic model is extended to non-symmetrical configuration, where each tether is allowed to have a different shape coefficient b_{l_k} and, thus, a different deformed shape depending on the orientation from Sun and the voltage modulation applied to each of them independently.

Additionally, we will consider that the E-sail's state cannot be directly measured, but estimated from gyroscopes measurements. These sensors only provide a measurement for the angular velocities, from which the full state composed by Euler angles and angular velocities has to be estimated. Nevertheless, in reality, the sensors show uncertainty and the dynamic system itself may suffer disturbances, that introduce noise.

This problem will be solved in Section 3.5, introducing a Linear Quadratic Estimator (LQE), or Kalman filter, which is able to estimate the E-sail's state from gyroscopes measurements and filter the noise sources mentioned. This estimator is used together with LQR controller, jointly constituting a Linear Quadratic Gaussian controller (LQG).

3.2 Linearization

As stated in Section 3.1, the objective is to design a control law making use of LQR method [18]. For this purpose, it is fundamental to linearize the system of differential equations expressed in Equation (2.55) that govern the E-sail's rotational movement. Specifically, this linearization process is performed for each of the two phases defined in Section 3.1: a first tracking phase where linearization is done around a reference trajectory that allows to maneuver from initial to final desired attitude and, finally, a regulation phase aimed to maintain the attitude close to the final attitude, with state variables reaching steady state.

3.2.1 Reference values

Reference values in regulation phase

In the case of regulation, reference values for state variables are obtained by fixing some of the variables according to desired final state, being all of them constant in steady state, except from Euler angle ψ, as the spacecraft would continue rotating around its spin axis at constant velocity. In this way, we first fix the reference pitch angle to the desired final value $\alpha_n^{ref} = \alpha_{n_f}$, together with two more variables that are also imposed: $\phi_{ref} = 0$ and $\omega_{z_{ref}}$=1, assuming a dynamic equilibrium where the spacecraft continues spinning around z_B axis in steady state.

Using these conditions and, just applying Equation (2.47), reference clock angle would be $\delta_n^{ref} = \pi$ rad and, also, $\theta_{ref} = \alpha_n^{ref}$. After that, the three missing state variables are obtained from kinematic differential equations (f_1, f_2 and f_3 in Equation 2.55) with time-derivatives set to zero: $\omega_{y_{ref}} = 0$, $\omega_{x_{ref}} = -\tan\theta_{ref}$ and $\dot{\psi}_{ref} = \omega/\cos\theta_{ref}$, from which $\psi_{ref} = t^*/\cos\theta_{ref}$. As a result, reference state variables for regulation phase are summarized in Equation (3.5).

$$\mathbf{X}_{ref} = \left\{ \begin{array}{c} \phi_{ref} \\ \theta_{ref} \\ \psi_{ref} \\ \omega_{x_{ref}} \\ \omega_{y_{ref}} \\ \omega_{z_{ref}} \end{array} \right\} = \left\{ \begin{array}{c} 0 \\ \alpha_{n_f} \\ t^*/\cos\theta_{ref} \\ -\tan\theta_{ref} \\ 0 \\ 1 \end{array} \right\}. \tag{3.5}$$

Furthermore, reference values for control variables Γ_k^{ref} are obtained minimizing function $\Phi(\mathbf{\Gamma})$ in Equation 3.6:

$$\min\ \Phi(\mathbf{\Gamma}) = \Gamma_1^2 + \Gamma_2^2 + \Gamma_3^2 + ... + \Gamma_N^2, \tag{3.6}$$

subject to dynamic Euler equations (f_4, f_5 and f_6 in Equation 2.55), particularized using reference state variables and expressed in steady state:

$$
\begin{aligned}
G_1(\mathbf{\Gamma}_{ref}) &\equiv \frac{I_t - I_z}{I_t}\omega_{y_{ref}}\omega_{z_{ref}} + \frac{\mathscr{E}(\mathbf{\Gamma}_{ref})}{I_t\omega^2} = 0,\\
G_2(\mathbf{\Gamma}_{ref}) &\equiv \frac{I_z - I_t}{I_t}\omega_{x_{ref}}\omega_{z_{ref}} + \frac{\mathscr{F}(\mathbf{\Gamma}_{ref})}{I_t\omega^2} = 0,\\
G_3(\mathbf{\Gamma}_{ref}) &\equiv \frac{\mathscr{G}(\mathbf{\Gamma}_{ref})}{I_z\omega^2} = 0.
\end{aligned} \tag{3.7}
$$

To perform the minimization, Lagrange's multipliers theorem is applied, introducing Lagrange's multipliers $[\kappa_1, \kappa_2, \kappa_3]$ and the N equations in (3.8):

$$
\frac{\partial\Phi(\mathbf{\Gamma}_{ref})}{\partial\Gamma_k^{ref}} - \kappa_1\frac{\partial G_1(\mathbf{\Gamma}_{ref})}{\partial\Gamma_k^{ref}} - \kappa_2\frac{\partial G_2(\mathbf{\Gamma}_{ref})}{\partial\Gamma_k^{ref}} - \kappa_3\frac{\partial G_3(\mathbf{\Gamma}_{ref})}{\partial\Gamma_k^{ref}} = 0 \quad \text{with} \quad k = 1,...,N \tag{3.8}
$$

So, solving $N+3$ equations (3.7)-(3.8) we can compute the N reference control variables Γ_k^{ref} plus the 3 Lagrange's multipliers. However, unlike it would happen with simplified deformed shape model, where the system of equations is completely linear [2], in this project there are non-linear dependencies inside the torque components.

In more detail and, according to Equations (2.39)-(2.41), torque components depend on the control variables Γ_k apparently linearly; however, we are assuming a shape coefficient model depending also on $\sigma_k = \sigma\Gamma_k$, breaking linearity. Therefore, a special numerical process has to be defined to solve system of equations (3.7)-(3.8) used for minimization:

1. Compute shape coefficients b_{l_k} using α_n^{ref} and δ_n^{ref}, expressing them as function of control variables Γ_k^{ref}, which are unknowns.
2. Calculate torque components as functions of Γ_k^{ref}, using equations (2.39)-(2.41).
3. Compute the first derivatives of torque components with respect to σ_k^{ref}, according to Appendix B.1, as functions of Γ_k^{ref}
4. Calculate the first derivatives of Φ, G_1, G_2 and G_3 with respect to Γ_k^{ref}, as functions of Γ_k^{ref}, using Equation 3.9:

$$
\begin{aligned}
\frac{\partial\Phi(\mathbf{\Gamma})}{\partial\Gamma_k^{ref}} &= 2\Gamma_k^{ref},\\
\frac{\partial G_1(\mathbf{\Gamma}_{ref})}{\partial\Gamma_k^{ref}} &= \frac{\sigma}{I_t\omega^2}\frac{\partial\mathscr{E}_k(\mathbf{\Gamma}_{ref})}{\partial\sigma_k},\\
\frac{\partial G_2(\mathbf{\Gamma}_{ref})}{\partial\Gamma_k^{ref}} &= \frac{\sigma}{I_t\omega^2}\frac{\partial\mathscr{F}_k(\mathbf{\Gamma}_{ref})}{\partial\sigma_k},\\
\frac{\partial G_3(\mathbf{\Gamma}_{ref})}{\partial\Gamma_k^{ref}} &= \frac{\sigma}{I_z\omega^2}\frac{\partial\mathscr{G}_k(\mathbf{\Gamma}_{ref})}{\partial\sigma_k}.
\end{aligned} \tag{3.9}
$$

5. Solve numerically the system of equations (3.7)-(3.8) with Γ_k^{ref} and Lagrange's multipliers as unknowns.

Reference values in tracking phase

Regarding the tracking phase, the selected reference movement corresponds to the slew maneuver defined in Section 3.1, which allows to change the pitch angle from zero (Sun-facing configuration) to the final desired orientation. As a consequence, this phase is a transient regime where many of the reference values for state and control variables will depend on time.

Specifically, the reference pitch angle is selected to have the same evolution as the slew maneuver described in Equation (3.2), i.e. $\alpha_n^{ref}(t^*) = \tilde{\alpha}_n(t^*)$. Besides, the same reference values as in regulation phase are assigned to variables ϕ and ω_z, this is: $\phi_{ref} = 0$ and $\omega_{z_{ref}} = 1$.

On the one hand, after imposing these reference values, a similar deduction is performed to obtain the rest of reference state variables. Thus, $\delta_n^{ref} = \pi$ rad and $\theta_{ref}(t^*) = \alpha_n^{ref}(t^*)$ are computed from Equation (2.47), where θ_{ref} now depends on time as $\alpha_{n_{ref}}$ does. Due to this fact, the remaining reference state variables will vary also with time, as they are deduced from kinematic differential equations in (2.55). All these values are gathered in $\mathbf{X}_{ref}(t^*)$:

$$\mathbf{X}_{ref}(t^*) = \left\{ \begin{array}{c} \phi_{ref}(t^*) \\ \theta_{ref}(t^*) \\ \psi_{ref}(t^*) \\ \omega_{x_{ref}}(t^*) \\ \omega_{y_{ref}}(t^*) \\ \omega_{z_{ref}}(t^*) \end{array} \right\} = \left\{ \begin{array}{c} 0 \\ \tilde{\alpha}_n(t^*) \\ \int_0^{t^*} 1/\cos\theta_{ref}(t')\,\mathrm{d}t' \\ -\tan\theta_{ref}(t^*) \\ \dot{\tilde{\alpha}}_n(t^*) \\ 1 \end{array} \right\}. \tag{3.10}$$

On the other hand, reference control variables ($\mathbf{\Gamma}_{ref}(t^*)$) are also computed by minimizing the function expressed in Equation (3.11), which is solved throughout the algebraic system of equations composed by dynamic differential equations (3.12) and applying Lagrange's multipliers theorem (3.13):

$$\min\ \Phi(\mathbf{\Gamma},t^*) = \Gamma_1^2(t^*) + \Gamma_2^2(t^*) + \Gamma_3^2(t^*) + \ldots + \Gamma_N^2(t^*), \tag{3.11}$$

$$\begin{aligned} G_1(\mathbf{\Gamma}_{ref},t^*) &\equiv \frac{I_t - I_z}{I_t}\omega_{y_{ref}}(t^*)\omega_{z_{ref}}(t^*) + \frac{\mathscr{E}(\mathbf{\Gamma}_{ref},t^*)}{I_t\omega^2} - \dot{\omega}_{x_{ref}}(t^*) = 0, \\ G_2(\mathbf{\Gamma}_{ref},t^*) &\equiv \frac{I_z - I_t}{I_t}\omega_{x_{ref}}(t^*)\omega_{z_{ref}}(t^*) + \frac{\mathscr{F}(\mathbf{\Gamma}_{ref},t^*)}{I_t\omega^2} - \dot{\omega}_{y_{ref}}(t^*) = 0, \\ G_3(\mathbf{\Gamma}_{ref},t^*) &\equiv \frac{\mathscr{G}(\mathbf{\Gamma}_{ref},t^*)}{I_z\omega^2} - \dot{\omega}_{z_{ref}}(t^*) = 0, \end{aligned} \tag{3.12}$$

$$\frac{\partial\Phi(\mathbf{\Gamma}_{ref},t^*)}{\partial\Gamma_k^{ref}} - \kappa_1(t^*)\frac{\partial G_1(\mathbf{\Gamma}_{ref},t^*)}{\partial\Gamma_k^{ref}} - \kappa_2(t^*)\frac{\partial G_2(\mathbf{\Gamma}_{ref},t^*)}{\partial\Gamma_k^{ref}} - \kappa_3(t^*)\frac{\partial G_3(\mathbf{\Gamma}_{ref},t^*)}{\partial\Gamma_k^{ref}} \quad \text{with} \quad k = 1,\ldots,N. \tag{3.13}$$

In particular, this system of equations has to be solved using the reference values for the state variables at each time instant during the tracking maneuver. Besides, the first derivatives of non-dimensional angular velocities with time are appearing now in dynamic equations (as compared to regulation, where they are constant and, hence, their derivatives are null), so they are calculated from derivation of (3.10):

$$\begin{aligned} \dot{\omega}_{x_{ref}}(t^*) &= -\sec^2\tilde{\alpha}_n(t^*)\dot{\tilde{\alpha}}_n(t^*), \\ \dot{\omega}_{y_{ref}}(t^*) &= \ddot{\tilde{\alpha}}_n(t^*), \\ \dot{\omega}_{z_{ref}}(t^*) &= 0. \end{aligned} \tag{3.14}$$

3.2.2 Linearization process

Once the reference values for state and control variables have been determined, to perform the linearization of movement equations **f** (2.55) we apply Taylor's theorem to approximate the non-linear functions by Taylor's polynomials of first order around the mentioned reference values. In general, these linearized equations are expressed in terms of matrices A and B, containing the first derivatives of each movement equation with respect each variable, multiplied by their corresponding incremental variables.

Linearized equations in regulation phase

In regulation phase, the linearized differential movement equations are expressed by Equation (3.15):

$$\delta\dot{\mathbf{X}}(t^*) = A\delta\mathbf{X}(t^*) + B\delta\mathbf{\Gamma}(t^*), \tag{3.15}$$

where A is the 6x6 matrix consisting of the first derivatives of movement equations with respect to non-dimensional state variables (Euler angles and angular velocities):

$$A = \frac{\partial\mathbf{f}(\mathbf{X}_{ref},\mathbf{\Gamma}_{ref})}{\partial\mathbf{X}}, \tag{3.16}$$

B is the 6xN matrix consisting of the first derivatives of movement equations with respect to non-dimensional control variables:

$$B = \frac{\partial\mathbf{f}(\mathbf{X}_{ref},\mathbf{\Gamma}_{ref})}{\partial\mathbf{\Gamma}}, \tag{3.17}$$

and, finally, $\delta\mathbf{X}$ and $\delta\mathbf{\Gamma}$ represent the incremental variables for both state and control variables, with respect to their reference values:

$$\delta\mathbf{X} = \mathbf{X} - \mathbf{X}_{ref}, \qquad \delta\mathbf{\Gamma} = \mathbf{\Gamma} - \mathbf{\Gamma}_{ref}. \tag{3.18}$$

All derivatives appearing in Equations (3.16)-(3.17) are defined in Appendix C for regulation phase. At this point, it is important to remark that ψ_{ref} depends on time but, as the derivatives corresponding to this Euler angle are all zero, it is possible to affirm that matrices A and B are compose of constant values. This fact will allow to apply later on Section 3.3.1 the LQR method with infinite horizon for regulation case.

Linearized equations in tracking phase

The linearized spacecraft dynamics around the slew maneuver in tracking phase is characterized by Equation (3.19):

$$\delta\dot{\mathbf{X}}(t^*) = A(t^*)\delta\mathbf{X}(t^*) + B(t^*)\delta\mathbf{\Gamma}(t^*), \tag{3.19}$$

where now A and B linearization matrices are dependent on time, as they are again computed from derivation of differential movement equations (2.55) and particularized for reference values of state and control variables, which vary with time for tracking phase. Their expressions are described in Equations (3.20)-(3.21):

$$A(t^*) = \frac{\partial\mathbf{f}(\mathbf{X}_{ref}(t^*),\mathbf{\Gamma}_{ref}(t^*))}{\partial\mathbf{X}}, \tag{3.20}$$

$$B(t^*) = \frac{\partial\mathbf{f}(\mathbf{X}_{ref}(t^*),\mathbf{\Gamma}_{ref}(t^*))}{\partial\mathbf{\Gamma}}, \tag{3.21}$$

where all the derivatives to compute A and B are again explained in Appendix C.

Finally, the expressions for incremental state and control variables now contain the time evolution of references:

$$\delta\mathbf{X}(t^*) = \mathbf{X}(t^*) - \mathbf{X}_{ref}(t^*), \qquad \delta\mathbf{\Gamma}(t^*) = \mathbf{\Gamma}(t^*) - \mathbf{\Gamma}_{ref}(t^*). \tag{3.22}$$

3.3 LQR control

Linear Quadratic Regulator (LQR) is an active control method that pretends to stabilize a dynamic system around a certain desired reference trajectory and minimizing a certain quadratic cost function. For this purpose, LQR provides the methodology to find the values of the gain matrix K that is able to minimize deviations between actual problem variables and their reference values (i.e. incremental variables $\delta\mathbf{X}$ and $\delta\mathbf{\Gamma}$), hence proposing a linear feedback control law for closed-loop control.

Subsequent sections look into LQR control in more detail, providing specific conditions for determining the control law and the system controllability, in each of the two phases considered in this project. Thus, infinite horizon LQR will be applied to regulation phase, where linearization matrices A and B do not depend on time and the objective is to stabilize the system around the final attitude; whereas finite horizon LQR is used for tracking phase, where there exists a dependence on time, as the objective is to follow a certain reference trajectory.

3.3.1 Infinite horizon LQR (regulation phase)

Infinite horizon LQR method applies to linear dynamic systems, whose linearization matrices are independent on time, as it is the case of our E-sail model in regulation phase, expressed in linearized differential equations 3.15. Therefore, the objective is, given those equations, to find a feedback control law that minimizes the following potential:

$$\min J = \int_0^\infty \left(\delta\mathbf{X}^T(t^*) Q \delta\mathbf{X}(t^*) + \delta\mathbf{\Gamma}^T(t^*) R \delta\mathbf{\Gamma}(t^*)\right) \mathrm{d}t^*, \tag{3.23}$$

where Q and R are assumed to be two symmetrical matrices, being Q definite positive and R semidefinite positive. They represent the relative weights assigned to state and control variables, respectively, and their choice would greatly influence the quality of the controller, provoking either a smoother or more aggresive response from the dynamic system and hence, a different demand from control input. In this project, Q and R are determined to be, after a trial and error process:

$$Q = Id_6, \quad R = \frac{10^{10}}{V_w^2} Id_N, \tag{3.24}$$

where Id_n means the identity matrix of order n.

As stated in Section 3.3 introduction, there exists a linear feedback control law that solves the optimization problem in Equation (3.23), subject to the linearized dynamic system equations expressed in Equation (3.15):

$$\delta\mathbf{\Gamma}(t^*) = K\delta\mathbf{X}(t^*). \tag{3.25}$$

The feedback gain, K, is a matrix of constant elements that is computed from Equation (3.26), where P matrix results from solving the Algebraic Riccati Equation (3.27):

$$K = -R^{-1}B^T P, \tag{3.26}$$

$$Q + A^T P + PA - PBR^{-1}B^T P = 0. \tag{3.27}$$

Finally, it is also fundamental to check the controllability condition for our dynamic system before solving LQR problem to ensure that it is resolvable. In our E-sail case, with 6 state variables, the system would be controllable if $C = [B\, AB\, A^2B\, A^3B\, A^4B\, A^5B]$ matrix has full row rank (if the number of tethers is N, then the rank should be N).

3.3.2 Finite horizon LQR (tracking phase)

Finite horizon LQR is applied to tracking phase in order to have a more precise control over the maneuver duration and the resulting attitude evolution, in contrast to regulation phase, when stabilization after reaching the final attitude is the main purpose. In this case, the linearization matrices A and B depend on time, as they describe a transient regime expressed in Equation (3.19).

Again, the objective is to find a feedback control law that minimizes a certain potential; however, the dependence on time changes the objective of control problem and, therefore, its solution strategy. In this case, the potential is computed until a defined time horizon, that is coincident with the desired tracking phase duration T^*:

$$\min J = \delta\mathbf{X}^T(T^*)Q_{end}\delta\mathbf{X}(T^*) + \int_0^{T^*} \left(\delta\mathbf{X}^T(t^*)Q(t^*)\delta\mathbf{X}(t^*) + \delta\mathbf{\Gamma}^T(t^*)R(t^*)\delta\mathbf{\Gamma}(t^*)\right) \mathrm{d}t^*, \tag{3.28}$$

where, appart from the previously introduced matrices Q and R representing the relative weights assigned to state and control variables, respectively, a new matrix Q_{fin} is defined (being also symmetrical and definite positive), determining the relative weight assigned to the final state. In this case, these matrices can vary with time, so we will take advantage of this property to make R increase linearly until reaching the regulation value. As a result, the weight matrices are defined as:

$$Q_{end} = Id_6, \quad Q(t^*) = Id_6, \quad R(t^*) = \frac{10^{10} - 10^4(1 - t^*/T^*)}{V_w^2} Id_N, \tag{3.29}$$

The finite horizon LQR problem posed in Equation (3.28), and subject to the linearized dynamic differential equations (3.19), can be solved using the linear feedback control law in Equation (3.30). Besides, this control problem does not require a controllability hypothesis, as compared to infinite horizon LQR, but problems may arise due to controllability loss at some time instant.

$$\delta\mathbf{\Gamma}(t^*) = K(t^*)\delta\mathbf{X}(t^*). \tag{3.30}$$

The gain matrix K depends on time for tracking and comes from Equation (3.31):

$$K(t^*) = -R^{-1}B^T(t^*)P(t^*), \tag{3.31}$$

where P matrix is now also dependent on time and results from solving the Riccati Differential Equation (3.32). This differential equation needs to be solved backwards on time from $t^* = T^*$ to $t^* = 0$, as the boundary condition is given at the end of the maneuver ($P(t_m^*) = Q_{end}$). This is easily done by applying the variable change $t' = T^* - t^*$.

$$-\dot{P}(t^*) = Q + A^T(t^*)P(t^*) + P(t^*)A(t^*) - P(t^*)B(t^*)R^{-1}B^T(t^*)P(t^*), \quad P(T^*) = Q_{end}. \tag{3.32}$$

3.4 Transition from tracking to regulation phase

At this point, the control strategy for both stages of the attitude change maneuver has been defined. However, if we consider that, at the instant t_m^* when the slew maneuver ends, the tracking finite horizon LQR transfers the control to infinite horizon LQR, there may be a sudden step change in control variables, that may lead to overshooting in the attitude response, as it is studied in [2].

This issue can be solved in two different ways, that are applied combined in this project:

Delayed transition

This idea is based on extending the tracking phase beyond the slew maneuver duration t_m^*, comprising both the slew maneuver and some determined time interval after, when $\alpha_{n_{ref}}$ is permanent regime. Therefore, tracking phase is applied until a selected time T^* greater or equal to t_m^*, when regulation control begins.

As the reference pitch angle after t_m^* is constant, the tracking controller after that instant behaves in a more similar way to the regulation phase, as it was a permanent regime. As a consequence, this helps to stabilize the subsequent regulation phase, because the sudden change of reference variables and control between phases is reduced.

First order filter

Additionally, a first order filter can be introduced just after the transition instant T^* to turn the step change in control variables into a smooth variation. Then, the feedback control gain matrix for regulation is modified using the filter expressed in Equation (3.33):

$$K_{regulation}^{modified}(t^*) = K_{tracking}(T^*)e^{-c(t^*-T^*)} + K_{regulation}\left(1 - e^{-c(t^*-T^*)}\right), \tag{3.33}$$

where $K_{tracking}(T^*)$ is the last gain matrix of tracking phase, which is faded by a rate $e^{-c(t^*-T^*)}$, with $c = 1000$ inversely proportional to the transition duration, while $K_{regulation}$ gains weight at the same rate.

3.5 LQG control

In this section, the E-sail control dynamics is modelled according to the control diagram in Figure 3.2. In contrast to Section 3.3, where the system was only composed by a feedback loop using LQR method, now we consider that the E-sail state ($\mathbf{X}$) cannot be measured directly and there are two sources of noise.

On the one hand, it is known that the E-sail dynamics is defined, in the ideal case, by Equations (2.55). However, now we assume that some disturbances appear in terms of angular accelerations (which may come from neglected gravitational and centrifugal terms, for example). Thus, these disturbances are modelled as a white gaussian noise with mean zero and covariance V: $\mathbf{v} \sim N_n(0,V)$.

On the other hand, the E-sail state has to be deduced from sensors measurements $\mathbf{y}$. In our case, we assume that the E-sail has one optical gyroscope per body axis (three in total) incorporated, which are able to provide the measurement for angular velocities $\boldsymbol{\Omega}$ at each instant, with a certain white gaussian noise with mean zero and covariance W: $\mathbf{w} \sim N_n(0,W)$.

As a result, the system is defined by:

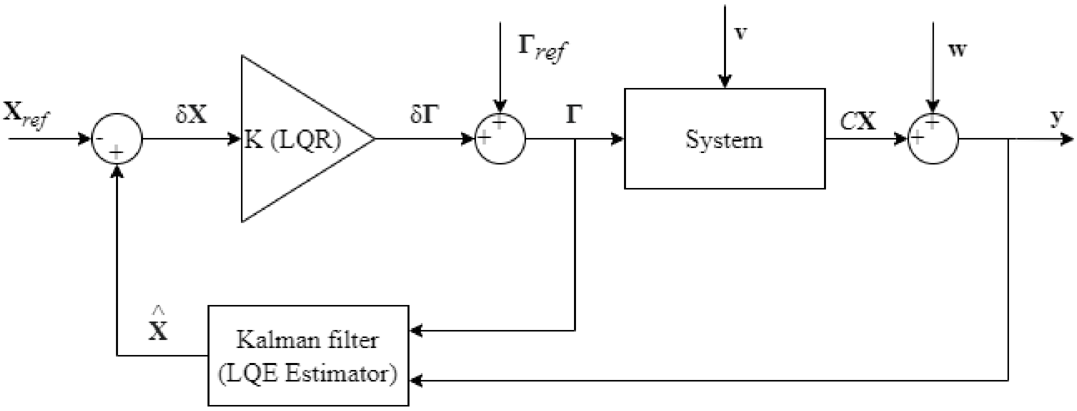

Figure 3.2 Linear Quadratic Gaussian control diagram.

$$\dot{\mathbf{X}}(t^*) = f(\mathbf{X},\boldsymbol{\Gamma},t^*) + \mathbf{v}(t^*), \tag{3.34}$$

$$\mathbf{y}(t^*) = C\mathbf{X}(t^*) + \mathbf{w}(t^*), \tag{3.35}$$

where C matrix establishes the relationship between the measurements and the system state variables:

$$C = \begin{bmatrix} 0 & 0 & 0 & 1 & 0 & 0 \\ 0 & 0 & 0 & 0 & 1 & 0 \\ 0 & 0 & 0 & 0 & 0 & 1 \end{bmatrix}. \tag{3.36}$$

The control problem defined by Equations (3.34)-(3.35) can be solved using Linear Quadratic Gaussian control (LQG), as the system dynamics can be linearized (as done in Section 3.2) and it is driven by additive white Gaussian noise. This type of controller combines a Kalman filter to estimate the state from the measurements and a LQR controller that uses that estimation to determine a feedback law that is able to minimize a certain quadratic cost function [19].

Therefore, considering the linearized dynamics represented in Equations (3.37), where A and B linearization matrices are computed according to Section 3.2, the objective of LQG problem is to minimize the potential J, which is now given in terms of the stochastic expected value ("$E[X]$"), as per Equation (3.38).

$$\delta\dot{\mathbf{X}}(t^*) = A(t^*)\delta\mathbf{X}(t^*) + B(t^*)\delta\boldsymbol{\Gamma}(t^*) + \mathbf{v}(t^*), \tag{3.37}$$

$$\min J = E\left[\delta\mathbf{X}^T(T^*)Q_{end}\delta\mathbf{X}(T^*) + \int_0^{T^*} \left(\delta\mathbf{X}^T(t^*)Q(t^*)\delta\mathbf{X}(t^*) + \delta\boldsymbol{\Gamma}^T(t^*)R(t^*)\delta\boldsymbol{\Gamma}(t^*)\right) \mathrm{d}t^*\right] \tag{3.38}$$

The LQG controller that is able to minimize the cost function J is defined by a LQR controller with feedback gain matrix K, which is computed as explained in Section 3.3, but where the control variables are computed from an estimation of the state, denoted by $\hat{\mathbf{X}}$:

$$\boldsymbol{\Gamma} = K(\hat{\mathbf{X}} - \mathbf{X}_{ref}) + \boldsymbol{\Gamma}_{ref}. \tag{3.39}$$

The estimates of the state are given, at each time instant, by a Kalman filter defined by Equation (3.40):

$$\dot{\hat{\mathbf{X}}}(t^*) = f(\hat{\mathbf{X}},\mathbf{\Gamma},t^*) + K_f(t^*)\left(\mathbf{y}(t^*) - C\hat{\mathbf{X}}(t^*)\right). \tag{3.40}$$

The associated Kalman gain matrix, K_f, is optimal minimizing the propagation error of the stochastic process defined in Equation (3.34), with measurements $\mathbf{y}$. This gain is computed from the following Riccati differential equation that solves a Linear Quadratic Estimation problem (LQE), where $S = E[\mathbf{X}(t^*)\mathbf{X}^T(t^*)]$ is the propagation error matrix (covariance of state variables):

$$\begin{aligned} \dot{S}(t^*) &= A(t^*)S(t^*) + S(t^*)A^T(t^*) - S(t^*)C^T W^{-1} C S(t^*) + V, \\ S(0) &= E[\mathbf{X}(0)\mathbf{X}^T(0)]. \end{aligned} \tag{3.41}$$

Solving this differential equation from $t^* = 0$ to $t^* = T^*$, $S(t^*)$ is obtained, from which Kalman gain is finally computed:

$$K_f(t^*) = S(t^*)C^T W^{-1}. \tag{3.42}$$

To conclude, some particularities are remarked. On the one hand, matrices C, V and W can depend on time, but in this project will be defined as constant values; this fact allows to compute K in regulation phase using the algebraic Riccati equation instead of the differential one, as all the matrices involved must be constant (A is constant in regulation phase) to do so. Indeed, for regulation, the cost potential J is integrated to $T^* \to \infty$ and the term of Q_{end} is neglected. On the other hand, the LQG controller is subject to the separation principle, which allows to design both the Kalman filter and the LQR controller independently.

4 Results

This chapter contains all the results that allow to validate the applicability and study the behaviour of the proposed E-sail model, the LQR control and the LQG control with noise. Firstly, Section 4.1 illustrates the non-symmetrical tethers' deformed shape model. After that, Sections 4.2-4.3 are dedicated to study LQR and LQG controllers, respectively, analyzing the operating range limited by saturation, the theoretical limits of the dynamic model and, also, the response under measurements affected by noise.

4.1 Shape coefficient analysis

One of the main points of innovation in this project is the proposed model for the tethers' deformed shape, allowing each tether to deform asymmetrically depending on the E-sail orientation and the applied voltage. In order to illustrate this idea, two main results are presented hereunder.

On the one hand, Figures 4.1-4.2 represent the dependencies of the shape coefficient with pitch angle (assuming constant nominal $\sigma = 9.2818 \cdot 10^{-13}$ kg/(m s)) and the voltage parameter σ (assuming constant pitch $\alpha_n = 0$), studying the first tether (the one aligned with x_B) with $\delta_n = \pi$ rad.

As explained in Section 2.1, the shape coefficient is defined as the tether's deformed shape slope at the root and it is directly related to the applied forces. Thus, when increasing the pitch angle, the perpendicular component of the solar wind diminishes, directly decreasing the electric forces exerted on the tether; in contrast, these forces are increased with the voltage applied on tethers (related to parameter σ). As a consequence, the shape coefficient decreases with the pitch and linearly increases with σ, as seen in Figures 4.1-4.2.

On the other hand, the actual deformed shape according to our model with non-symmetrical configuration is depicted in Figures 4.3-4.4, where it is compared to the symmetrical model where all tethers would deform identically. Variables α_n and σ_k are taken from successive simulations in Section 4.2, representing a pitch change maneuver to reach 5 and 20 degrees, under LQR control.

Analyzing the resulting deformed shape, we can observe that the symmetrical model provides exactly the same shape, so it can be used as reference for comparison. Thus, the tethers under non-symmetrical model experience the expected behaviour: the tethers subject to higher voltage suffer more deformation and all the tethers reduce their slope when increasing the pitch angle.

To conclude, the symmetrical deformed shape model is defined assuming a Sun-facing configuration, with null pitch angle, so it is logical that both models compared produce similar results at low pitch angles (until 10 degrees approximately), but differ at higher pitch angles, where Sun-facing hypothesis is no longer valid as first order approximation. This difference is specially remarkable at 60 degrees (Figure 4.5), where the tethers at lower voltage show a negative deformation due to the effect of obliquity from Sun.

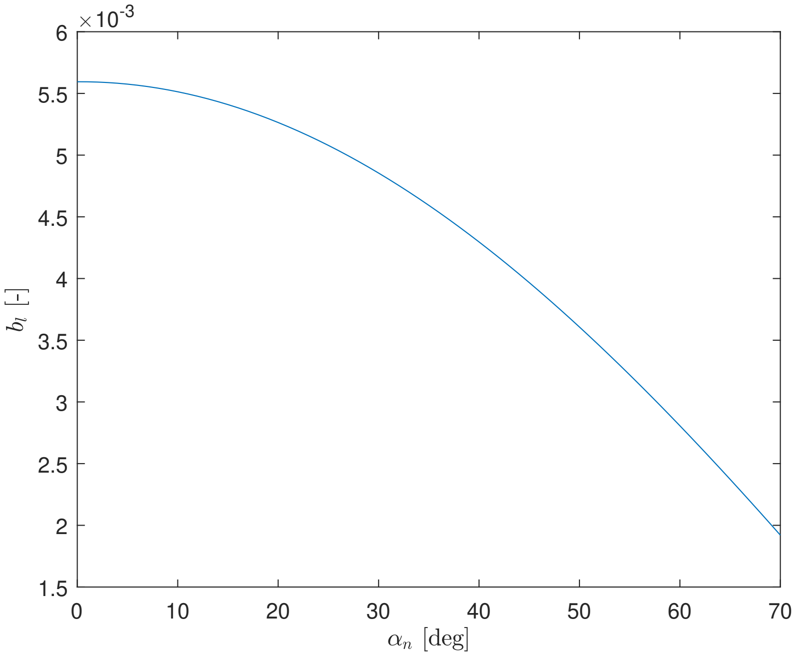

Figure 4.1 Shape coefficient b_{l_k} as function of the pitch angle α_n.

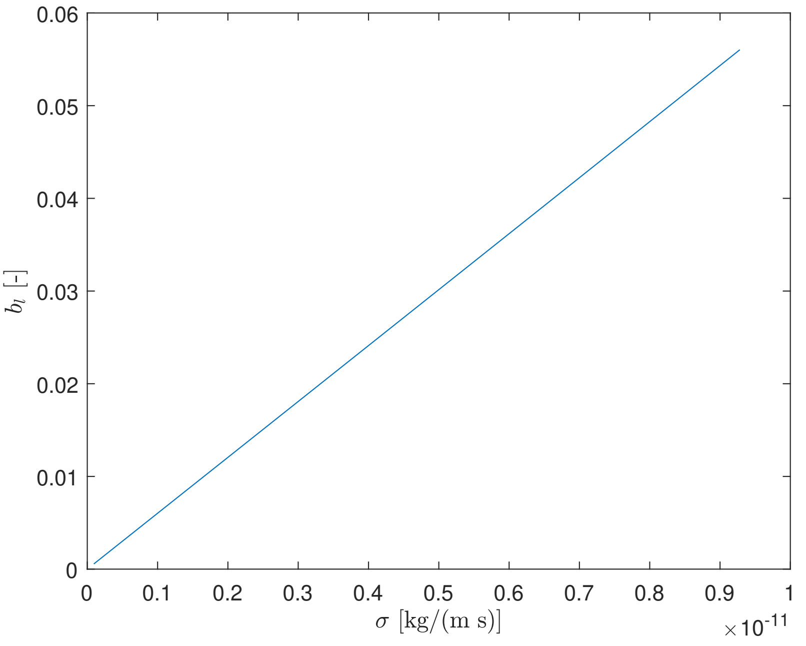

Figure 4.2 Shape coefficient b_{l_k} as function of the parameter σ.

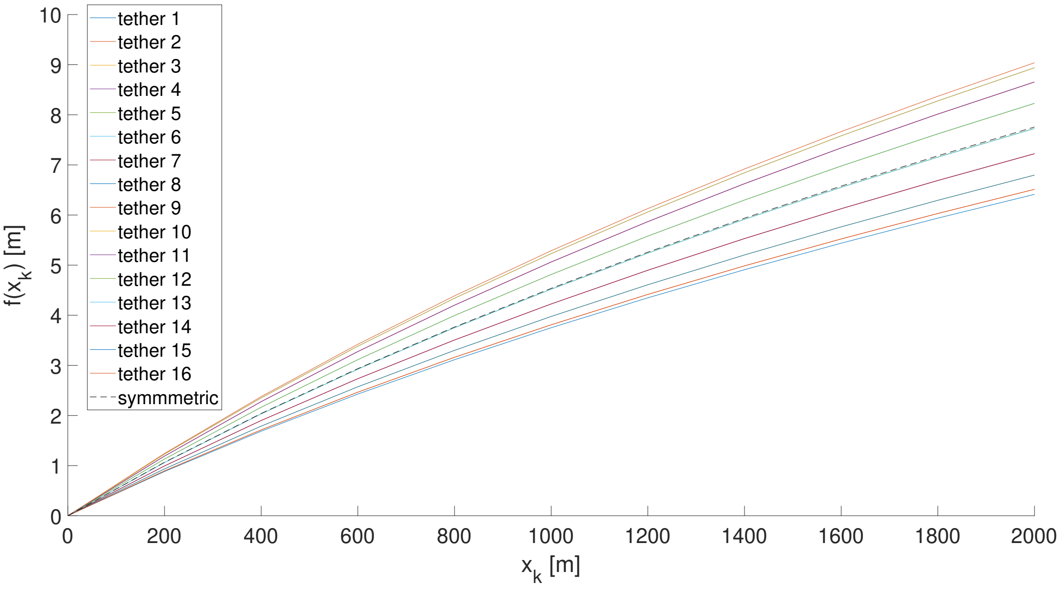

Figure 4.3 Tethers' deformed shape in permanent regime of maneuver until $\alpha_{nf} = 5^\circ$ using LQR control.

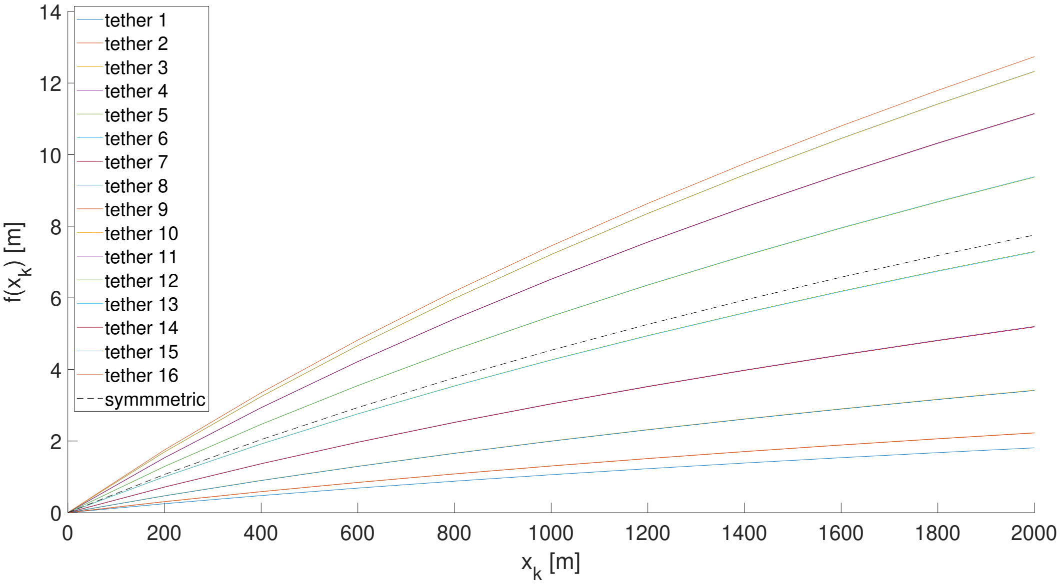

Figure 4.4 Tethers' deformed shape in permanent regime of maneuver until $\alpha_{nf} = 20^\circ$ using LQR control.

4.2 LQR control results

Hereunder, in this section, the LQR controller designed in Section 3.3 is tested directly on our E-sail model with 16 tethers. The main objective is to simulate several scenarios with different desired final pitch angles (α_{nf}) from 5 to 70 degrees, in order to validate the limits of both the tethers' non-symmetrical shape model and the LQR control under these assumptions, as compared to the symmetrical case studied by Pérez et al. [2]

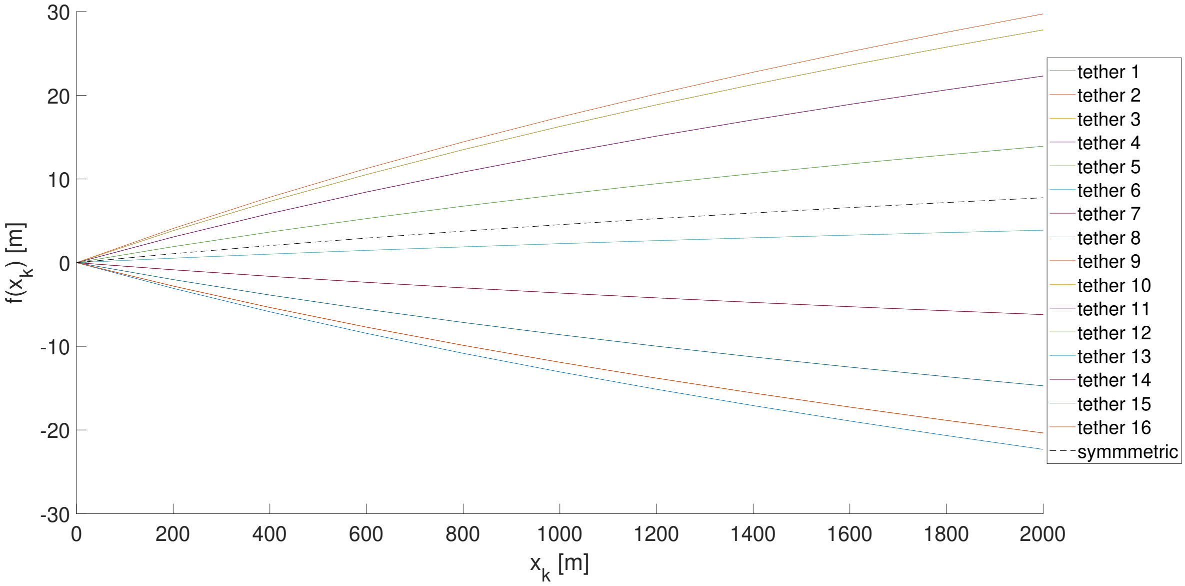

Figure 4.5 Tethers' deformed shape in permanent regime of maneuver until $\alpha_{nf} = 60^\circ$ using LQR control.

4.2.1 Analysis with control saturation

Firstly, the pitch change maneuver is studied at low pitch angles, where LQR controller should behave stable and close to the given reference, with a minimal demand of control voltage (represented by coefficients σ_k). Besides, the control power is assumed to be feasible until the saturation limit $\sigma_{max} = 1.15\sigma = 1.07 \cdot 10^{-12}$ kg/(m s), remarking that σ_k will represent in this chapter the increment of voltage with respect to the nominal σ. Hence, the aim is also to verify which is the maximum pitch angle that can be reached due to this saturation limit.

Consequently, three cases are now studied, taking into account control saturation: maneuver until final pitch $\alpha_{nf} = 5^\circ$, $\alpha_{nf} = 20^\circ$ and $\alpha_{nf} = 30^\circ$. In general, simulations are performed for a time-interval of 8 minutes, being the slew maneuver time $t_m = 2$ min and the transition time from tracking to regulation $T = 4$ min.

Starting with the most remarkable result, the E-sail response on pitch angle, we know from reference [2] that, in a symmetrical model where all tethers have the same deformed shape, the maneuver is limited by saturation at approximately $\alpha_{nf} = 15^\circ$. Regarding our model, where each tether shape is independently determined by the applied voltage and attitude, it is possible to observe that saturation limit is extended to, approximately, $\alpha_{nf} = 28.2^\circ$, as shown in Figures 4.8 and 4.18.

Thus, Figures 4.6-4.7 show a smooth pitch angle response, without overshooting when reaching the desired angle nor appreciable oscillations in permanent regime. Indeed, on the one hand, $\alpha_{nf} = 5^\circ$ response is practically the same as the one obtained in [2], as both models should provide comparable dynamics until a pitch angle of 10 degrees, where they can be approximated as a Sun-facing configuration. On the other, $\alpha_{nf} = 20^\circ$ response is acceptable and validates the extension of this project's E-sail model to a wider range of pitch angles.

However, this operative range finds its limit when simulating a maneuver to $\alpha_{nf} = 30^\circ$, which leads to control power saturation (see Figure 4.9). As a consequence, the maximum pitch angle reached with the technological limit set is $\alpha_{n_{max}} = 28.2°$, demonstrated in Figures 4.8 and 4.18. This improvement directly enhances the E-sail's thrust vector orientation capabilities, as an example.

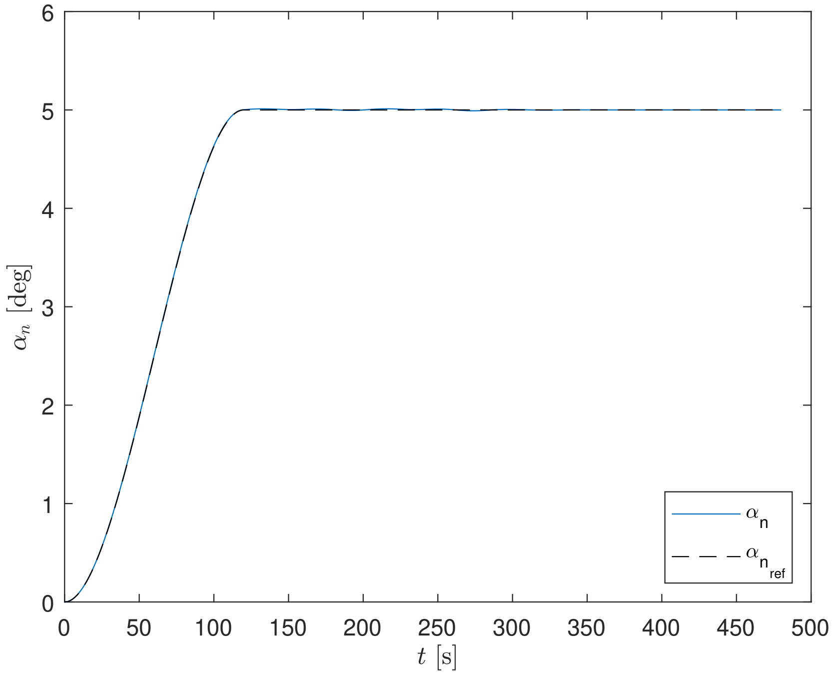

Figure 4.6 Pitch angle α_n evolution using LQR to reach a final pitch $\alpha_{nf} = 5°$.

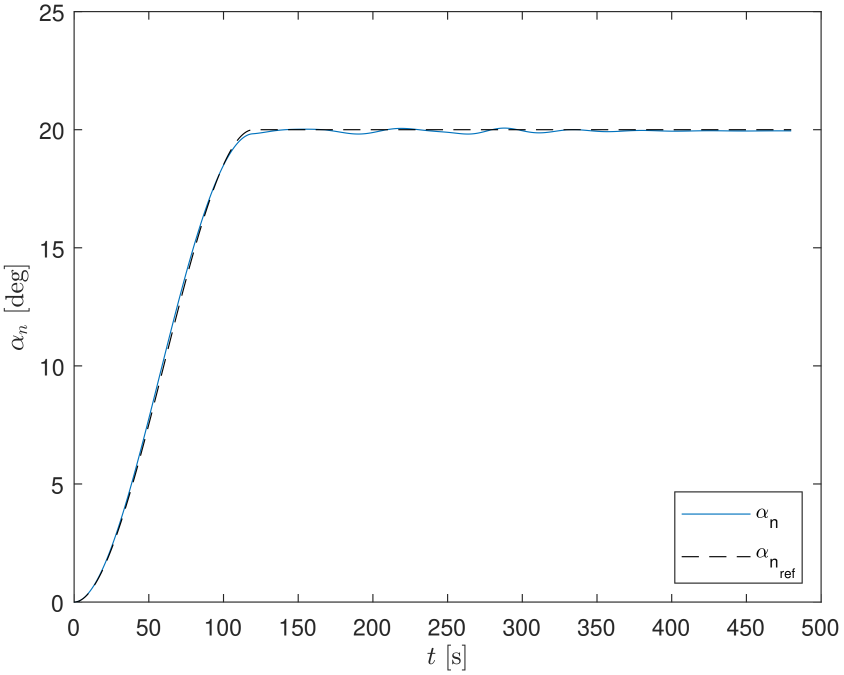

Figure 4.7 Pitch angle α_n evolution using LQR to reach a final pitch $\alpha_{nf} = 20°$.

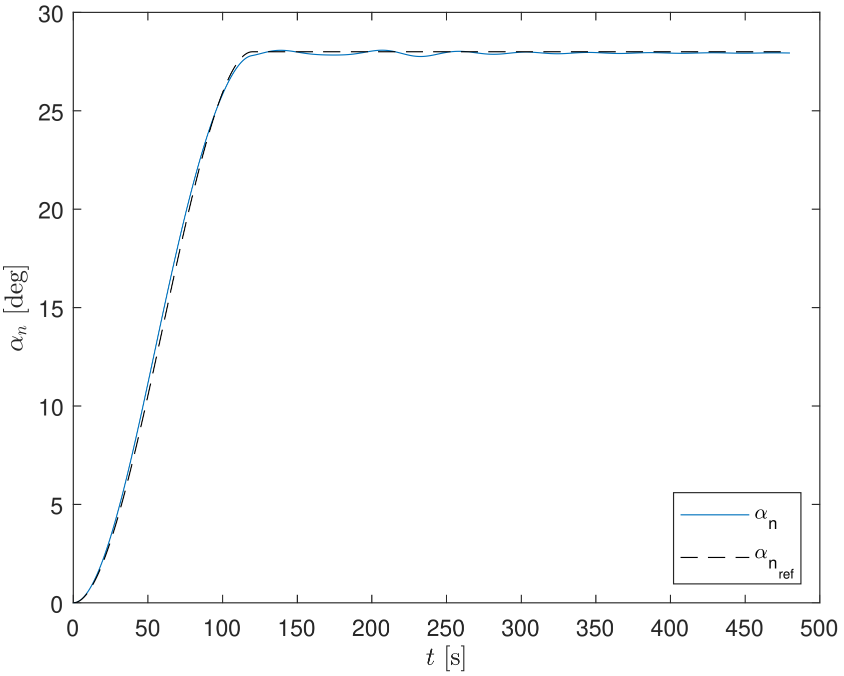

Figure 4.8 Pitch angle α_n evolution using LQR to reach a final pitch $\alpha_{nf} = 28.2°$.

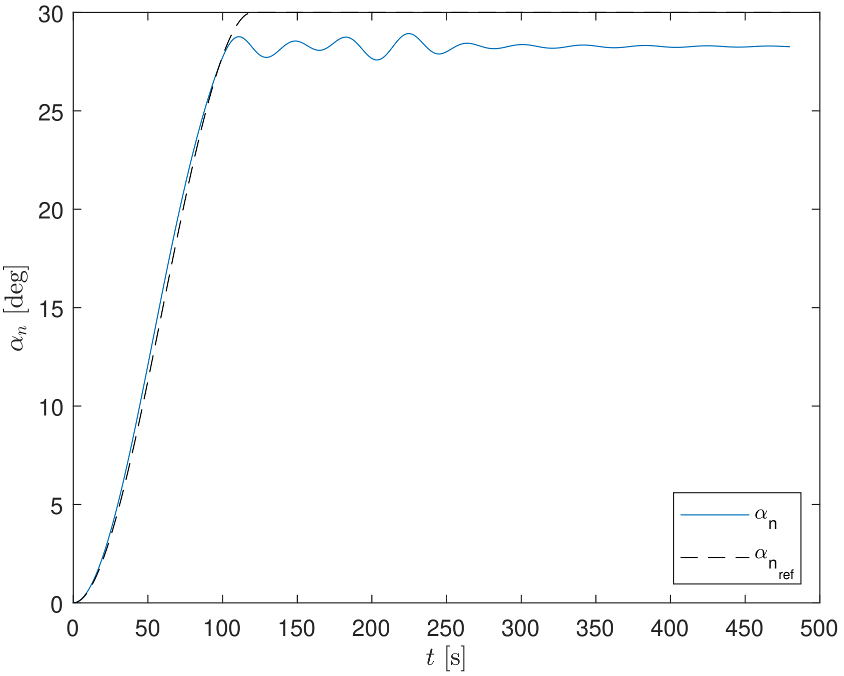

Figure 4.9 Pitch angle α_n evolution using LQR to reach a final pitch $\alpha_{nf} = 30°$.

Regarding the E-sail state variables, on the one hand, the Euler angles θ and ψ show the expected reference behaviour and ϕ suffers some oscillations until reaching a permanent regime with a value close to the reference (Figures 4.10-4.12).

On the other hand, angular velocities around x and y axes behave as reference state, but the nominal angular velocity Ω_z experiences a slight increase that can be associated to different dynamic equilibrium at the new attitude (Figures 4.13-4.15). In fact, this velocity gain is increased when increasing final pitch, at least inside the current interval of study.

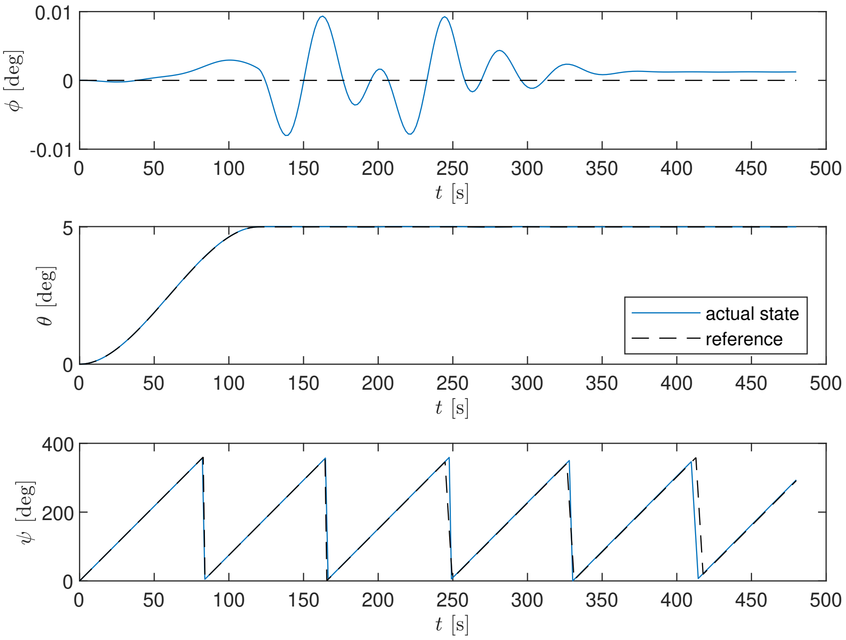

Figure 4.10 Attitude evolution using LQR to reach a final pitch $\alpha_{nf} = 5°$.

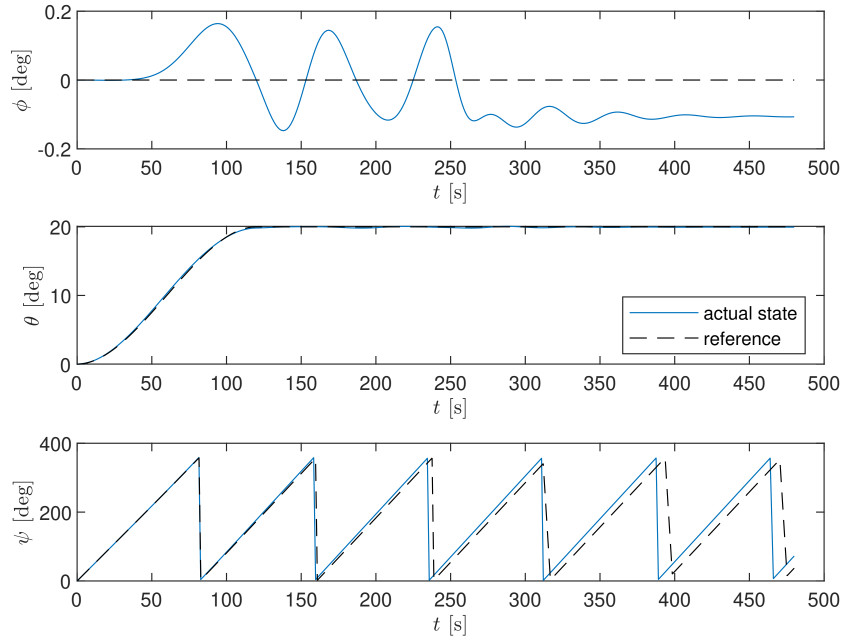

Figure 4.11 Attitude evolution using LQR to reach a final pitch $\alpha_{nf} = 20°$.

As additional remark, control saturation effects can be observed in attitude and angular velocity of $\alpha_{nf} = 30°$ case, as some oscillations appear due to the fact that the E-sail's control power is not enough to reach the reference state.

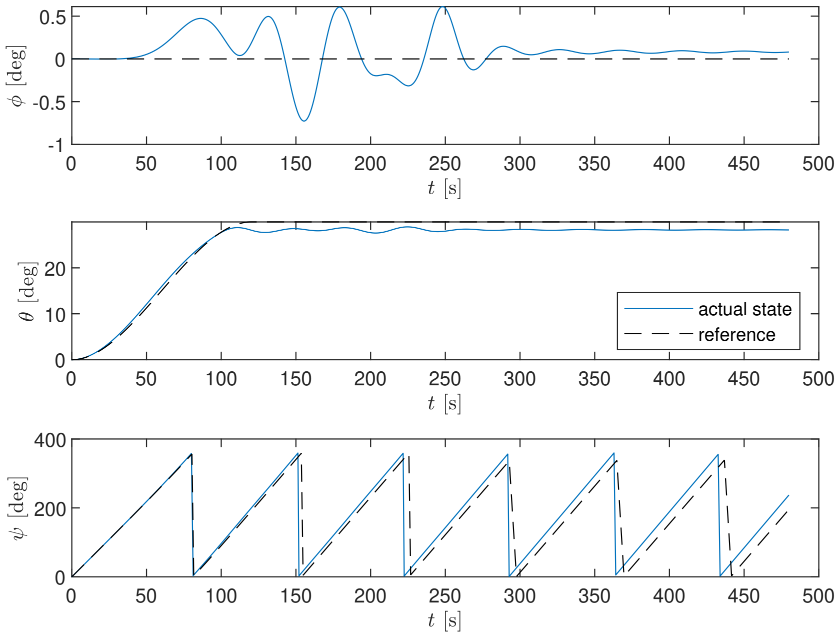

Figure 4.12 Attitude evolution using LQR to reach a final pitch $\alpha_{nf} = 30°$.

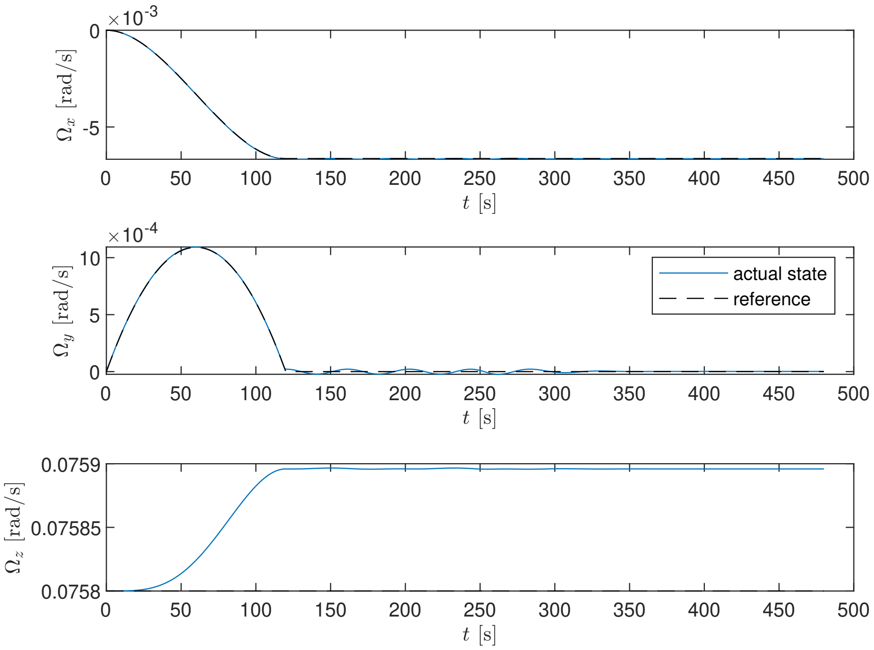

Figure 4.13 Angular velocity evolution using LQR to reach a final pitch $\alpha_{nf} = 5°$.

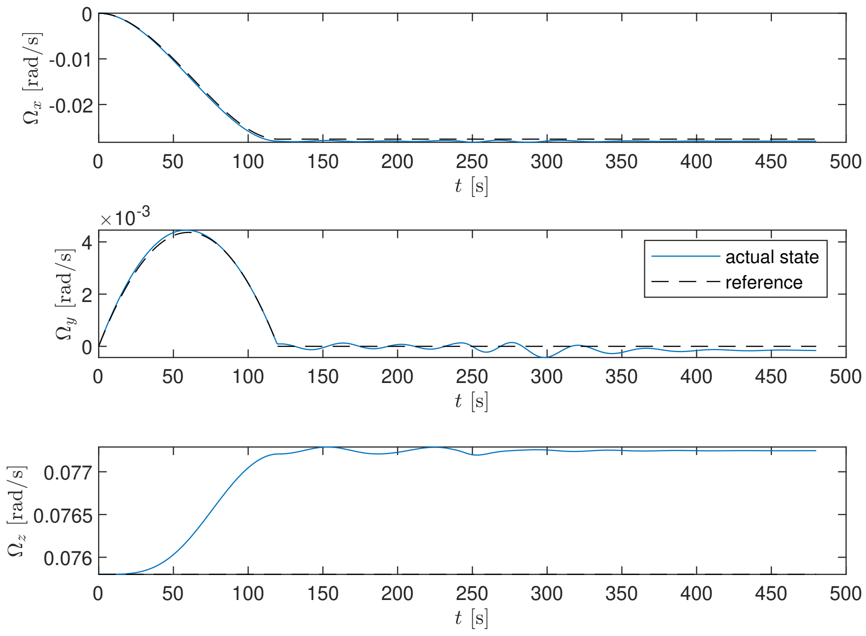

Figure 4.14 Angular velocity using LQR to reach a final pitch $\alpha_{nf} = 20°$.

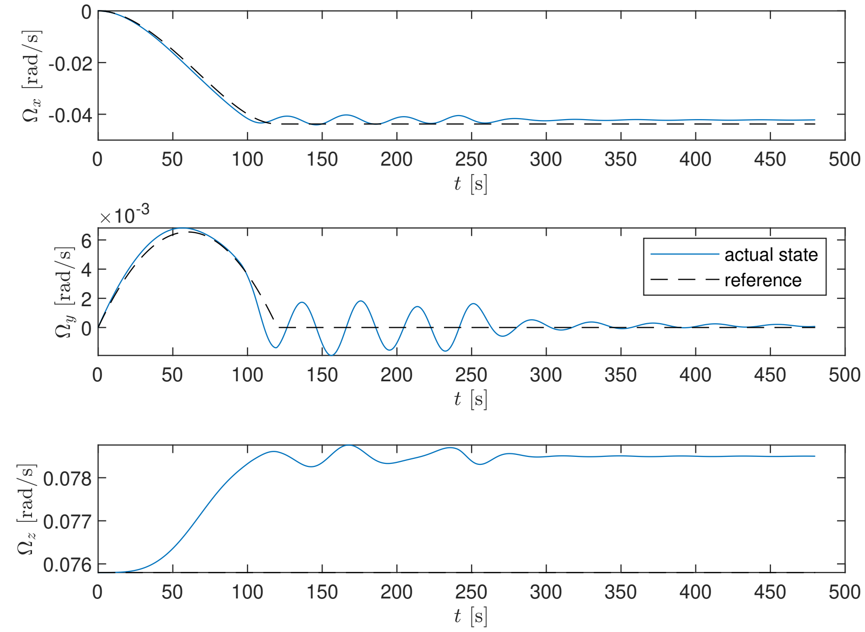

Figure 4.15 Angular velocity using LQR to reach a final pitch $\alpha_{nf} = 30°$.

Finally, the control input resulting from LQR controller is analyzed. In Figures 4.16-4.17, all the tethers' voltages stay below the saturation limit and characterized by a smooth evolution to reach the permanent regime value at the end of the slew maneuver. As expected, the control power demand increases when asking to reach a bigger final pitch angl. However, this increase is stopped at saturation limit, as it can be seen in the case of $\alpha_{nf} = 30°$ (Figure 4.19), where 6 tethers are affected by saturation and cannot achieve the voltage that LQR controller is requiring.

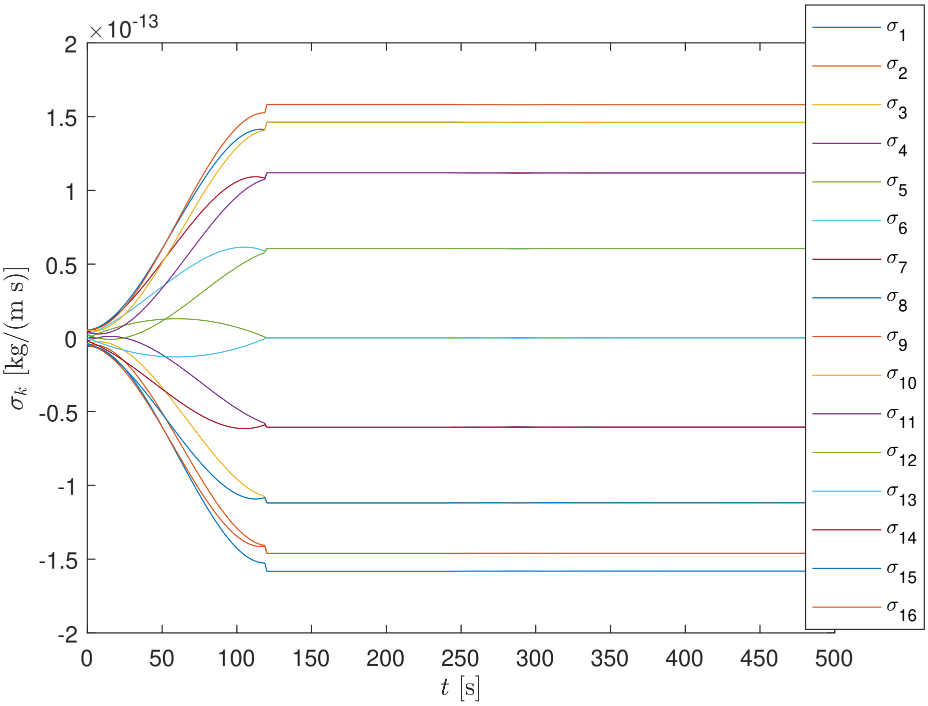

Figure 4.16 Control variables evolution using LQR to reach a final pitch $\alpha_{nf} = 5°$.

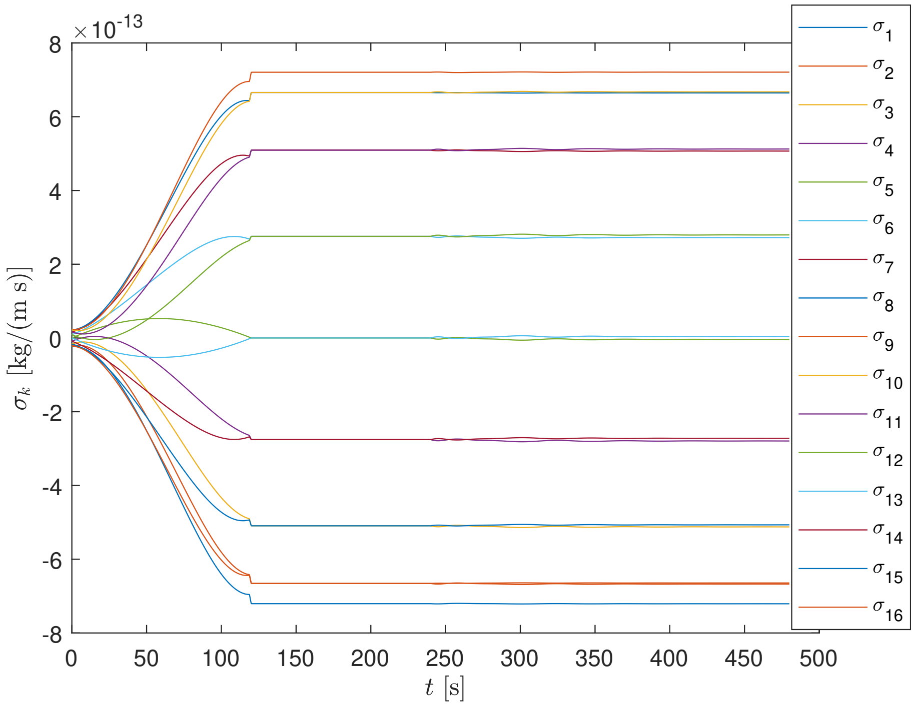

Figure 4.17 Control variables using LQR to reach a final pitch $\alpha_{nf} = 20°$.

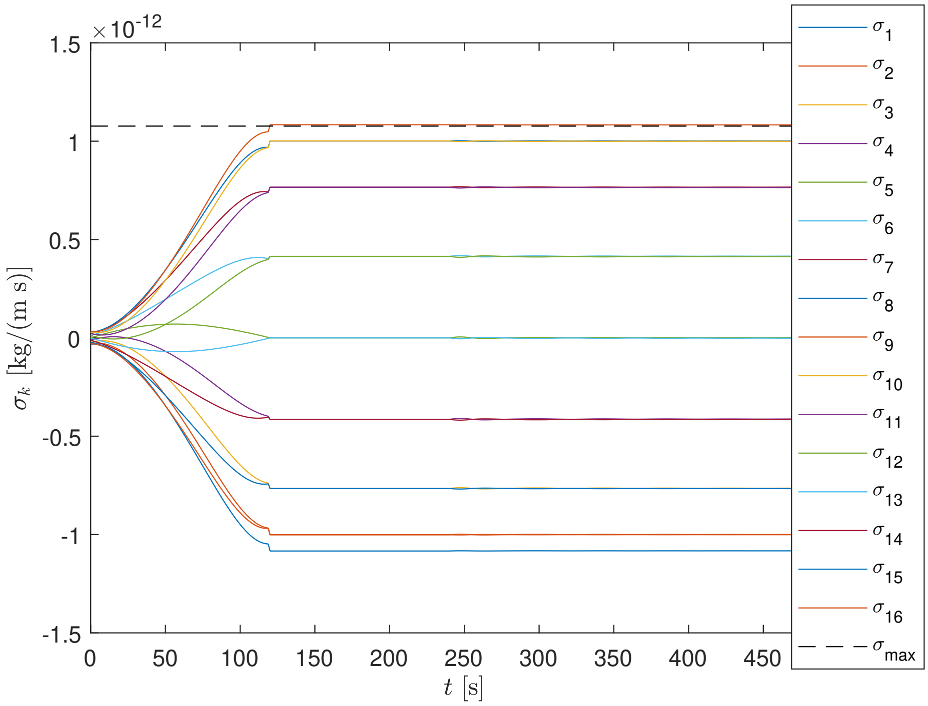

Figure 4.18 Control variables using LQR to reach a final pitch $\alpha_{nf} = 28.2°$.

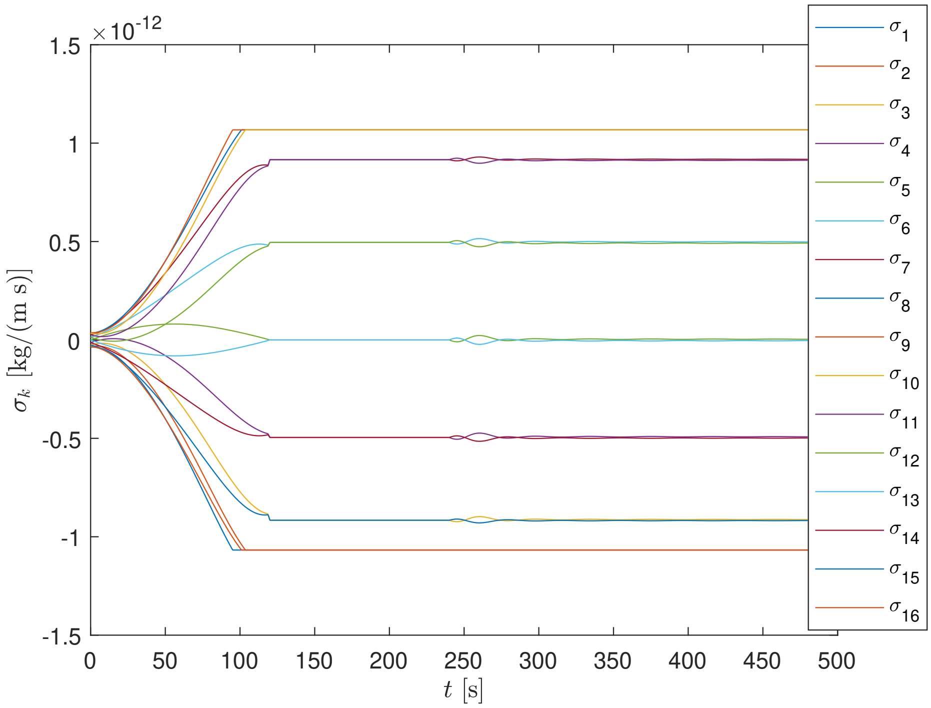

Figure 4.19 Control variables using LQR to reach a final pitch $\alpha_{nf} = 30°$.

4.2.2 Analysis beyond control saturation

The previous section studies are limited by an imposed technological constraint that limits the maximum voltage which can be applied to a tether in reality. However, we could disregard the control saturation to analyze the theoretical limits of our E-sail model, just in case those technical limits are surpassed in future developments. Hence, we perform again the same simulations, but increasing the desired pitch angles to 45, 60 and 70 degrees, in order to represent the particular E-sail behaviour at big pitch angles.

Again, beginning with the pitch angle response, Figures 4.20-4.22 represent three paradigmatic cases:

- When increasing the desired pitch angle to $\alpha_{nf} = 45^\circ$, the controller loses some accuracy at permanent regime, providing a pitch close to the reference but 1 degree lower and, also, with some non-damped oscillation.
- Around $\alpha_{nf} = 60^\circ$, the E-sail's response is just the expected, like in the cases studied in Section 4.2.1.
- In the case of $\alpha_{nf} = 70^\circ$, the controller does not work anymore as expected, obtaining pitch angles 10 degrees over the desired one.

As a conclusion, we could affirm that the theoretical validity for the E-sail controller model is extended until a pitch angle of 65 degrees approximately, which is inside the E-sail's practical limit that current studies and simulations are deducing (60-70 degrees) [5].

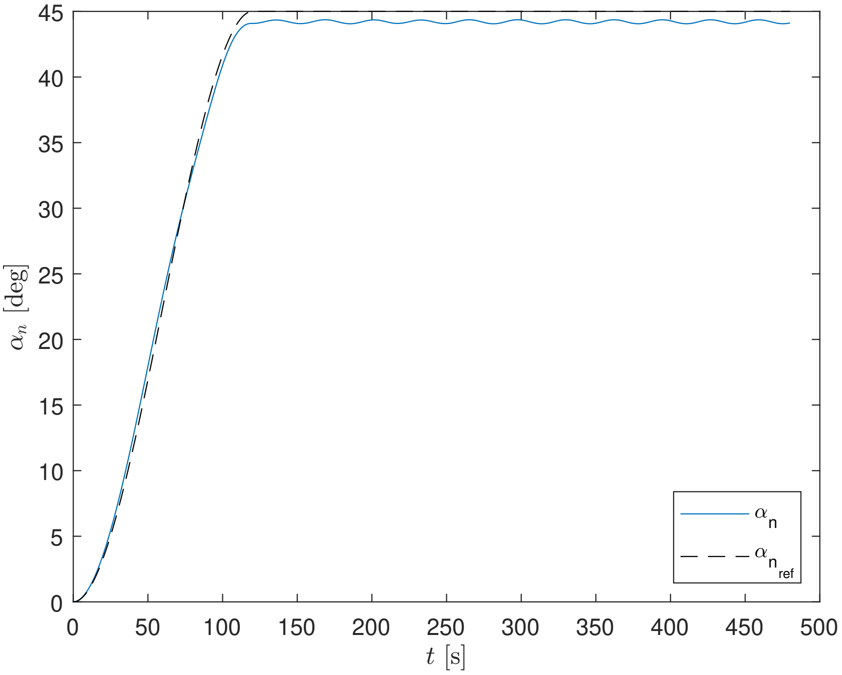

Figure 4.20 Pitch angle α_n evolution using LQR to reach a final pitch $\alpha_{nf} = 45^\circ$.

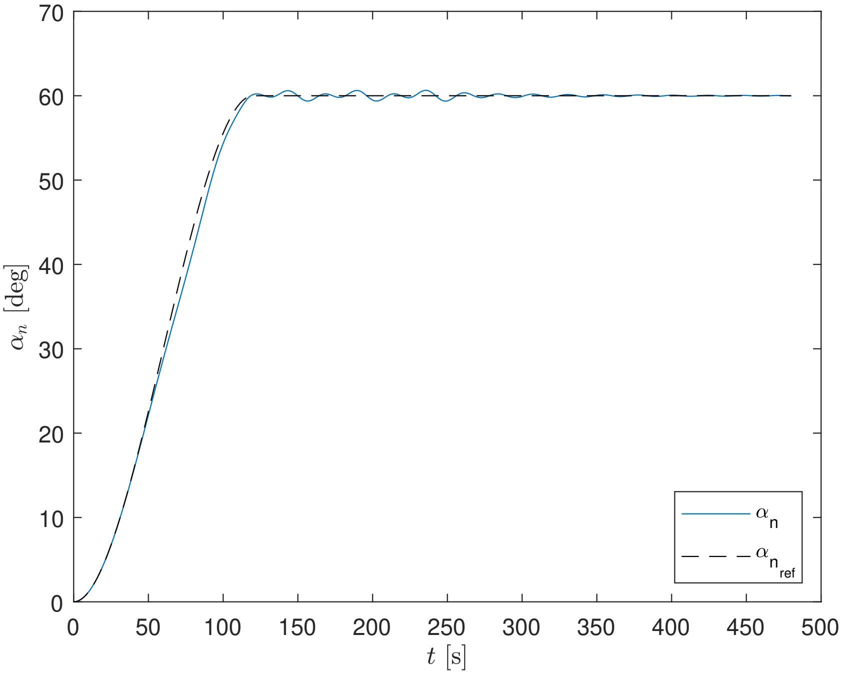

Figure 4.21 Pitch angle α_n evolution using LQR to reach a final pitch $\alpha_{nf} = 60°$.

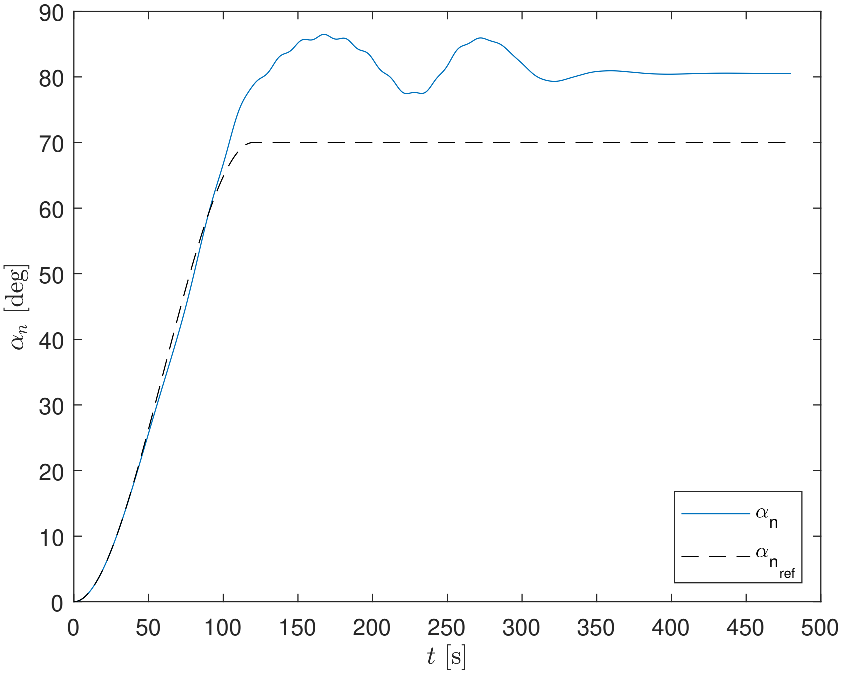

Figure 4.22 Pitch angle α_n evolution using LQR to reach a final pitch $\alpha_{nf} = 70°$.

This behaviour in pitch response can be explained by analyzing the resulting attitude and angular velocity. Looking into Figures 4.26-4.28, the main difference is observed in Ω_z evolution: this angular velocity increases in $\alpha_{nf} = 45°$ case as happened in Section 4.2.1, but remains constant for $\alpha_{nf} = 60°$ and, by contrast, decreases when $\alpha_{nf} = 70°$. This evolution impacts directly on ψ increase rate, as it is shown in Figures 4.23-4.25, and could be related to the pitch response accuracy.

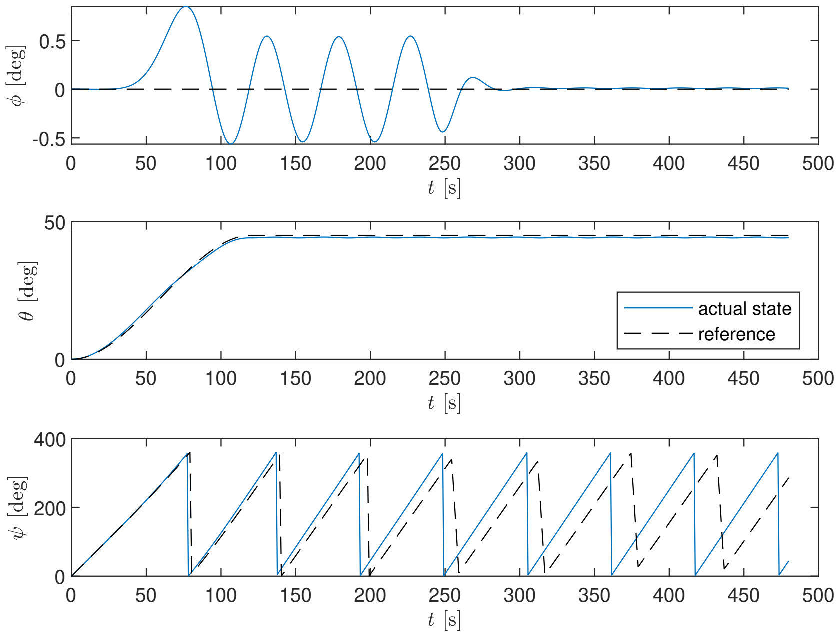

Figure 4.23 Attitude evolution using LQR to reach a final pitch $\alpha_{nf} = 45°$.

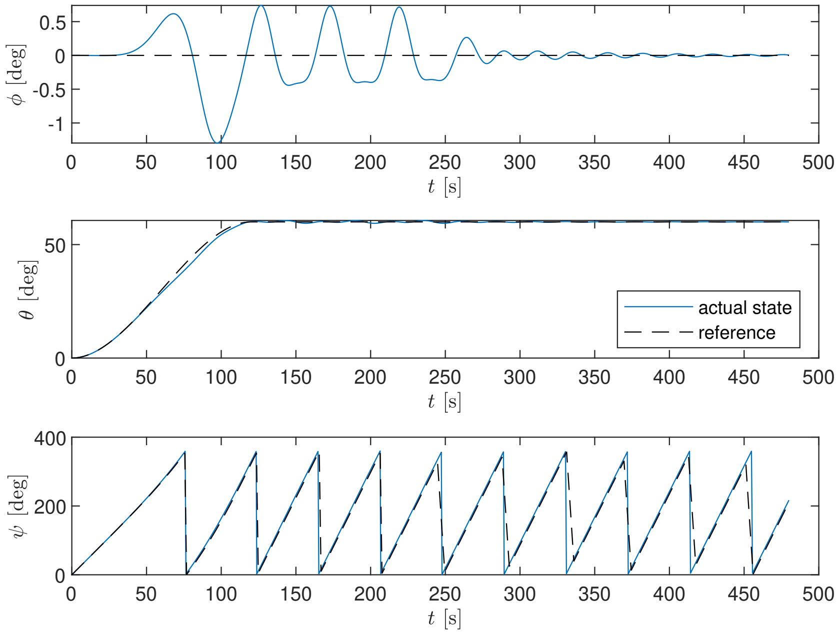

Figure 4.24 Attitude evolution using LQR to reach a final pitch $\alpha_{nf} = 60°$.

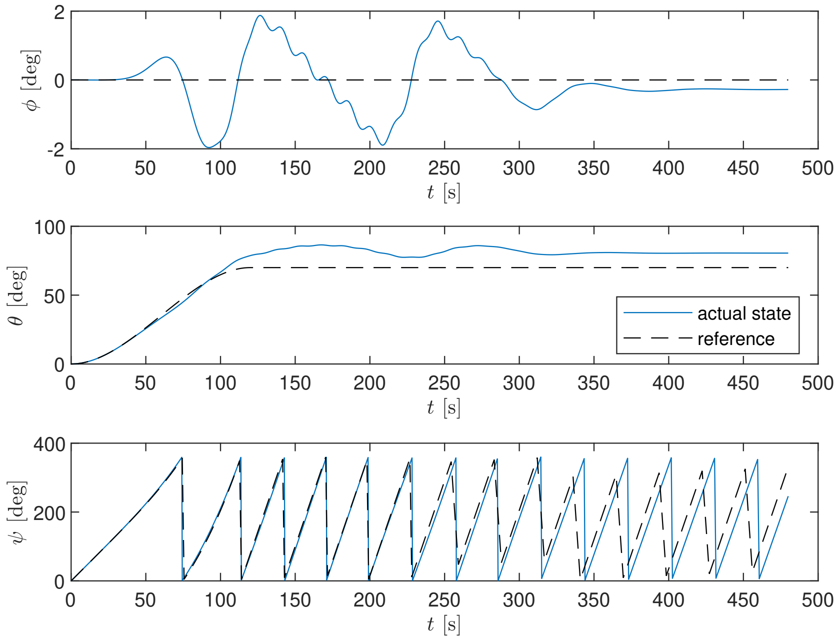

Figure 4.25 Attitude evolution using LQR to reach a final pitch $\alpha_{nf} = 70°$.

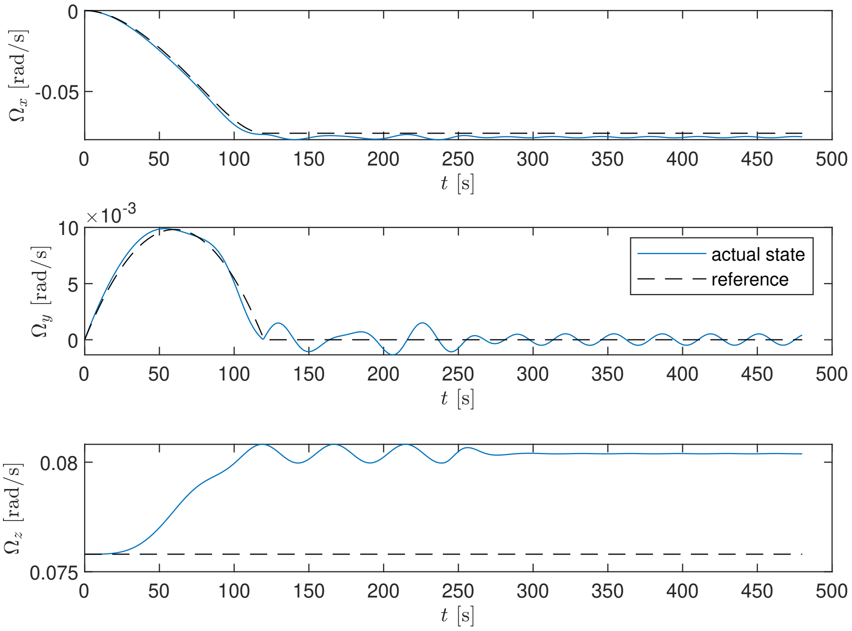

Figure 4.26 Angular velocity evolution using LQR to reach a final pitch $\alpha_{nf} = 45°$.

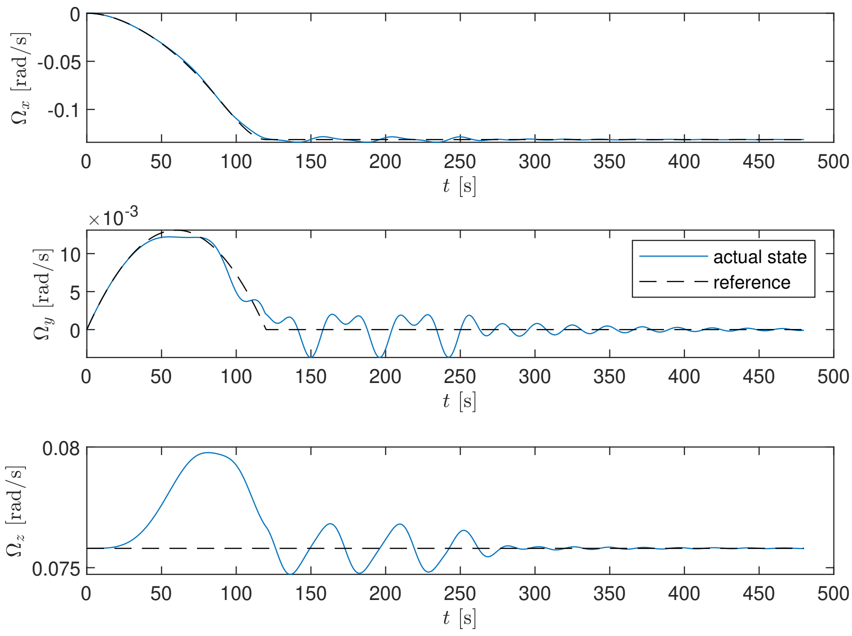

Figure 4.27 Angular velocity using LQR to reach a final pitch $\alpha_{nf} = 60°$.

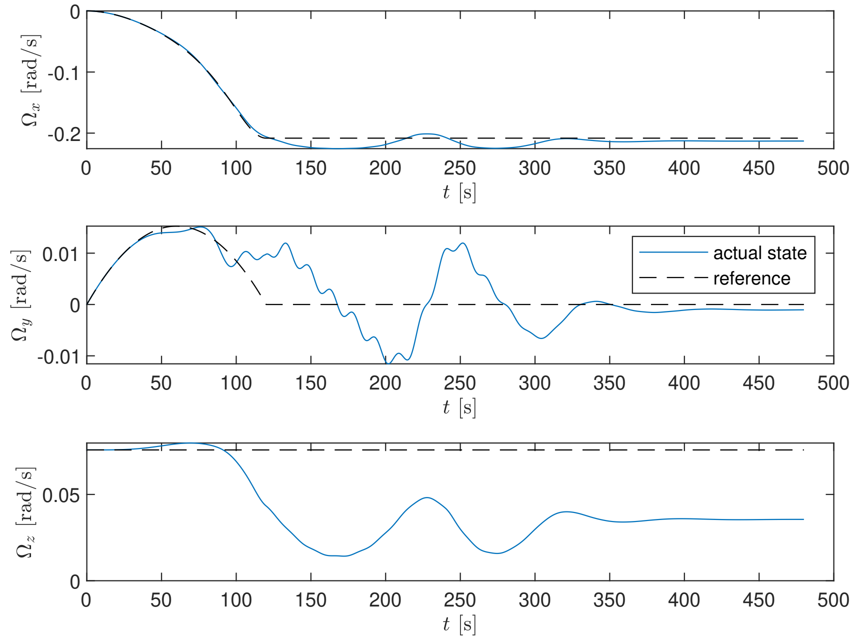

Figure 4.28 Angular velocity using LQR to reach a final pitch $\alpha_{nf} = 70°$.

Finally, the control input variables σ_k are represented in Figures 4.29-4.22, where the typical behaviour is observed and the maximum values get specially excessive in the case of $\alpha_{nf} = 70°$, where it reaches one order of magnitude above nominal σ.

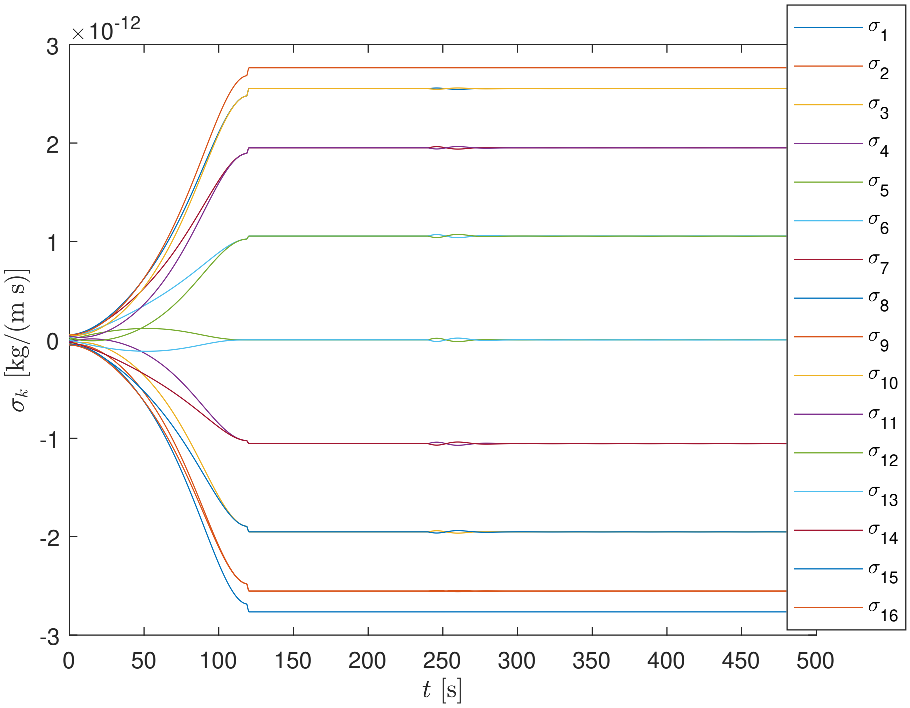

Figure 4.29 Control variables evolution using LQR to reach a final pitch $\alpha_{nf} = 45°$.

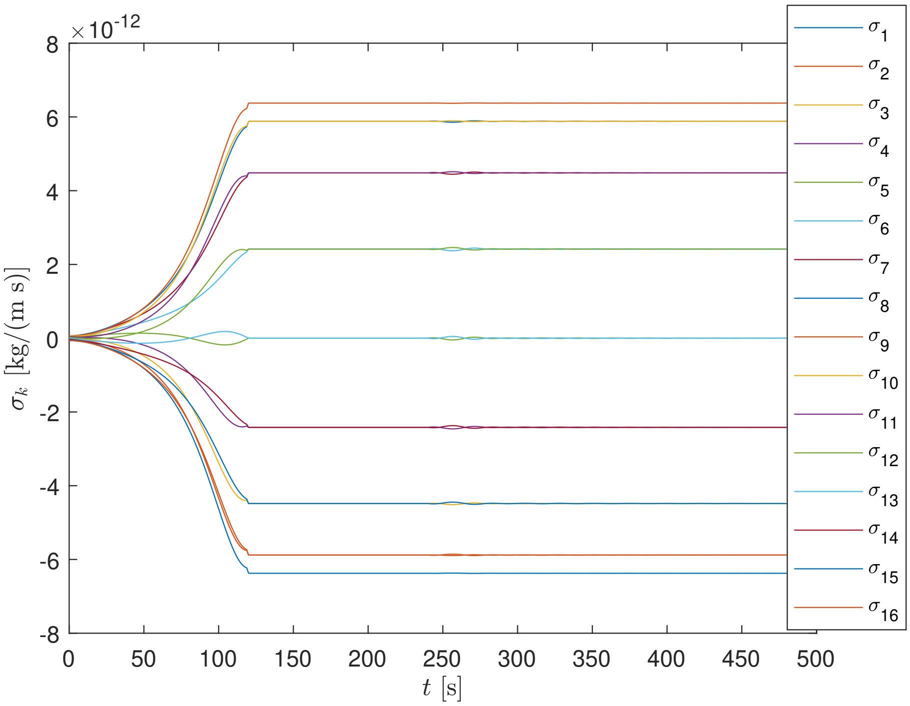

Figure 4.30 Control variables using LQR to reach a final pitch $\alpha_{nf} = 60°$.

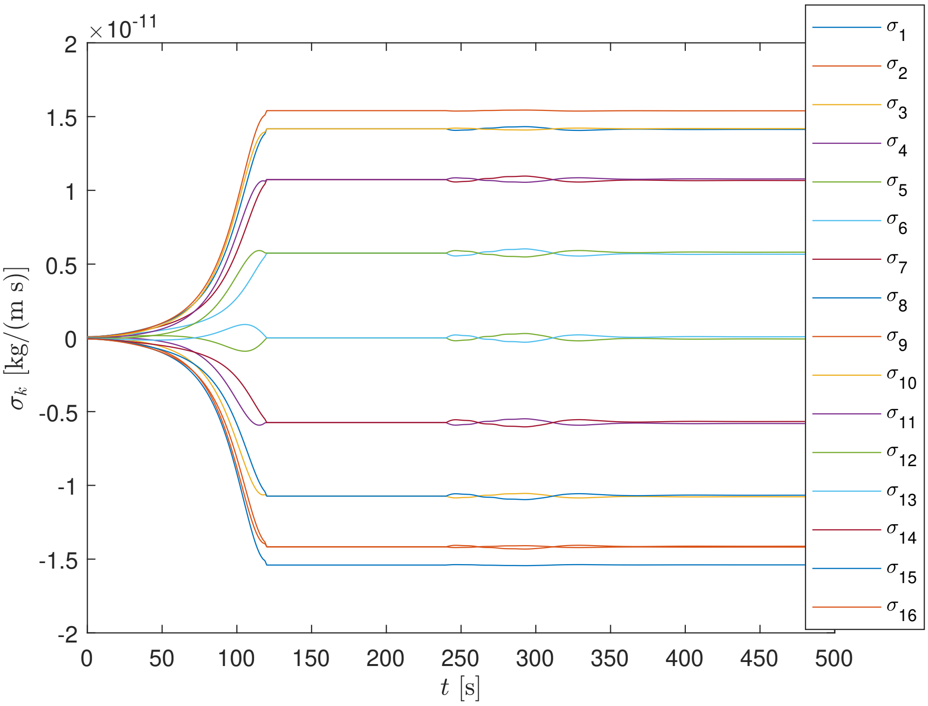

Figure 4.31 Control variables using LQR to reach a final pitch $\alpha_{nf} = 70°$.

4.3 LQG control results

The aim of this section is to perform a similar study to that performed in Section 4.2, but now introducing a white Gaussian noise for system disturbance, with standard deviation $\sigma_v = 10^{-4}$ rad/s^2, as well as for gyroscopes' measurements, with deviation $\sigma_w = 5 \cdot 10^{-4}$ rad/s. In this case, the Linear Quadratic Gaussian control designed in Section 3.5 is applied, and analyzed during a simulation time of 12 minutes.

4.3.1 Noise effects on operative maneuver range

Simulating the maneuver with noise inside the pitch operating range deduced in Section 4.2 (i.e., from 0 to 28 degrees), the objective is to check if this range is still applicable when applying the LQG control. Therefore, three cases are studied: final pitch $\alpha_{nf} = 5°$ and $\alpha_{nf} = 20°$ to verify the correct behaviour inside the model's validity pitch interval and, also, the case of $\alpha_{nf} = 30°$ to check saturation limit.

Beginning with pitch angle response, shown in Figures 4.32-4.34, we can state that the LQG controller is generating an accurate maneuver, filtering the possible mean perturbations, although a slight (nearly negligible) and stable oscillation around the reference is appreciated at permanent regime.

At final pitch angle 30 degrees, it is possible to observe again control saturation, that causes a larger oscillation in permanent regime, altough stably maintained around the saturation limit located around 28 degrees.

If we look into the simulated gyroscopes' measurements, represented in Figures 4.35-4.34, it is possible to compare the noisy angular velocities measurements with the smooth estimates performed by Kalman filter, which are close to real angular velocities. Here we can observe also how the previously commented slight low-frequency oscillation is not completely filtered, specially when saturation occurs.

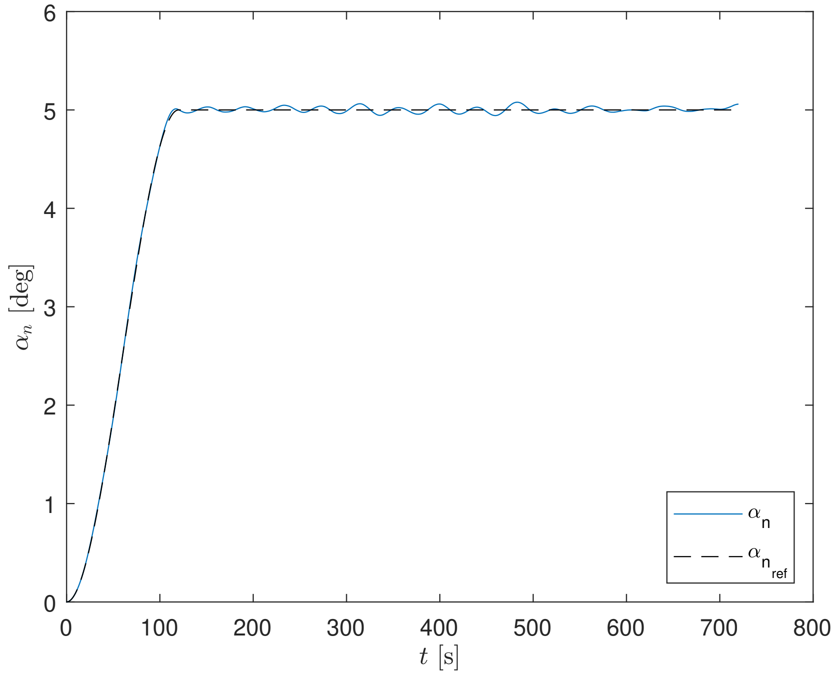

Figure 4.32 Pitch angle α_n evolution using LQG to reach a final pitch $\alpha_{nf} = 5°$.

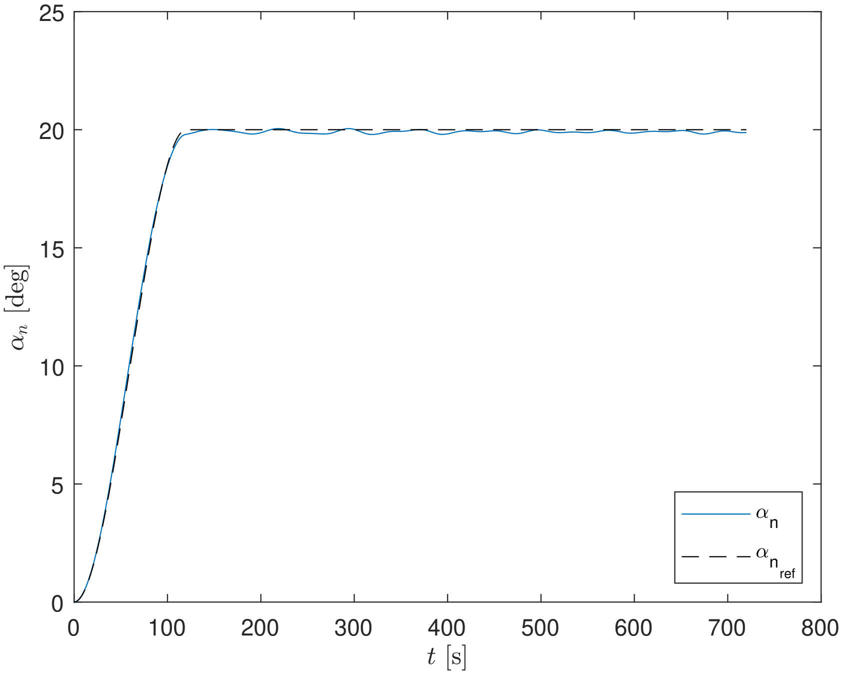

Figure 4.33 Pitch angle α_n evolution using LQG to reach a final pitch $\alpha_{nf} = 20°$.

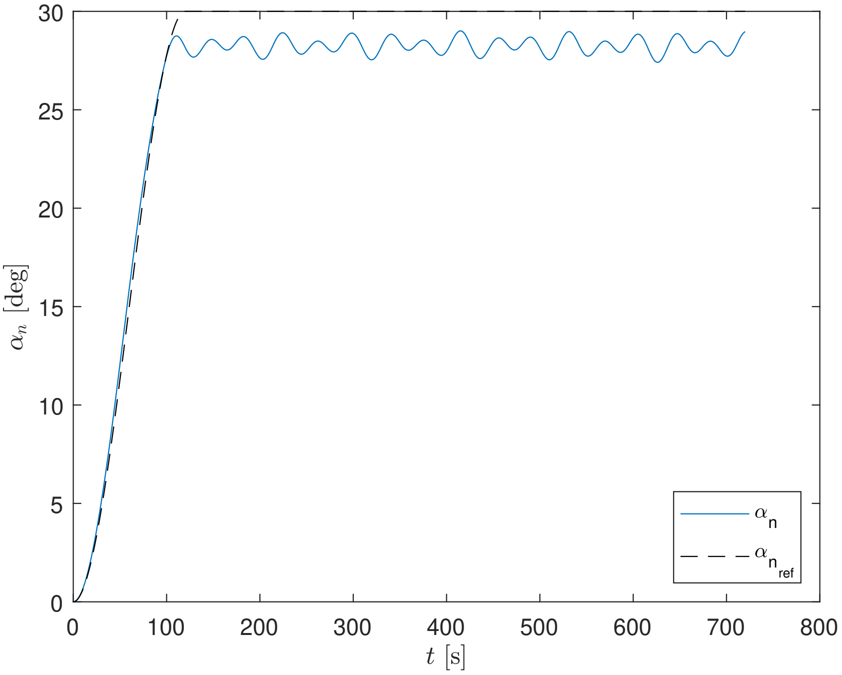

Figure 4.34 Pitch angle α_n evolution using LQG to reach a final pitch $\alpha_{nf} = 30°$.

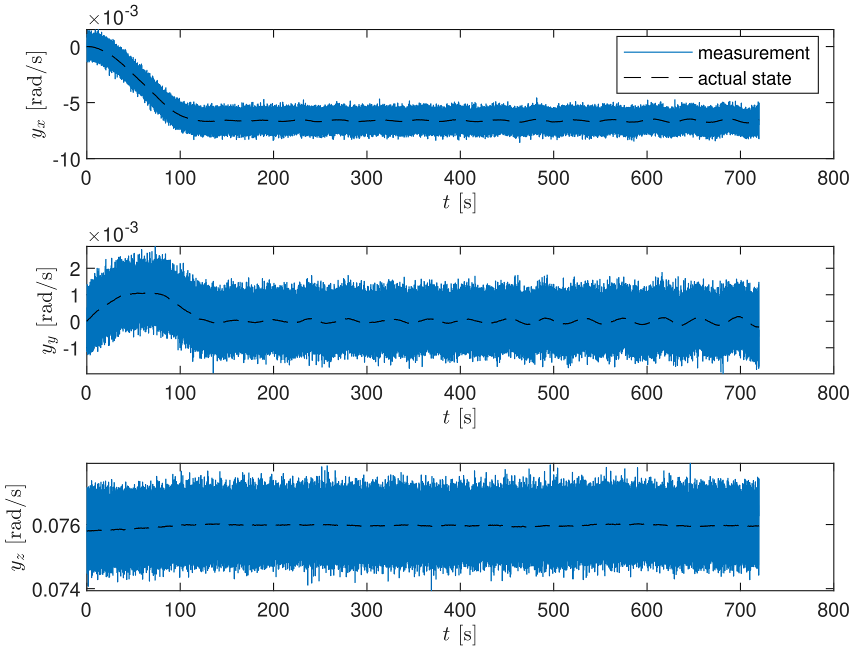

Figure 4.35 Angular velocity measurements evolution for LQG to reach a final pitch $\alpha_{nf} = 5°$.

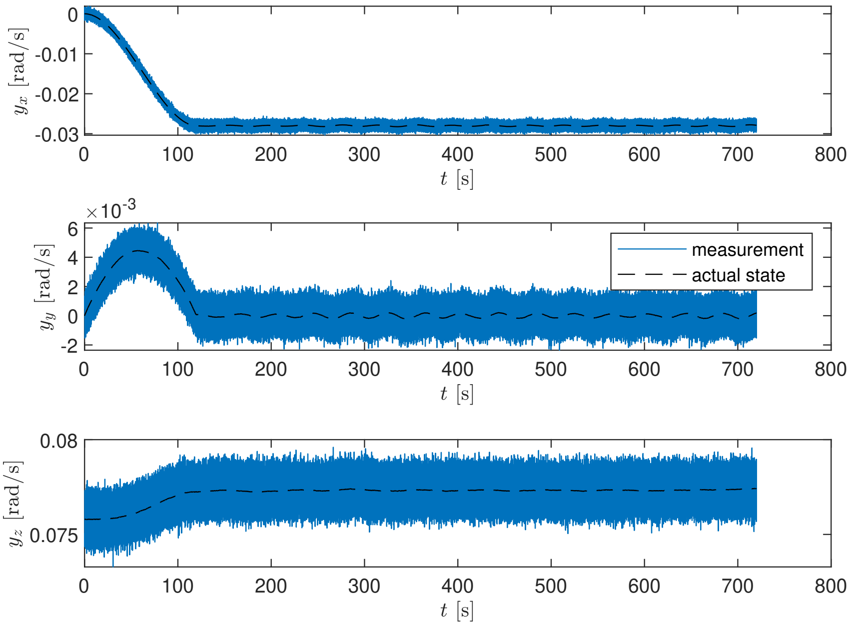

Figure 4.36 Angular velocity measurements evolution for LQG to reach a final pitch $\alpha_{nf} = 20°$.

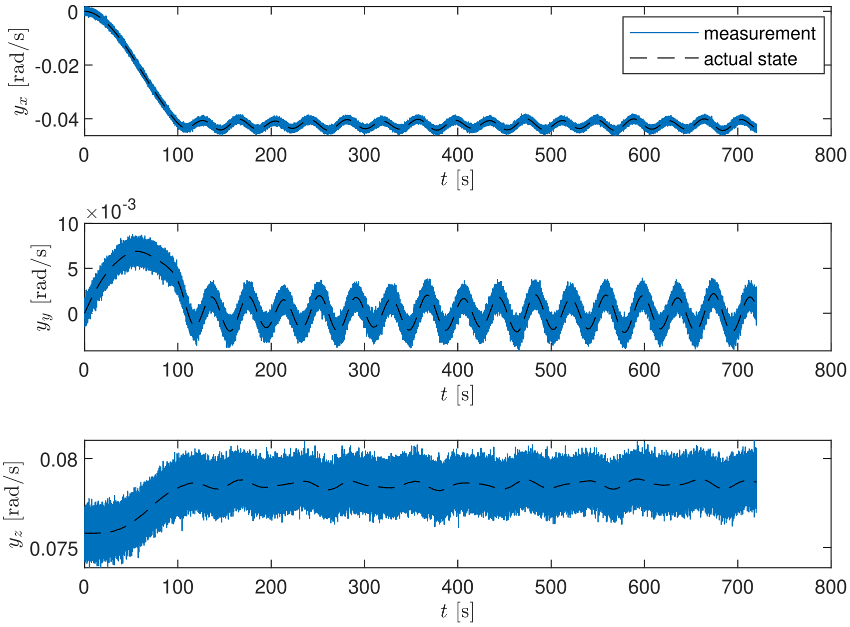

Figure 4.37 Angular velocity measurements evolution for LQG to reach a final pitch $\alpha_{nf} = 30°$.

As the attitude is estimated from the instruments' measurements using the Kalman filter, the oscillation effects are propagated to the Euler angles, altough the overall behaviour is comparable to that studied in Section 4.2.

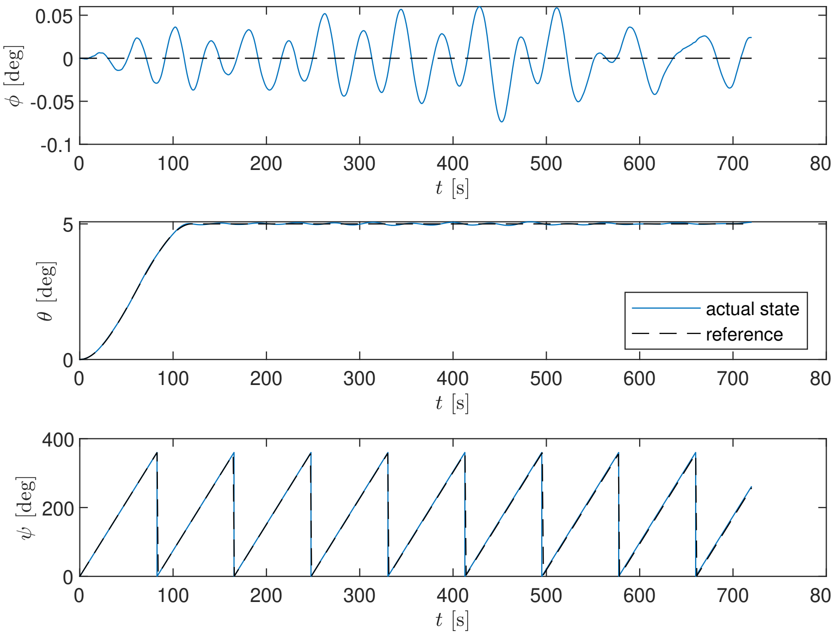

Figure 4.38 Attitude evolution using LQG to reach a final pitch $\alpha_{nf} = 5°$.

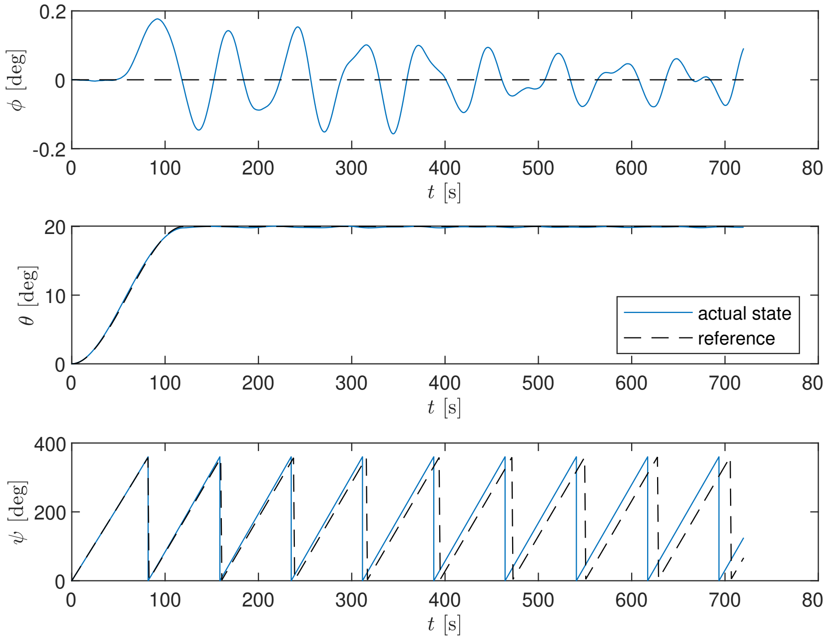

Figure 4.39 Attitude evolution using LQG to reach a final pitch $\alpha_{nf} = 20°$.

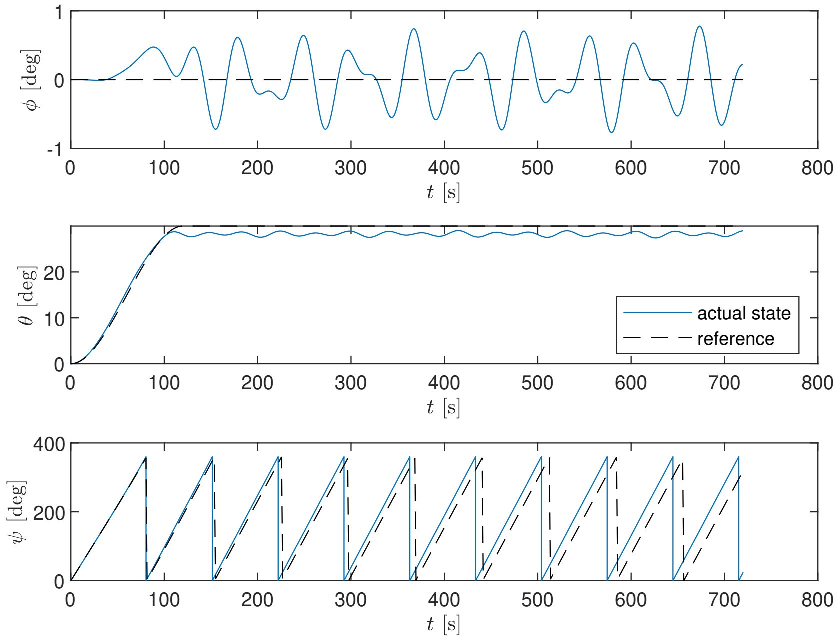

Figure 4.40 Attitude evolution using LQG to reach a final pitch $\alpha_{nf} = 30°$.

Finally, the tethers' control coefficients exhibit an analogous behaviour to that of LQR control in Section 4.2, so they are only depicted in Figures 4.41-4.43.

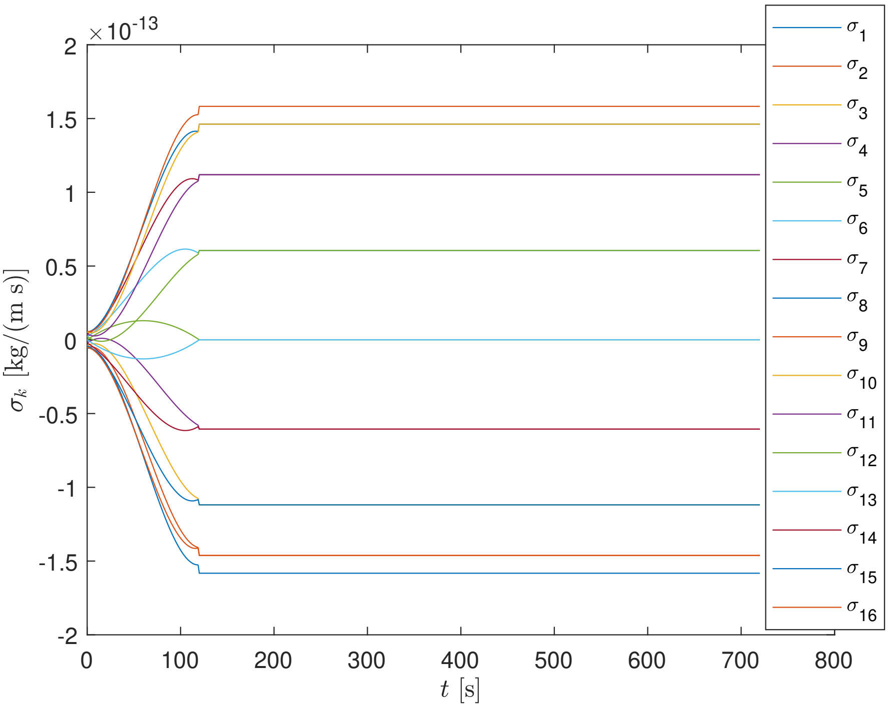

Figure 4.41 Control variables evolution using LQG to reach a final pitch $\alpha_{nf} = 5°$.

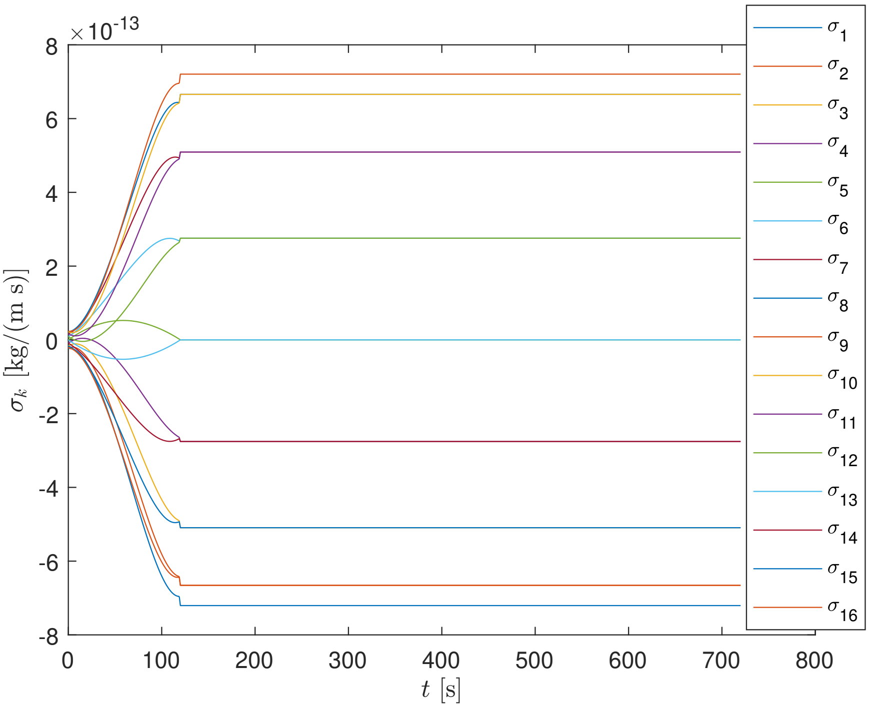

Figure 4.42 Control variables evolution using LQG to reach a final pitch $\alpha_{nf} = 20°$.

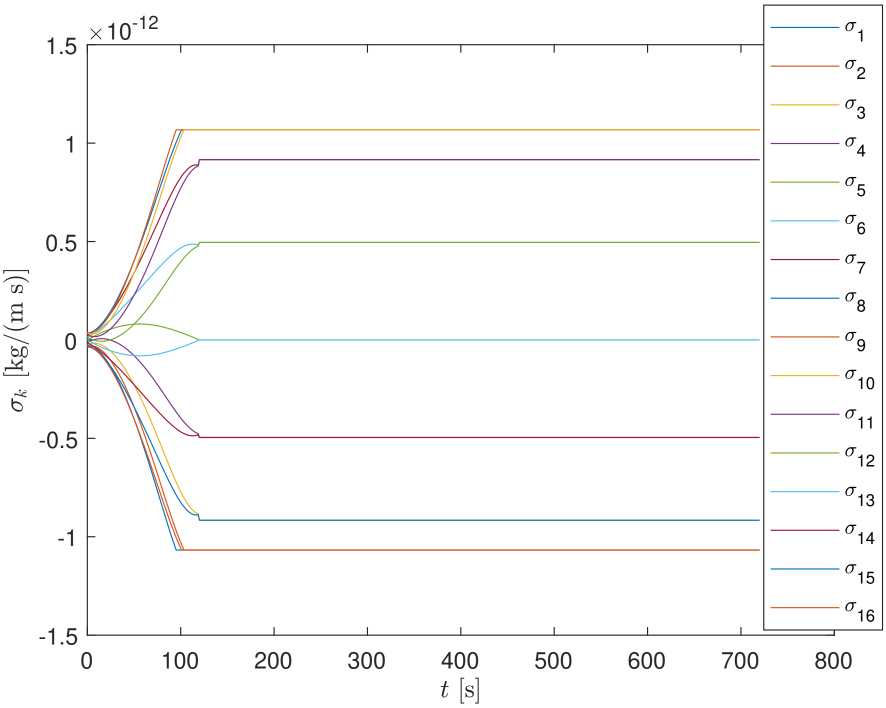

Figure 4.43 Control variables evolution using LQG to reach a final pitch $\alpha_{nf} = 30°$.

4.3.2 Noise effects on great pitch maneuvers

Once the LQG control has been validated inside the operative limits (due to control saturation) of the E-sail pitch change maneuver, the following step is to test it under great values of the pitch angle, near to the previously defined theoretical limit of 65 degrees.

Thus, simulating a maneuver until $\alpha_{nf} = 60°$, it is possible to observe in Figure 4.44 that this desired pitch is reached and the final attitude stays close to the reference. Nevertheless, the oscillation appearing at low pitch angles happens in this case with a greater frequency, although keeping a low assumable error amplitude.

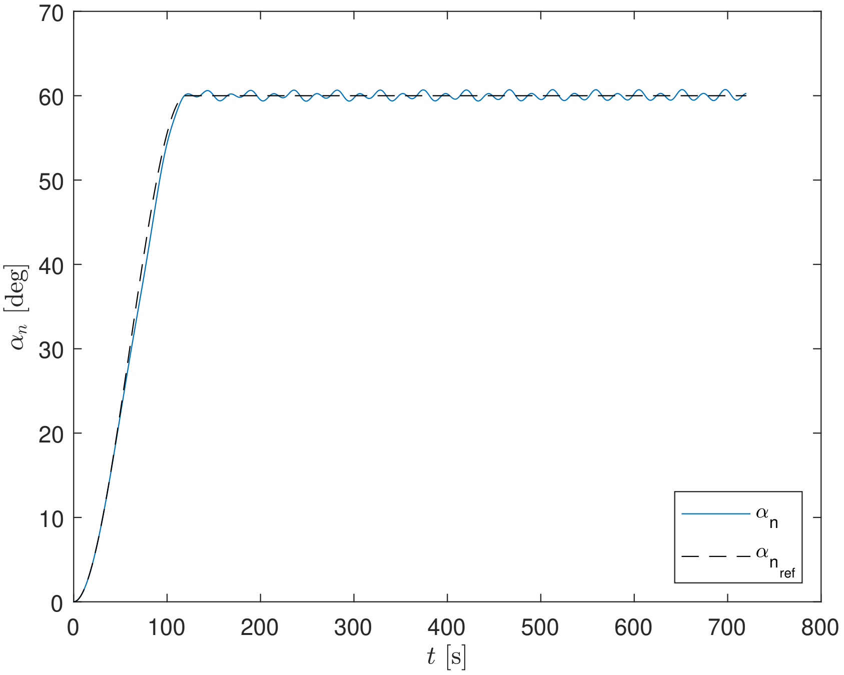

Figure 4.44 Pitch angle α_n evolution using LQG to reach a final pitch $\alpha_{nf} = 60°$.

This stable oscilatory motion in permanent regime is also observed in the state variables and the measurements, but always being around the defined reference values. In the case of the control variables, no distinguishable behaviour can be seen.

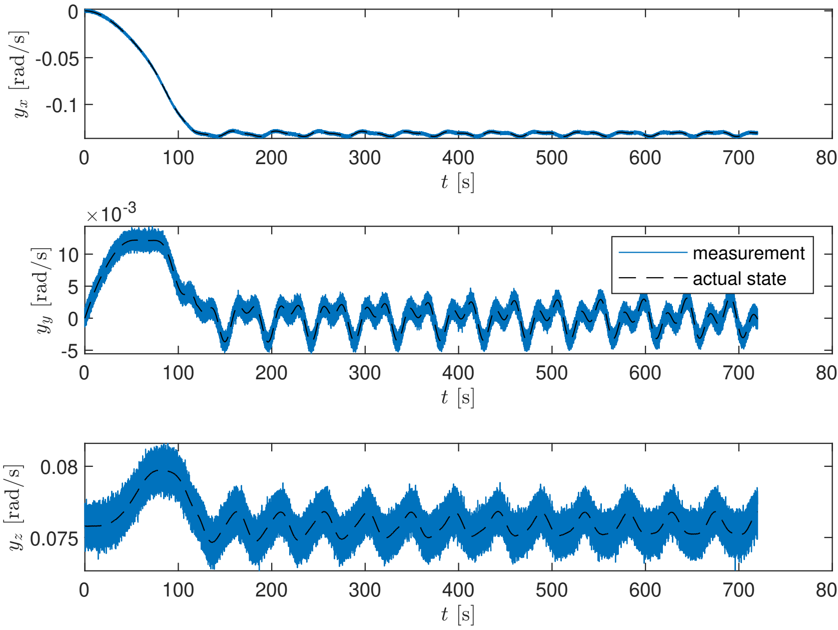

Figure 4.45 Angular velocity measurements evolution for LQG to reach a final pitch $\alpha_{nf} = 60^\circ$.

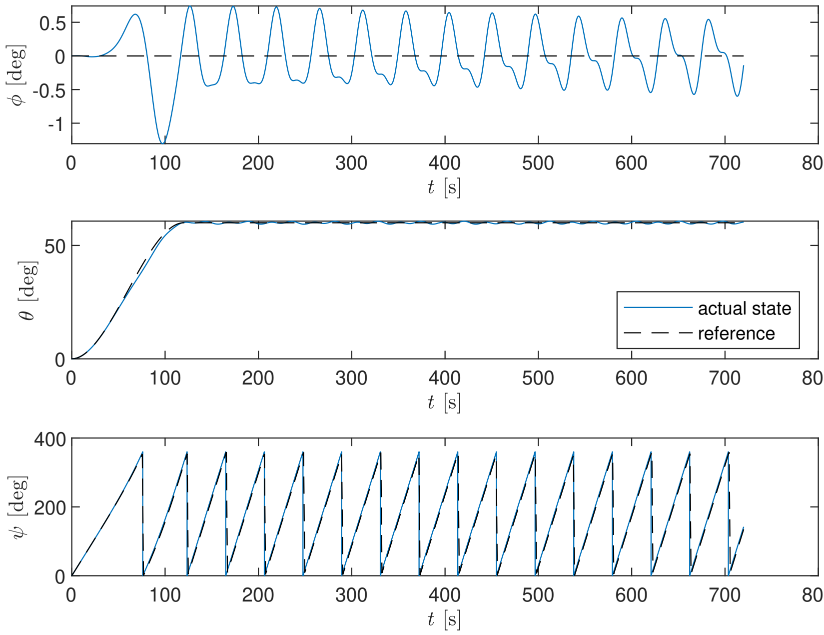

Figure 4.46 Attitude evolution using LQG to reach a final pitch $\alpha_{nf} = 60^\circ$.

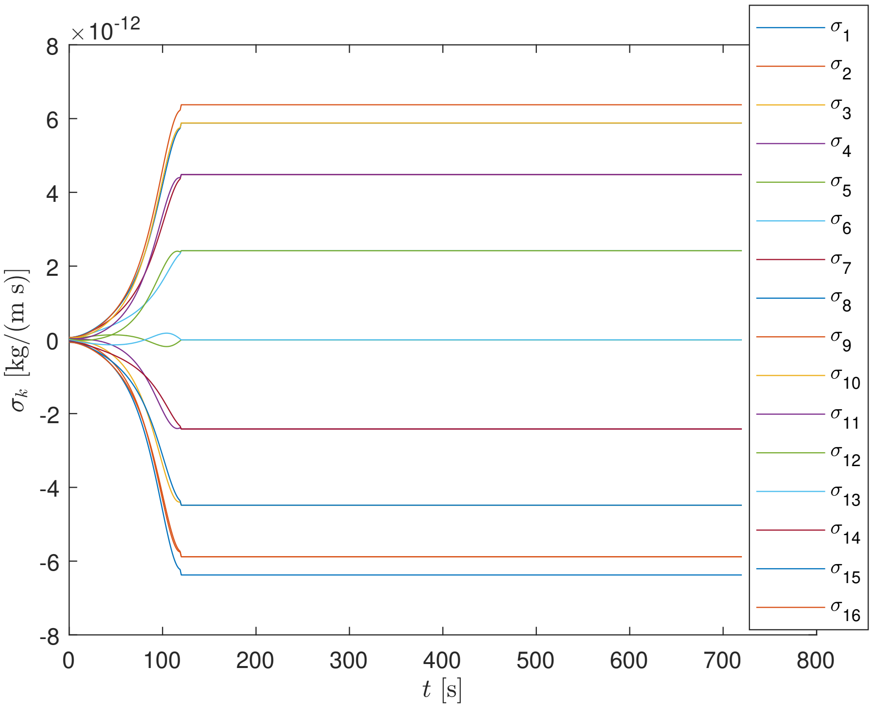

Figure 4.47 Control variables evolution using LQG to reach a final pitch $\alpha_{nf} = 60°$.

4.3.3 Influence of sensor quality on LQG controller response

As an additional study, it is interesting to test the E-sail's LQG control response under different noise intensity. Indeed, we have been analyzing a gyroscope with standard deviation $\sigma_w = 5 \cdot 10^{-4}$ rad/s, but we should study which is the behaviour when using a worse quality sensor in terms of white Gaussian noise standard deviation.

For this purpose, the E-sail maneuver is simulated under noise deviation $\sigma_w = 10^{-2}$ rad/s and desired pitch angle of 20 degrees, obtaining the pitch response shown in Figure 4.48. In this case, the measurement is so corrupted with noise, that the Kalman filter estimation of the E-sail's state variables is not so accurate as before. As a result, the final pitch is around half a degree lower from the desired one.

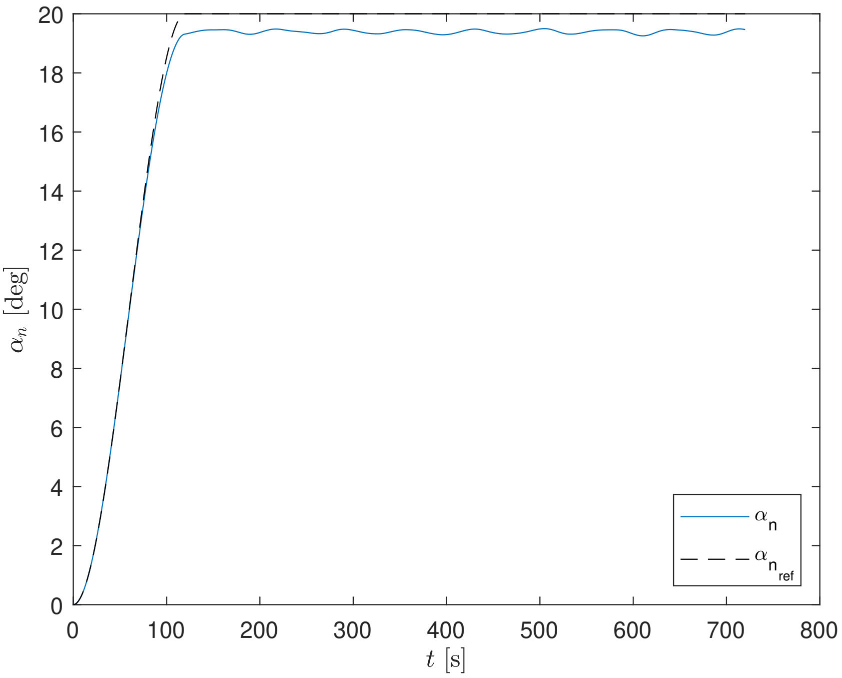

Figure 4.48 Pitch angle α_n evolution using LQG to reach a final pitch $\alpha_{nf} = 20°$, with sensor typical deviation $\sigma_w = 10^{-2}$ rad/s.

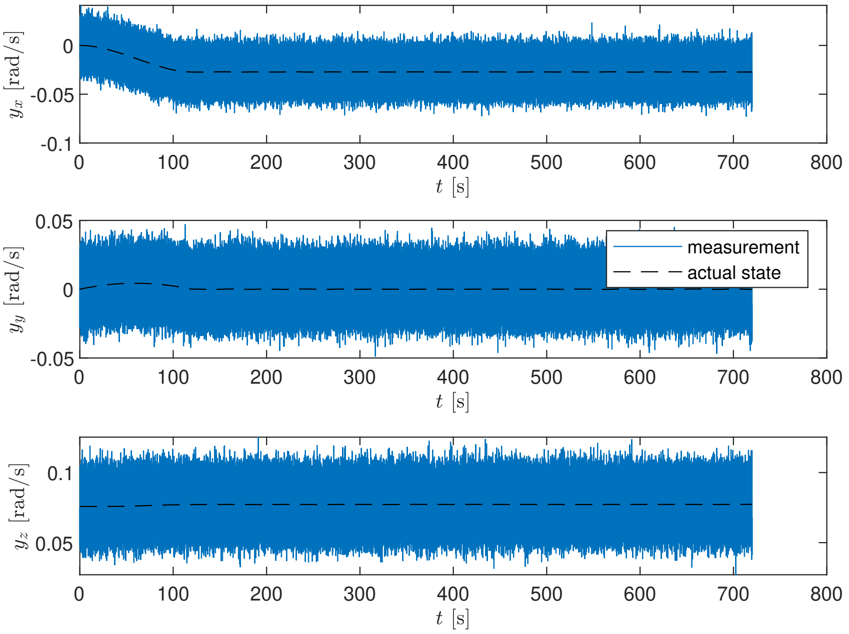

Figure 4.49 Angular velocity measurements evolution for LQG to reach a final pitch $\alpha_{nf} = 20°$, with sensor typical deviation $\sigma_w = 10^{-2}$ rad/s.

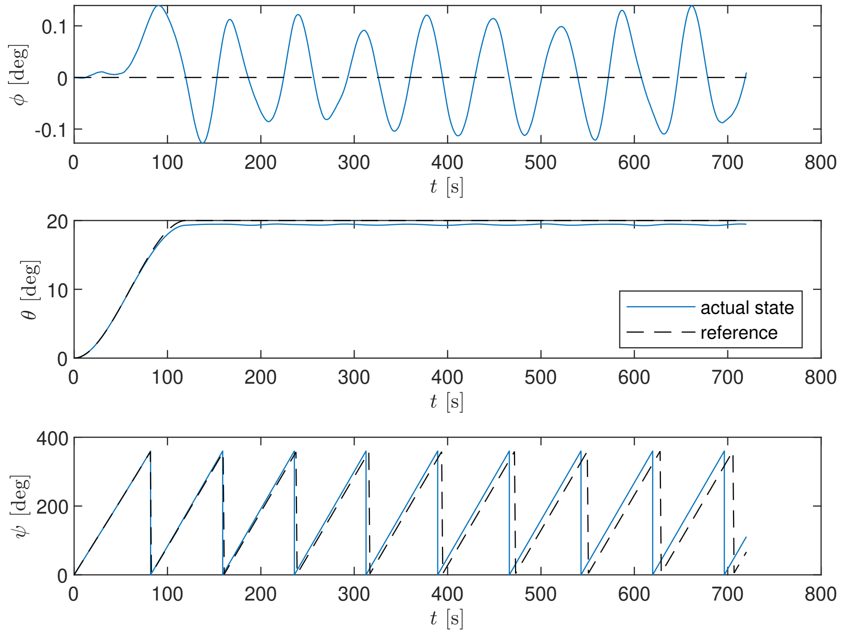

Figure 4.50 Attitude evolution using LQG to reach a final pitch $\alpha_{nf} = 20°$, with sensor typical deviation $\sigma_w = 10^{-2}$ rad/s.

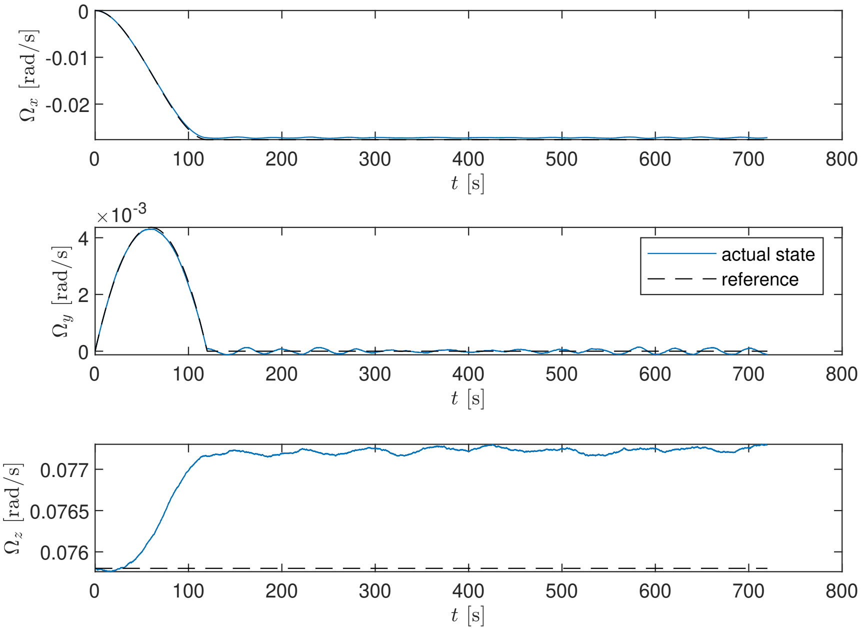

Figure 4.51 Angular velocity evolution using LQG to reach a final pitch $\alpha_{nf} = 20°$, with sensor typical deviation $\sigma_w = 10^{-2}$ rad/s.

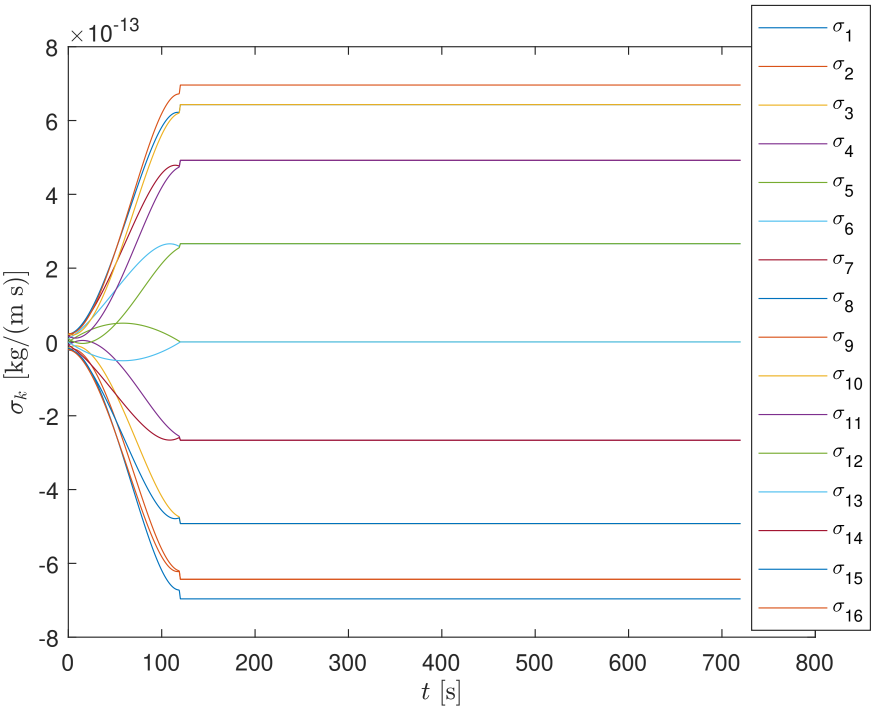

Figure 4.52 Control variables evolution using LQG to reach a final pitch $\alpha_{nf} = 20°$, with sensor typical deviation $\sigma_w = 10^{-2}$ rad/s.

5 Conclusions

A new tether deformed shape model has been proposed in this project, in order to study the E-sail dynamics under non-symmetrical configuration in which each tether is able to deform independently depending on the applied voltage and the relative orientation.

Firstly, the electric solar sails' state of art has been reviewed to understand the basic architecture and potential applications of this innovative propellantless propulsive technology, focusing on the current advances in terms of attitude control. Following the related works performed by Bassetto et al. [1] and Pérez et al. [2], where their symmetrical model allows attitude control (using direct and LQR control, respectively) valid for low pitch angles near to Sun-facing configuration, the objective of this project has been set to achieve controllability for a higher pitch range.

For this purpose, the non-symmetrical model for tethers' deformation has been defined in Section 2.1, based on the same logarithmic function for the deformed shape, but now proposing a procedure to compute the shape coefficient depending on the attitude and the applied voltage, independently for each tether. As a consequence, the expressions for the E-sail's torque components have been reformulated to include the new deformed shape model.

This model has been first analyzed in Section 4.1, looking into the dependencies of the shape coefficients, deducing two different behaviours: on the one hand, the tethers' deformation increases with the control voltage applied, as the solar wind forces would be higher; and, on the other, this deformation decreases when increasing the pitch angle, as the forces diminish when perpendicular component of solar wind velocity is lower, being the maximum deformation produced at Sun-facing configuration.

After that, LQR control is applied and several maneuvers are simulated to study the E-sail behaviour (Section 4.2. First of all, assuming control saturation, we have determined the maximum pitch angle that can be reached when applying LQR to our non-symmetrical E-sail model. This operative limit is located at 28 degrees, approximately, which is bigger to that reached on the reference [2], at 15 degrees. Besides, inside this practical maneuvering range, the E-sail response in terms of attitude, angular velocity and control voltage has been observed to be stable and accurate, near to the stablished reference trajectory.

Obviating saturation, LQR control has been tested at high final pitch angles, to set the theoretical validity limits in case that propulsive technology is developed in the future and would allow a higher control voltage that the one considered. Therefore, a maximum feasible pitch angle of 65 degrees is theoretically obtained, being the demand on control power increased when increasing the desired final pitch. Besides, at intermediate pitch angles, around 40 and 50 degrees, a slight but stable oscillation appears on the attitude response, losing a bit of accuracy, but staying close to the desired reference.

Finally, the E-sail state is considered to be estimated from gyroscopes measurements with a certain white gaussian noise, as well as a noise that disturbs the system dynamics. In this context, LQG control is applied (Section 4.3, which is capable of filtering the noise in mean and providing an accurate attitude response at the maneuvering ranges studied for LQR. However, a low frequency oscillation not filtered from the noise is propagated to the state estimates and, then, to the pitch response, altough its amplitude can be considered negligible at low pitch angles, being more relevant at higher pitch angles. Additionally, by worsening the standard deviation quality of the sensors, we have observed how the accurate of the controller is affected.

To conclude, several related future works that could be performed are commented. On the one hand, appart from the maneuvering feasibility that has been analyzed in this project according to the control capabilities, the operative range should be studied in terms of mechanical and structural capabilities, and test the actual behaviour with a prototype in reality. On the other hand, a deeper analysis of perturbations and instrumental errors can be performed, using detailed models of the disturbances sources (e.g. gravitational gradients or neglected centrifugal terms) and more complete models of the gyroscopes, including noise combined with bias.

A Shape coefficient derivatives

This first appendix is dedicated to the computation of the first derivatives of shape coefficient with respect to the state and control variables needed for subsequent calculations used for linearization of dynamic differential equations in Section 3.2.

A.1 Derivatives of shape coefficient with respect to control variables

Firstly, derivating the shape coefficient definition in Equation (2.14) with respect to control variables σ_k, with k from 1 to N, the following result is reached:

$$\frac{\partial b_{l_k}}{\partial \sigma_k} = \frac{F_{x_k}\frac{\partial F_{z_k}}{\partial \sigma_k} - F_{z_k}\frac{\partial F_{x_k}}{\partial \sigma_k}}{F_{x_k}^2}, \tag{A.1}$$

where the derivatives of the local forces acting on tether k root with control variable σ_k can be expressed, using chain rule for derivation and clearing the derivative that wants to be computed, as:

$$\frac{\partial F_{x_k}}{\partial \sigma_k} = a_1 \frac{\partial b_{l_k}}{\partial \sigma_k} + a_2, \tag{A.2}$$

$$\frac{\partial F_{z_k}}{\partial \sigma_k} = a_3 \frac{\partial b_{l_k}}{\partial \sigma_k} + a_4, \tag{A.3}$$

with coefficients a_1 to a_4 developed in Equations (A.4)-(A.7):

$$\begin{aligned} a_1 = \rho\omega^2 L^2 \frac{\partial g_1}{\partial b_{l_k}} + \sigma_k u L \Bigg\{ & \sin\alpha_n \cos\delta_n \cos\zeta_k \frac{\partial g_2}{\partial b_{l_k}} + \sin\alpha_n \sin\delta_n \sin\zeta_k \frac{\partial g_2}{\partial b_{l_k}} \\ & - \cos(\delta_n - \zeta_k) \sin\alpha_n \frac{\partial g_3}{\partial b_{l_k}} - \cos\alpha_n \frac{\partial g_4}{\partial b_{l_k}} \Bigg\}, \end{aligned} \tag{A.4}$$

$$a_2 = uL\left\{\sin\alpha_n \cos\delta_n \cos\zeta_k g_2 + \sin\alpha_n \sin\delta_n \sin\zeta_k g_2 - \cos(\delta_n - \zeta_k)\sin\alpha_n g_3 - \cos\alpha_n g_4\right\}, \tag{A.5}$$

$$a_3 = \sigma_k u L \left\{ \cos\alpha_n \frac{\partial g_2}{\partial b_{l_k}} - \cos(\delta_n - \zeta_k)\sin\alpha_n \frac{\partial g_4}{\partial b_{l_k}} - \frac{\partial g_5}{\partial b_{l_k}} \right\}, \tag{A.6}$$

$$a_4 = uL\left\{\cos\alpha_n g_2(b_{l_k}) - \cos(\delta_n - \zeta_k)\sin\alpha_n g_4(b_{l_k}) - g_5(b_{l_k})\right\}. \tag{A.7}$$

As a result, we can introduce the linear expressions (A.2)-(A.3) in Equation (A.1), obtaining a simple analytical expression to compute the derivative of the shape coefficient with respect to the control variable of tether k:

$$\frac{\partial b_{l_k}}{\partial \sigma_k} = \frac{a_4 F_{x_k} - a_2 F_{z_k}}{F_{x_k}^2 - a_3 F_{x_k} + a_1 F_{z_k}}. \tag{A.8}$$

Finally, the derivatives of auxiliar functions with respect to shape coefficient are shown:

$$\begin{aligned}\frac{\partial g_1}{\partial b_{l_k}} = \Bigg(& \frac{b_{l_k}(1+x)}{2\sqrt{(1+x)^2+b_{l_k}^2}} + b_{l_k} \ln\left|\frac{1+x+\sqrt{(1+x)^2+b_{l_k}^2}}{b_{l_k}}\right| \\ & - \frac{b_{l_k}(1+x)}{2(1+x+\sqrt{(1+x)^2+b_{l_k}^2})}\left(1+\frac{1+x}{\sqrt{(1+x)^2+b_{l_k}^2}}\right) \\ & + \frac{1}{2}\ln\left|\frac{\sqrt{(1+x)^2+b_{l_k}^2}}{b_{l_k}}+1\right| - \frac{1}{2}\left|\frac{\sqrt{(1+x)^2+b_{l_k}^2}}{b_{l_k}}-1\right| - \frac{b_{l_k}}{\sqrt{(1+x)^2+b_{l_k}^2}}\Bigg]_{x=0}^{x=1},\end{aligned} \tag{A.9}$$

$$\frac{\partial g_2}{\partial b_{l_k}} = \left(-\frac{1}{2}\ln\left|\frac{\sqrt{(1+x)^2+b_{l_k}^2}}{b_{l_k}}+1\right| + \frac{1}{2}\left|\frac{\sqrt{(1+x)^2+b_{l_k}^2}}{b_{l_k}}+1\right| - \frac{b_{l_k}}{\sqrt{(1+x)^2+b_{l_k}^2}}\right]_{x=0}^{x=1}, \tag{A.10}$$

$$\frac{\partial g_3}{\partial b_{l_k}} = \left(\frac{b_{l_k}}{\sqrt{(1+x)^2+b_{l_k}^2}}\right]_{x=0}^{x=1}, \tag{A.11}$$

$$\frac{\partial g_4}{\partial b_{l_k}} = \left(\ln\left|\frac{1+x+\sqrt{(1+x)^2+b_{l_k}^2}}{b_{l_k}}\right| - \frac{1+x}{1+x+\sqrt{(1+x)^2+b_{l_k}^2}}\left(1+\frac{1+x}{\sqrt{(1+x)^2+b_{l_k}^2}}\right)\right]_{x=0}^{x=1}, \tag{A.12}$$

$$\frac{\partial g_5}{\partial b_{l_k}} = \left(-\frac{b_{l_k}(1+x)\sec^2\left(\frac{1}{2}\arctan\left(\frac{1+x}{b_{l_k}}\right)\right)}{2(b_{l_k}^2+(1+x)^2)\tan\left(\frac{1}{2}\arctan\left(\frac{1+x}{b_{l_k}}\right)\right)}\right]_{x=0}^{x=1}. \tag{A.13}$$

A.2 Derivatives of shape coefficient with respect to Euler angles

The strategy in this case is similar to that stated in A.1, but we now need to describe the derivatives of sine and cosine of angles α_n and δ_n with respect to Euler angles ϕ and θ, as those are the angles appearing in torque calculations.

Then, working with Equation (2.47) we have that $\cos\alpha_n = \cos\phi\cos\theta$ and $\sin\delta_n = \sin\phi/\sin\alpha_n$.

Besides, it is known that $\sin\alpha_n = \sqrt{1-\cos^2\alpha_n}$ and $\cos\delta_n = \sqrt{1-\sin^2\delta_n}$. Therefore, derivating these expressions and properly applying the chain rule, the derivatives of sine and cosine of the orientation angles are obtained:

$$\frac{\partial\cos\alpha_n}{\partial\phi} = -\sin\phi\cos\theta, \tag{A.14}$$

$$\frac{\partial\cos\alpha_n}{\partial\theta} = -\cos\phi\sin\theta, \tag{A.15}$$

$$\frac{\partial\sin\alpha_n}{\partial\phi} = \frac{-\cos\alpha_n}{\sqrt{1-\cos^2\alpha_n}}\frac{\partial\cos\alpha_n}{\partial\phi}, \tag{A.16}$$

$$\frac{\partial\sin\alpha_n}{\partial\theta} = \frac{-\cos\alpha_n}{\sqrt{1-\cos^2\alpha_n}}\frac{\partial\cos\alpha_n}{\partial\theta}, \tag{A.17}$$

$$\frac{\partial\sin\delta_n}{\partial\phi} = \frac{\sin\alpha_n\cos\phi - \sin\phi\dfrac{\partial\sin\alpha_n}{\partial\phi}}{\sin^2\alpha_n}, \tag{A.18}$$

$$\frac{\partial\sin\delta_n}{\partial\theta} = -\frac{\sin\phi\dfrac{\partial\sin\alpha_n}{\partial\theta}}{\sin^2\alpha_n}, \tag{A.19}$$

$$\frac{\partial\cos\delta_n}{\partial\phi} = \frac{-\sin\delta_n}{\sqrt{1-\sin^2\delta_n}}\frac{\partial\sin\delta_n}{\partial\phi}, \tag{A.20}$$

$$\frac{\partial\cos\delta_n}{\partial\theta} = \frac{-\sin\delta_n}{\sqrt{1-\sin^2\delta_n}}\frac{\partial\sin\delta_n}{\partial\theta}. \tag{A.21}$$

Additionally, in Equations (2.34)-(2.36) also appears the cosine and sine of the substraction $\delta_n - \zeta_k$. Therefore, we have to get the corresponding derivatives of δ_n from derivation of the relationship $\delta_n = \arcsin(\sin\delta_n)$ with chain rule and, then, it is possible to use these values to compute the derivatives of $\cos(\delta_n - \zeta_k)$ and $\sin(\delta_n - \zeta_k)$:

$$\frac{\partial\cos(\delta_n - \zeta_k)}{\partial\phi} = -\sin(\delta_n - \zeta_k)\frac{\partial\delta_n}{\partial\phi}, \tag{A.22}$$

$$\frac{\partial\cos(\delta_n - \zeta_k)}{\partial\theta} = -\sin(\delta_n - \zeta_k)\frac{\partial\delta_n}{\partial\theta}, \tag{A.23}$$

$$\frac{\partial\sin(\delta_n - \zeta_k)}{\partial\phi} = \cos(\delta_n - \zeta_k)\frac{\partial\delta_n}{\partial\phi}, \tag{A.24}$$

$$\frac{\partial\sin(\delta_n - \zeta_k)}{\partial\theta} = \cos(\delta_n - \zeta_k)\frac{\partial\delta_n}{\partial\theta}, \tag{A.25}$$

$$\frac{\partial \delta_n}{\partial \phi} = \frac{1}{\sqrt{1-\sin^2\delta_n}}\frac{\partial \sin\delta_n}{\partial \phi}, \tag{A.26}$$

$$\frac{\partial \delta_n}{\partial \theta} = \frac{1}{\sqrt{1-\sin^2\delta_n}}\frac{\partial \sin\delta_n}{\partial \theta}. \tag{A.27}$$

Once all these preliminary calculations are performed, then we apply the same procedure as in A.1 to compute the first derivative of the shape coefficient with respect to the Euler angles. Below only expressions for ϕ derivatives are shown; actually, for θ it is only needed to substitute them by θ derivatives. So, derivating Equation (2.14):

$$\frac{\partial b_{l_k}}{\partial \phi} = \frac{F_{x_k}\frac{\partial F_{z_k}}{\partial \phi} - F_{z_k}\frac{\partial F_{x_k}}{\partial \phi}}{F_{x_k}^2}, \tag{A.28}$$

where the derivatives of the local forces acting on tether k root with Euler angle ϕ can be expressed, using chain rule for derivation and clearing the derivative that wants to be computed, as:

$$\frac{\partial F_{x_k}}{\partial \phi} = a_5\frac{\partial b_{l_k}}{\partial \phi} + a_6, \tag{A.29}$$

$$\frac{\partial F_{z_k}}{\partial \sigma_k} = a_7\frac{\partial b_{l_k}}{\partial \phi} + a_8, \tag{A.30}$$

with coefficients a_5 to a_8 developed in Equations (A.31)-(A.34):

$$a_5 = \rho\omega^2L^2\frac{\partial g_1}{\partial b_{l_k}} + \sigma_k uL\left[(\sin\alpha_n\cos\delta_n\cos\zeta_k + \sin\alpha_n\sin\delta_n\sin\zeta_k)\frac{\partial g_2}{\partial b_{l_k}}\right.$$
$$\left. - \cos(\delta_n-\zeta_k)\sin\alpha_n\frac{\partial g_3}{\partial b_{l_k}} - \cos\alpha_n\frac{\partial g_4}{\partial b_{l_k}}\right], \tag{A.31}$$

$$a_6 = \sigma_k uL\left\{g_2\left(\frac{\partial \sin\alpha_n}{\partial \phi}\cos\delta_n\cos\zeta_k + \sin\alpha_n\frac{\partial \cos\delta_n}{\partial \phi}\cos\zeta_k + \frac{\partial \sin\alpha_n}{\partial \phi}\sin\delta_n\sin\zeta_k\right.\right.$$
$$\left.\left. + \sin\alpha_n\frac{\partial \sin\alpha_n}{\partial \phi}\sin\zeta_k\right) - \left(\frac{\partial \cos(\delta_n-\zeta_k)}{\partial \phi}\sin\alpha_n + \cos(\delta_n-\zeta_k)\frac{\partial \sin\alpha_n}{\partial \phi}\right)g_3 - \frac{\partial \sin\alpha_n}{\partial \phi}g_4\right\}, \tag{A.32}$$

$$a_7 = \sigma_k uL\left\{\cos\alpha_n\frac{\partial g_2}{\partial b_{lk}} - \cos(\delta_n-\zeta_k)\sin\alpha_n\frac{\partial g_4}{\partial b_{lk}} - \cos\alpha_n\frac{\partial g_5}{\partial b_{lk}}\right\}, \tag{A.33}$$

$$a_8 = \sigma_k uL\left\{\frac{\partial \cos\alpha_n}{\partial \phi}g_2 - \left(\frac{\partial \cos(\delta_n-\zeta_k)}{\partial \phi}\sin\alpha_n + \cos(\delta_n-\zeta_k)\frac{\partial \sin\alpha_n}{\partial \phi}\right)g_4 - \frac{\partial \cos\alpha_n}{\partial \phi}g_5\right\}. \tag{A.34}$$

Again, we can introduce the linear expressions (A.29)-(A.30) in Equation (A.28), obtaining a simple analytical expression to compute the derivative of the shape coefficient with respect to the Euler angles:

$$\frac{\partial b_{l_k}}{\partial \phi} = \frac{a_8 F_{x_k} - a_6 F_{z_k}}{F_{x_k}^2 - a_7 F_{x_k} + a_5 F_{z_k}}. \tag{A.35}$$

B Torque components derivatives

Once the derivatives of shape coefficient have been exposed in Appendix A, this appendix is dedicated to develop the expressions of the partial derivatives of torque components with respect to both control variables and Euler angles. They are expressed in terms of the torque contribution of a each tether k; being the total torque the sum from $k = 1$ to N.

B.1 Derivatives of torque components with respect to control variables

The torque components derived with respect to control variables σ_k are:

$$\frac{\partial \mathscr{E}_k}{\partial \sigma_k} = \frac{\mathscr{E}_k}{\sigma_k} + uL^2 \sigma_k \sin\alpha_n \left[\cos(\delta_n - \zeta_k)\sin\zeta_k(\ln 8 - 2) - \sin\delta_n(\ln 4 - 1)\right] \frac{\partial b_{l_k}}{\partial \sigma_k}, \tag{B.1}$$

$$\frac{\partial \mathscr{F}_k}{\partial \sigma_k} = \frac{\mathscr{F}_k}{\sigma_k} + uL^2 \sigma_k \sin\alpha_n \left[\cos\delta_n(\ln 4 - 1) - \cos(\delta_n - \zeta_k)\cos\zeta_k(\ln 8 - 2)\right] \frac{\partial b_{l_k}}{\partial \sigma_k}, \tag{B.2}$$

$$\frac{\partial \mathscr{G}_k}{\partial \sigma_k} = \frac{\mathscr{G}_k}{\sigma_k}, \tag{B.3}$$

where $\partial b_{l_k} / \partial \sigma_k$ are computed according to Appendix A.1.

B.2 Derivatives of torque components with respect to Euler angles

The torque components derived with respect to Euler angle ϕ are:

$$\begin{aligned} \frac{\partial \mathscr{E}_k}{\partial \phi} = uL^2 \sigma_k \Bigg\{ & \frac{\partial b_{l_k}}{\partial \phi} \sin\alpha_n \left[\cos(\delta_n - \zeta_n)\sin\zeta_k(\ln 8 - 2) - \sin\delta_n(\ln 4 - 1)\right] \\ & + b_{l_k} \frac{\partial \sin\alpha_n}{\partial \phi} \left[\cos(\delta_n - \zeta_n)\sin\zeta_k(\ln 8 - 2) - \sin\delta_n(\ln 4 - 1)\right] \\ & + b_{l_k} \sin\alpha_n \left[\frac{\partial \cos(\delta_n - \zeta_n)}{\partial \phi} \sin\zeta_k(\ln 8 - 2) - \frac{\partial \sin\delta_n}{\partial \phi}(\ln 4 - 1)\right] + \frac{\sin\delta_k}{2} \frac{\partial \cos\alpha_n}{\partial \phi} \Bigg\}, \end{aligned} \tag{B.4}$$

$$
\begin{aligned}
\frac{\partial \mathscr{F}_k}{\partial \phi} &= uL^2\sigma_k \left\{ \frac{\partial b_{l_k}}{\partial \phi} \sin\alpha_n \left[\cos\delta_n(\ln 4 - 1) - \cos(\delta_n - \zeta_n)\cos\zeta_k(\ln 8 - 2)\right] \right. \\
&+ b_{l_k} \frac{\partial \sin\alpha_n}{\partial \phi} \left[\cos\delta_n(\ln 4 - 1) - \cos(\delta_n - \zeta_n)\cos\zeta_k(\ln 8 - 2)\right] \\
&\left. + b_{l_k} \sin\alpha_n \left[\frac{\partial \cos(\delta_n)}{\partial \phi}(\ln 4 - 1)\sin - \frac{\partial \cos(\delta_n - \zeta_n)}{\partial \phi} \cos\zeta_k(\ln 8 - 2) \right] + \frac{\partial \cos\alpha_n}{\partial \phi} \frac{\cos\zeta_k}{2} \right\},
\end{aligned}
\tag{B.5}
$$

$$
\frac{\partial \mathscr{G}_k}{\partial \phi} = \frac{uL^2\sigma_k}{2} \left\{ \frac{\partial \sin(\delta_n - \zeta_n)}{\partial \phi} \sin\alpha_n + \sin(\delta_n - \zeta_n) \frac{\partial \sin\alpha_n}{\partial \phi} \right\}. \tag{B.6}
$$

where $\partial b_{l_k}/\partial \phi$ are computed according to Appendix A.2.

To compute the torque components derived with respect to Euler angle θ, the expressions are similar, just substituting ϕ derivations by θ derivations.

C Linearization matrices

This appendix is dedicated to show the components of matrices A and B appearing in linearized movement equations used for LQR method. In the case of regulation phase, these matrices do not depend on time, and each column is the result of derivation of equations 2.55 with respect to the state and control variables, as appropriate. As computations for tracking phase share the same expressions, but being them particularized for each time instant, this appendix will show only the results obviating time.

C.1 Matrix A

On the one hand, matrix A is composed of the first derivatives of equations $\mathbf{f}$ with respect to non-dimensional state variables, hence obtaining the components represented in Equations (C.1)-(C.36).

In Equations (C.4)-(C.6) and (C.10)-(C.12), the first derivatives of torque components with respect to Euler angles ϕ and θ are computed according to Appendix B.2. It is also important to remark that Euler angle ψ does not appear in Equation (2.55) and torque components are not dependent of it, so the derivatives with respect to ψ are all null.

- Matrix A components resulting from ϕ derivation:

$$A_{11} = \frac{\partial f_1(\mathbf{X}_{ref},\mathbf{\Gamma}_{ref})}{\partial \phi} = 0, \tag{C.1}$$

$$A_{21} = \frac{\partial f_2(\mathbf{X}_{ref},\mathbf{\Gamma}_{ref})}{\partial \phi} = \frac{\omega_{z_{ref}} \cos\theta_{ref} - \omega_{x_{ref}} \sin\theta_{ref}}{\cos^2\phi_{ref}}, \tag{C.2}$$

$$A_{31} = \frac{\partial f_3(\mathbf{X}_{ref},\mathbf{\Gamma}_{ref})}{\partial \phi} = (\omega_{z_{ref}} \cos\theta_{ref} - \omega_{x_{ref}} \sin\theta_{ref}) \tan\phi_{ref} \sec\phi_{ref}, \tag{C.3}$$

$$A_{41} = \frac{\partial f_4(\mathbf{X}_{ref},\mathbf{\Gamma}_{ref})}{\partial \phi} = \frac{1}{I_t\omega^2} \frac{\partial \mathscr{E}(\mathbf{X}_{ref},\mathbf{\Gamma}_{ref})}{\partial \phi}, \tag{C.4}$$

$$A_{51} = \frac{\partial f_5(\mathbf{X}_{ref},\mathbf{\Gamma}_{ref})}{\partial \phi} = \frac{1}{I_t\omega^2} \frac{\partial \mathscr{F}(\mathbf{X}_{ref},\mathbf{\Gamma}_{ref})}{\partial \phi}, \tag{C.5}$$

$$A_{61} = \frac{\partial f_6(\mathbf{X}_{ref},\mathbf{\Gamma}_{ref})}{\partial \phi} = \frac{1}{I_z\omega^2} \frac{\partial \mathscr{G}(\mathbf{X}_{ref},\mathbf{\Gamma}_{ref})}{\partial \phi}. \tag{C.6}$$

- Matrix A components resulting from θ derivation:

$$A_{12} = \frac{\partial f_1(\mathbf{X}_{ref},\mathbf{\Gamma}_{ref})}{\partial \theta} = -\omega_{x_{ref}} \sin\theta_{ref} + \omega_{z_{ref}} \cos\theta_{ref}, \tag{C.7}$$

$$A_{22} = \frac{\partial f_2(\mathbf{X}_{ref},\mathbf{\Gamma}_{ref})}{\partial \theta} = (\omega_{z_{ref}} \sin\theta_{ref} + \omega_{x_{ref}} \cos\theta_{ref}) \tan\phi_{ref}, \tag{C.8}$$

$$A_{32} = \frac{\partial f_3(\mathbf{X}_{ref},\mathbf{\Gamma}_{ref})}{\partial \theta} = (-\omega_{z_{ref}} \sin\theta_{ref} - \omega_{x_{ref}} \cos\theta_{ref}) \sec\phi_{ref}, \tag{C.9}$$

$$A_{42} = \frac{\partial f_4(\mathbf{X}_{ref},\mathbf{\Gamma}_{ref})}{\partial \theta} = \frac{1}{I_t\omega^2}\frac{\partial \mathscr{E}(\mathbf{X}_{ref},\mathbf{\Gamma}_{ref})}{\partial \theta}, \tag{C.10}$$

$$A_{52} = \frac{\partial f_5(\mathbf{X}_{ref},\mathbf{\Gamma}_{ref})}{\partial \theta} = \frac{1}{I_t\omega^2}\frac{\partial \mathscr{F}(\mathbf{X}_{ref},\mathbf{\Gamma}_{ref})}{\partial \theta}, \tag{C.11}$$

$$A_{62} = \frac{\partial f_6(\mathbf{X}_{ref},\mathbf{\Gamma}_{ref})}{\partial \theta} = \frac{1}{I_z\omega^2}\frac{\partial \mathscr{G}(\mathbf{X}_{ref},\mathbf{\Gamma}_{ref})}{\partial \theta}. \tag{C.12}$$

- Matrix A components resulting from ψ derivation:

$$A_{13} = \frac{\partial f_1(\mathbf{X}_{ref},\mathbf{\Gamma}_{ref})}{\partial \psi} = 0, \tag{C.13}$$

$$A_{23} = \frac{\partial f_2(\mathbf{X}_{ref},\mathbf{\Gamma}_{ref})}{\partial \psi} = 0, \tag{C.14}$$

$$A_{33} = \frac{\partial f_3(\mathbf{X}_{ref},\mathbf{\Gamma}_{ref})}{\partial \psi} = 0, \tag{C.15}$$

$$A_{43} = \frac{\partial f_4(\mathbf{X}_{ref},\mathbf{\Gamma}_{ref})}{\partial \psi} = 0, \tag{C.16}$$

$$A_{53} = \frac{\partial f_5(\mathbf{X}_{ref},\mathbf{\Gamma}_{ref})}{\partial \psi} = 0, \tag{C.17}$$

$$A_{63} = \frac{\partial f_6(\mathbf{X}_{ref},\mathbf{\Gamma}_{ref})}{\partial \psi} = 0. \tag{C.18}$$

- Matrix A components resulting from ω_x derivation:

$$A_{14} = \frac{\partial f_1(\mathbf{X}_{ref},\mathbf{\Gamma}_{ref})}{\partial \omega_x} = \cos\theta_{ref}, \tag{C.19}$$

$$A_{24} = \frac{\partial f_2(\mathbf{X}_{ref},\mathbf{\Gamma}_{ref})}{\partial \omega_x} = \sin\theta_{ref} \tan\phi_{ref}, \tag{C.20}$$

$$A_{34} = \frac{\partial f_3(\mathbf{X}_{ref},\mathbf{\Gamma}_{ref})}{\partial \omega_x} = -\sin\theta_{ref} \sec\phi_{ref}, \tag{C.21}$$

$$A_{44} = \frac{\partial f_4(\mathbf{X}_{ref},\mathbf{\Gamma}_{ref})}{\partial \omega_x} = 0, \tag{C.22}$$

$$A_{54} = \frac{\partial f_5(\mathbf{X}_{ref},\mathbf{\Gamma}_{ref})}{\partial \omega_x} = \frac{I_z - I_t}{I_t}\omega_{z_{ref}}, \tag{C.23}$$

$$A_{64} = \frac{\partial f_6(\mathbf{X}_{ref},\mathbf{\Gamma}_{ref})}{\partial \omega_x} = 0. \tag{C.24}$$

- Matrix A components resulting from ω_y derivation:

$$A_{15} = \frac{\partial f_1(\mathbf{X}_{ref},\mathbf{\Gamma}_{ref})}{\partial \omega_y} = 0, \tag{C.25}$$

$$A_{25} = \frac{\partial f_2(\mathbf{X}_{ref},\mathbf{\Gamma}_{ref})}{\partial \omega_y} = 1, \tag{C.26}$$

$$A_{35} = \frac{\partial f_3(\mathbf{X}_{ref},\mathbf{\Gamma}_{ref})}{\partial \omega_y} = 0, \tag{C.27}$$

$$A_{45} = \frac{\partial f_4(\mathbf{X}_{ref},\mathbf{\Gamma}_{ref})}{\partial \omega_y} = \frac{I_t - I_z}{I_t}\omega_{z_{ref}}, \tag{C.28}$$

$$A_{55} = \frac{\partial f_5(\mathbf{X}_{ref},\mathbf{\Gamma}_{ref})}{\partial \omega_y} = 0, \tag{C.29}$$

$$A_{65} = \frac{\partial f_6(\mathbf{X}_{ref},\mathbf{\Gamma}_{ref})}{\partial \omega_y} = 0. \tag{C.30}$$

- Matrix A components resulting from ω_z derivation:

$$A_{16} = \frac{\partial f_1(\mathbf{X}_{ref},\mathbf{\Gamma}_{ref})}{\partial \omega_z} = \sin\theta_{ref}, \tag{C.31}$$

$$A_{26} = \frac{\partial f_2(\mathbf{X}_{ref},\mathbf{\Gamma}_{ref})}{\partial \omega_z} = -\cos\theta_{ref}\tan\phi_{ref}, \tag{C.32}$$

$$A_{36} = \frac{\partial f_3(\mathbf{X}_{ref},\mathbf{\Gamma}_{ref})}{\partial \omega_z} = \cos\theta_{ref}\sec\phi_{ref}, \tag{C.33}$$

$$A_{46} = \frac{\partial f_4(\mathbf{X}_{ref},\mathbf{\Gamma}_{ref})}{\partial \omega_z} = \frac{I_t - I_z}{I_t}\omega_{y_{ref}}, \tag{C.34}$$

$$A_{56} = \frac{\partial f_5(\mathbf{X}_{ref},\mathbf{\Gamma}_{ref})}{\partial \omega_z} = \frac{I_z - I_t}{I_t}\omega_{x_{ref}}, \tag{C.35}$$

$$A_{66} = \frac{\partial f_6(\mathbf{X}_{ref},\mathbf{\Gamma}_{ref})}{\partial \omega_z} = 0. \tag{C.36}$$

C.2 Matrix B

On the other hand, matrix B results from derivation of equations $\mathbf{f}$ with respect to each non-dimensional control variable Γ_k (with k from 1 to N), where the derivative of torque components with respect to Γ_k are computed according to Appendix B.1:

$$B_{1k} = \frac{\partial f_1(\mathbf{X}_{ref}, \mathbf{\Gamma}_{ref})}{\partial \Gamma_k} = 0, \tag{C.37}$$

$$B_{2k} = \frac{\partial f_2(\mathbf{X}_{ref}, \mathbf{\Gamma}_{ref})}{\partial \Gamma_k} = 0, \tag{C.38}$$

$$B_{3k} = \frac{\partial f_3(\mathbf{X}_{ref}, \mathbf{\Gamma}_{ref})}{\partial \Gamma_k} = 0, \tag{C.39}$$

$$B_{4k} = \frac{\partial f_4(\mathbf{X}_{ref}, \mathbf{\Gamma}_{ref})}{\partial \Gamma_k} = \frac{\sigma}{I_t \omega^2} \frac{\partial \mathscr{E}_k(\mathbf{X}_{ref}, \mathbf{\Gamma}_{ref})}{\partial \Gamma_k}, \tag{C.40}$$

$$B_{5k} = \frac{\partial f_5(\mathbf{X}_{ref}, \mathbf{\Gamma}_{ref})}{\partial \Gamma_k} = \frac{\sigma}{I_t \omega^2} \frac{\partial \mathscr{F}_k(\mathbf{X}_{ref}, \mathbf{\Gamma}_{ref})}{\partial \Gamma_k}, \tag{C.41}$$

$$B_{6k} = \frac{\partial f_6(\mathbf{X}_{ref}, \mathbf{\Gamma}_{ref})}{\partial \Gamma_k} = \frac{\sigma}{I_z \omega^2} \frac{\partial \mathscr{G}_k(\mathbf{X}_{ref}, \mathbf{\Gamma}_{ref})}{\partial \Gamma_k}. \tag{C.42}$$

List of Figures

Bibliography

[1] M. Bassetto, L. Niccolai, A.A. Quarta, and G. Mengali, *A comprehensive review of electric solar wind sail concept and its applications*, Progress in Aerospace Sciences **128** (2022).

[2] J. Pérez, G. Pacheco, and R. Vázquez, *Control de actitud de las e-sail mediante la modulación del voltaje de los tethers*, Universidad de Sevilla (2022).

[3] B. Fu, E. Sperber, and F. Eke, *Solar sail technology — a state of the art review*, Progress in Aerospace Sciences **86** (2016), no. 1-19.

[4] P. Janhunen, *Electric sail for spacecraft propulsion*, Journal of Propulsion and Power **20** (2004), no. 4.

[5] F.J. Urrios, G. Pacheco, and R. Vázquez, *Optimal planning and guidance strategies in coplanar circular interplanetary missions using electric solar wind sails*, Universidad de Sevilla (2022).

[6] P. Janhunen, A.A. Quarta, and G. Mengali, *Electric solar wind sail mass budget model*, Geoscientific Instrumentation, Methods and Data Systems **2** (2013), no. 1, 85–95.

[7] P. Janhunen, P. Toivanen, J. Envall, S. Merikallio, G. Montesanti, J. González, M. Noorma U. Kvell, and S. Lätt, *Electric solar wind sail applications overview*, (2014).

[8] P. Janhunen, *Photonic spin control for solar wind electric sail*, Acta Astronautica **83** (2013), 85–90.

[9] P.K. Toivanen and P. Janhunen, *Spin plane control and thrust vectoring of electric solar wind sail*, Journal of Propulsion and Power **29** (2013), 178–185.

[10] P.K. Toivanen and P. Janhunen, *Thrust vectoring of an electric solar wind sail with a realistic sail shape*, Acta Astronautica **131** (2013), 145–151.

[11] M. Bassetto, G. Mengali, and A.A. Quarta, *Thrust and torque vector characteristics of axially-symmetric e-sail*, Acta Astronautica **146** (2018), 134–143.

[12] M. Bassetto, G. Mengali, and A.A. Quarta, *E-sail attitude control with tether voltage modulation*, Acta Astronautica **166** (2020), 350–357.

[13] G. Li, Z.H. Zhu, and C. Du, *Flight dynamics and control strategy of electric solar wind sails*, Journal of Guidance, Control and Dynamics **43** (2020), 462–474.

[14] C. Du, Z.H. Zhu, and G. Li, *Analysis of thrust-induced sail plane coning and attitude motion of electric sail*, Acta Astronautica **178** (2021), 129–142.

[15] C. Du, Z.H. Zhu, and G. Li, *Rigid-flexible coupling effect on attitude dynamics of electric solar wind sail*, Communications in Nonlinear Science and Numerical Simulation **95** (2021), 105663.

[16] L. Huang, H. Wen, L. Cheng, and S. Xu, *Nonlinear model predictive control for attitude maneuver of a barbell electric sail through voltage regulation*, Acta Astronautica **179** (2021), 146–152.

[17] P. Toivanen and P. Janhunen, *Thrust vectoring of an electric solar wind sail with a realistic sail shape*, Acta Astronautica **131** (2017), 145–151.

[18] R. Vázquez, *Spacecraft dynamics (lecture notes)*, extracted from http://aero.us.es/dve/desc.html (2023).

[19] M. Athans, *The role and use of the stochastic linear-quadratic-gaussian problem in control system design*, IEEE Transactions on Automatic Control **16** (1971), 529–552.